2006

Inscription and characterization of fiber Bragg gratings in multi-mode As2S3 optical fiber at 1550nm using interferometric and phase mask methods

Hang Yan Yuen
Iowa State University

Inscription and characterization of fiber Bragg gratings in multi-mode As_2S_3 optical fiber at 1550nm using interferometric and phase mask methods

by

Hang Yan Yuen

A dissertation submitted to the graduate faculty

in partial fulfillment of the requirements for the degree of

DOCTOR OF PHILOSOPHY

Major: Materials Science and Engineering

Program of Study Committee:
Steve W. Martin, Major Professor
Kristen Constant
Xiaoli Tan
Palaniappa A. Moilan
Joseph Shinar

Iowa State University

Ames, Iowa

2006

UMI Number: 3243844

UMI Microform 3243844

ProQuest Information and Learning Company
300 North Zeeb Road
P.O. Box 1346
Ann Arbor, MI 48106-1346

Dedicated to my family and Hui
for their love and support during my education.

Table of contents

List of figures

List of tables

Abstract

Fiber Bragg gratings (FBGs) in optical fibers are quickly growing in appeal and are being considered by researchers for use as mechanical and chemical sensors in fiber reinforced composite airframes to provide inexpensive, high sensitivity and high density sensor coverage. Such FBG detection systems offer the advantages of being rapid, sensitive, radiation-hard and low density. To date, typical silica-glass optical fibers have been studied. However, the ultimate sensitivity of FBGs in silica fiber is limited by the relatively low photosensitivity of silica glass which leads to low reflectivities of the FBGs. In this project, advantage is taken of the significantly higher photosensitivity of chalcogenide glasses, glasses based upon the chalcogenide elements, S, Se, and Te to inscript FBGs in selected chalcogenide optical fibers, specifically As_2S_3. Time stability, power level dependence, and temperature dependence were measured for the FBGs written in multi-mode As_2S_3 optical fiber.

FBGs were inscripted in multi-mode arsenic sulfide (As_2S_3) glass fibers at 1550 nm by He-Ne laser irradiation using the interferometric and phase mask techniques. In the set up, a broadband light source centered at 1550 nm with a bandwidth of 100nm at half intensity (Agilent Broadband light source 83437A) and an OSA (Agilent HP86412B) were used to analyze the inscribed FBGs and the reflectivity around 1550 nm.

Multiple transmission dips were obtained from the FBGs writing experiment using both the interferometric and phase mask techniques that were caused by same mode reflection and neighboring mode coupling. Using the interferrometric method, we obtained FBGs with maximum reflectivity 46.6% at 1526.6 nm. The average effective index change in the glass caused by the He-Ne laser irradiation inducing the FBGs is estimated to be +0.000482. Using a 0/-1 order phase mask, we obtained FBGs of maximum reflectivity 61.9% at 1548.8 nm and the average effective index change is estimated to be +0.000491.

1. General introduction

1.1. Fiber Bragg gratings

Optical fibers have revolutionized the modern telecommunication industry. Their low transmission losses have enabled more efficient long-distance communication.

Since the discovery of photosensitivity in germanium doped silica optical fibers, fiber Bragg gratings (FBGs), which are in-fiber components, have been developed. FBGs are refractive index perturbations inscribed in the core of optical fibers resulting from the exposure to intense irradiation. Recently, FBGs have been applied in many ways, such as amplifiers[1], lasers[2], filters[3] and sensors[4]. Regarding their sensing applications, FBGs inscribed in an optical fiber, can be used as a sensor to measure physical parameters (e.g. pressure[5], temperature[6]), chemical parameters[7] (e.g. impurity contamination, leakage), and non specific-parameters (e.g. acoustical vibrations[8]). In this project, the fabrication and characterization of FBGs in optical fibers will be the focus of the study.

1.2. FBGs as mechanical strain and temperature sensors

The basic operation principle of a FBGs-based sensor system lies in monitoring the shift in wavelength of the returned 'Bragg' signal, as a function of the measurand (e.g. strain, temperature). The illustrated diagram is shown at Figure 1-1.

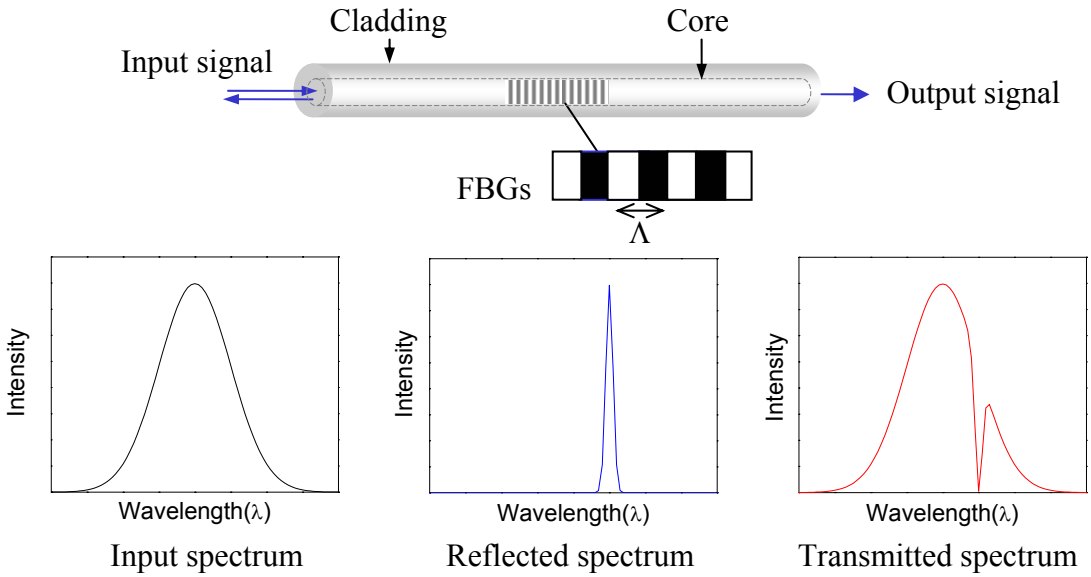

Figure 1-1 Illustration of how a FBGs sensor works[9]

The Bragg wavelength, λ_B, is related to the refractive index of the material, n, and the grating wavelength, Λ, by the simple formula[10]:

$$\lambda_B = 2n\Lambda \qquad 1\text{-}1$$

The strain response occurs because of both the physical elongation of the sensor (and the corresponding change in the grating wavelength), and the change in fiber index due to photo-elastic effects. Strain can thus be determined by measuring the part of wavelength spectrum associated with a particular location. Meanwhile, the temperature sensitivity of the FBGs occurs due to the effect of temperature change on the induced refractive index change and, to a lesser extent, the thermal expansion coefficient of the fiber.

As an added benefit of FBGs sensors, the measurand information is spectrally encoded and therefore the sensor signals are basically unaffected by environmental noise or power loss[11].

1.3. Advantages of FBGs sensors

Several significant advantages of FBGs sensors over other sensing technologies make it well suited as a real time mechanical strain sensor for aircraft structures. Besides being immune to electromagnetic interference, FBGs sensors have high stability, small size, and are lightweight[12]. As a passive sensor, its immunity to electromagnetic interference would eliminate the need for the costly and heavy shielding that is normally used to minimize electrical noise picked up when using electrically active sensors. Moreover, the inherent strength and fatigue and corrosion resistance of fibers enable FBGs sensors to maintain outstanding performance even in the extremely hostile environments of high temperatures under continuous vibrations and shock loadings.

Most importantly, distributed FBGs sensors provide multiple point measurements by using only a single fiber without increasing the size and weight of the sensor system. By multiplexing a number of sensing elements onto a single fiber or fiber pair, a fiber-optic sensor network can be formed and distributed in space. This would save cost by sharing the terminal equipment and also by simplified wiring and reduced installation cost[13].

Also, the measurement of strain inside a reinforced carbon composite used in aircraft would be easier since FBGs sensors can be installed between the laminate without affecting the structural strength, which is difficult to realize with conventional electrical resistance strain gauges. The laminate, in addition, can also even protect the sensor against rough handling[14].

In addition to these applications, the FBGs sensor is a potential candidate to become a multi- measurement detector. Dual measurement of temperature and strain using FBGs technique has been reported[15,16].

Currently, silica glass FBGs sensors are in use and are commercially available for the use of bridge structure[17] and spacecraft health monitoring[18]. In Section 1.5, the reasons for considering other chemistries, chalcogenide in particular, will be discussed.

1.4. Mechanism of photosensitivity in metal doped SiO_2

During non-radiative recombination, amorphous semiconductors exhibit a large variety of photo-induced metastable phenomena and structural changes in these glasses result from

exposure to sub-bandgap irradiation[19]. Among these photoinduced effects, photosensitivity is a more general term to describe the phenomenon of refractive index change of glass upon exposure to photon energy[19].

Although different types of fabrication methods have been reported, the mechanism of photosensitivity in FBGs is not fully understood and cannot be explained by a single model even in germanium-doped silica glass fiber, of which the photosensitivity was first to be discovered[20]. Nevertheless, some of these models[21] are discribed below and can be used as references for studying and examining the mechanism in chalcogenide glass.

1.4.1. Color-center model

This model, first proposed by Hand and Russell[22], suggests that the refractive index change of glass after irradiation is attributed by color-center defects. Due to the chemical reactions during glass forming at elevated temperature, defects are induced within the glass matrix. Further, during fiber drawing, atomic bonds in the glass can break and the glass becomes more inhomogeneous with randomly distributed broken bonds and trapped defects. During irradiation, these defects absorb light and are then transformed into defects that are more polarizable. They become strong optical absorbing color centers and are attributed to the change of the refractive index at longer wavelengths.

The UV-induced refractive index change obeys the Kramer-Kronig equation:

$$\Delta n_{eff}(\lambda) = \frac{1}{2\pi^2} P \int_0^{\infty} \frac{\Delta n_{eff}(\lambda)}{1-(\lambda'-\lambda)} d\lambda \qquad 1\text{-}2$$

where P is the principle part of the integral, λ is the wavelength, and $\Delta n_{eff}(\lambda)$ is the effective change in the absorption coefficient of the defect, which may be modeled as a Gaussian distribution, given by

$$\Delta n_{eff}(\lambda) = \frac{1}{L} \int_0^{L} \Delta\alpha(\lambda, z) dz \qquad 1\text{-}3$$

where L is the sample thickness.

To date, the color center model is the most widely accepted model for the formation mechanism of Bragg gratings in SiO_2 glass. However, it is not clear whether this model alone can always account for all of the observed index changes in glass.

For arsenic trisulfide glass, photosensitivity would be expected to be due to the wrong bond formation such as of As-As, S-S bonds. This has to be carefully examined throughout the research conducted in the future.

1.4.2. Compaction/Densification model

This model, suggested by Fiori and Devine[23], describes a structural alteration in the mechanical nature of the glass. As a result of irradiation, higher-order ring structures collapse and lead to densification. The configurational change in the structure causes the refractive index change. The relationship between the change of refractive index, Δn, can be expressed by

$$\Delta n = \frac{\left(n^2+2\right)\left(n^2-1\right)}{6n}\left[1-\frac{\Delta R}{\left(R\Delta V/V\right)}\right]\frac{\Delta V}{V} \qquad 1\text{-}4$$

where n is the refractive index, V is the volume, R is the refractivity.

If $(V/R)\Delta R/\Delta V<1$, then compaction results in the observed increase in refractive index. There is competition between the terms V/R and ΔR/ΔV, which affect the refractive index. For example, the refractive index increase caused by a volume expansion would be large in the absence of a simultaneous increase in the material polarizability.

1.5. Material selection: chalcogenide glasses

Chalcogenide glasses are materials containing chalcogen elements (group VI: S, Se and Te) and one or more of group V and IV elements such as Ga, Ge, As, etc.[24] One should note that, though oxygen is also a chalcogenide, oxide materials are usually treated separately mainly for historical reasons.

Depending on the composition, chalcogenide glasses commonly have high transparency in the 1-10 μm infrared (IR) wavelength regions. Their non-linear index of refraction is almost two orders of magnitude higher than that of silica glasses. Unlike in silica glass,

however, their characteristic low phonon energy allows many rare-earth transitions to occur without non-radiative quenching[25].

In recent years, chalcogenide glasses have attracted much attention due to their high photosensitivity. Photo-darkening and photo-expansion effects upon exposure at a wavelength corresponding to bandgap energy[19] have been a focus of research because of the high potential in developing a variety of holographic elements, such as microlenses[26], and grating and channel waveguides in bulk and thin films of chalcogenides[27].

Furthermore, contrary to the behaviors of other IR fibers, many chalcogenides[28] show good durability against water, various acids, and many solvents[29]. Their good water and chemical resistance make them stable enough for fiberization[30].

Arsenic sulfide fiber was chosen to be examined because of its better known properties[31, 32]. It is a strong glass former and therefore much easier for fiber drawing compared with the other chalcogenide glasses because of its better stability. More importantly, it is relatively stable and resistant to water and air for easy handling in typical application.

1.6. Photosensitivty phenomena in As_2S_3

Amorphous chalogenides have gained attention when they were discovered in 1954 by Goryunova and Kolomiets[33,34] that As_2S_3 exhibits semiconductor behavior. Additionally, amorphous chalcogenides also show various kinds of photo-induced changes in electrical, optical and photoelectric properties.

As_2S_3 is one of the chalcogenides with better known properties. Similar to As_2Se_3, its crystal form is made of 12-member rings in hexagonal layered structure, as shown in Figure 1-2. In the amorphous state, it is believed that the layered structure is preserved to the first approximation.

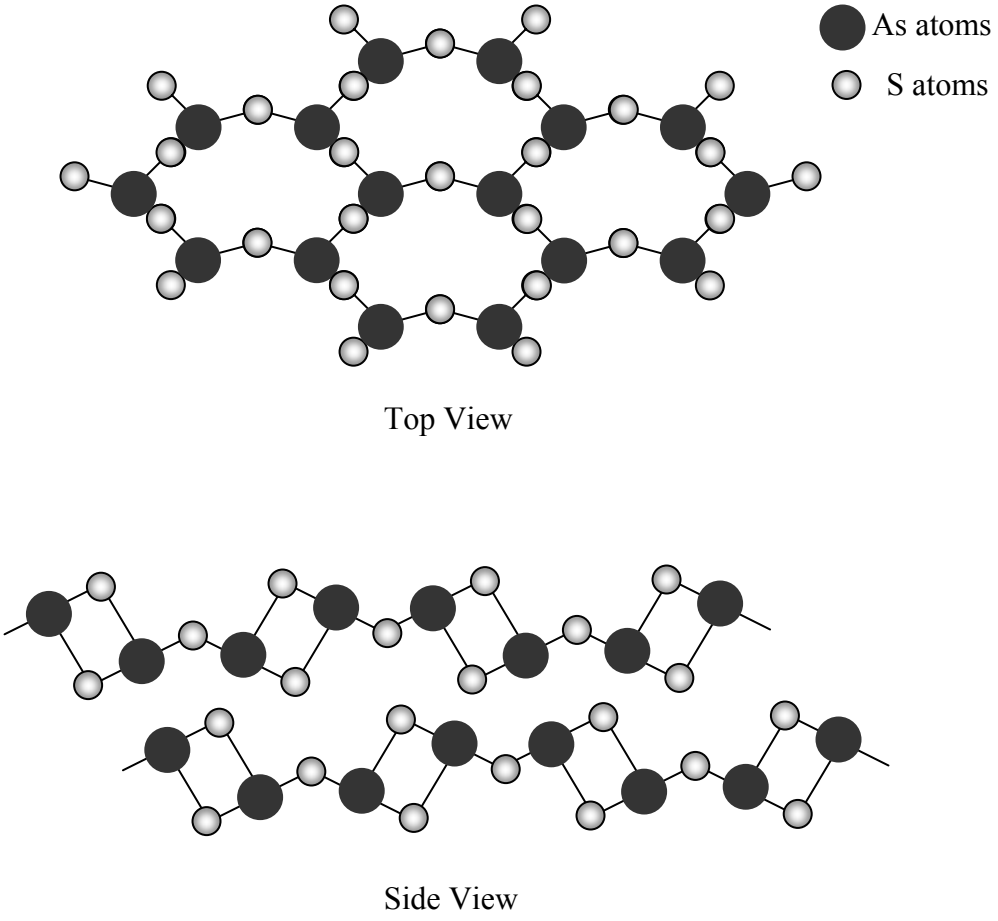

Figure 1-2 Layer structure of As_2S_3 crystal

In an "ideal" glass, all atoms satisfy the valence requirement, which also called 8-N rule when $N \geqslant 4$, where N is the number of valence electrons and coordination number is given by 8-N. However, As_2S_3 glass which should ideally contain only As-S bonds has been found to have up to 10 % homopolar bonds like As-As and S-S bonds in as made glass film[25] and one can increase the number of homopolar bonds by photon irradiation. Other researchers [35,36] have suggested that interaction between the lone-pair electrons and the bonding electrons of the neighboring chain may cause the formation of orbital-deficient

bonds. An empty orbital of a positively charged dangling bond would interact with lone-pair electrons of the neighboring chains, forming a threefold coordinated defect[37,38].

During the above non-radiative recombination in the presence of defects, energy would be used to modify the structure and properties of an amorphous material. There is a large variety of photoinduced metastable phenomena exhibited in amorphous semiconductors. In As_2S_3, it has been reported to exhibit photodarkening[39,40] and photoinduced volume change[41,42].

Photodarkening is the effect that the absorption edge of the material shifts to lower energy or longer wavelength on illumination[43]. Bond switching was thought to be the major cause of the process and bond-angle distortions also result from the bond switching[44]. Since these are metastable states, the photoinduced state can be destroyed either by annealing or by light illumination[45].

Photoinduced volume change of As_2S_3 film iss an indication of structural changes as a result of photoexcitation. One of the explanations claimed that light input energy to the system causing further disordering and the anharmonicity of the interatomic potential[41]. Another possible explanation is that “wrong” homopolar As-As bonds (2.57Å) are longer than heteropolar As-S bonds (2.24Å). However, S-S bonds (2.05Å) are indeed shorter than the heteropolar bonds. Thus, volume expansion may not be the consequence. It is believed that due to the photoinduced volume change, the density of the material was also being modified, forming the Bragg planes inside the fiber, which is an analog of the compaction/densification model discussed in Section 1.4.2.

1.6.1. Properties of arsenic sulfide

The typical properties of As_2S_3 glass are listed in Table 1-1[46, 47, 48]:

Table 1-1 Properties of As_2S_3 glass

Properties	Typical Composition	As_2S_3 or $As_{40}S_{60}$
Descriptive	Color	Yellow orange
	Crystal structure	Monoclinic
Physical	Density	3.2 g/cm^3 (crystal)
	Molecular weight	246.01 g/mol
Mechanical	Hardness (Knoop)	109
	Rupture modulus	2400 psi
	Young's modulus	2.3 x 10^6 psi
	Shear modulus	9.2 x 10^5 psi
	Poisson's ratio	0.24
Thermal	Thermal expansion coefficient	21.4 x 10^{-6} K^{-1}
	Thermo-optic coefficient	-8.6 x 10^{-6} K^{-1}
	Softening point	481 K (208 ^{o}C)
	Upper use temperature	423 K (150 ^{o}C)
	Glass transition temperature	453-470 K (180-193 ^{o}C)
	Annealing temperature	443K (170^{o}C)
Optical	Transmission window ($\alpha \leq 1$cm^{-1})	0.6-11 μm
	Absorption coefficient at 1.53 μm, RT	0.01 cm^{-1}

For a 3 mm As_2S_3 glass plate with polished surfaces, the optical transmission window is shown in Figure 1-3. The transmission increases rapidly at 0.6 μm and then decreases at around 10 μm. The glass does not transmit light beyond 13 μm. Note that depending on the purity of the glass, there may be transmission losses due to the absorption of H_2O and H_2S at around 3 μm and 4 μm, respectively. Also, beginning at 10 μm, the intrinsic multi-phonon vibrations cause transmission loss.

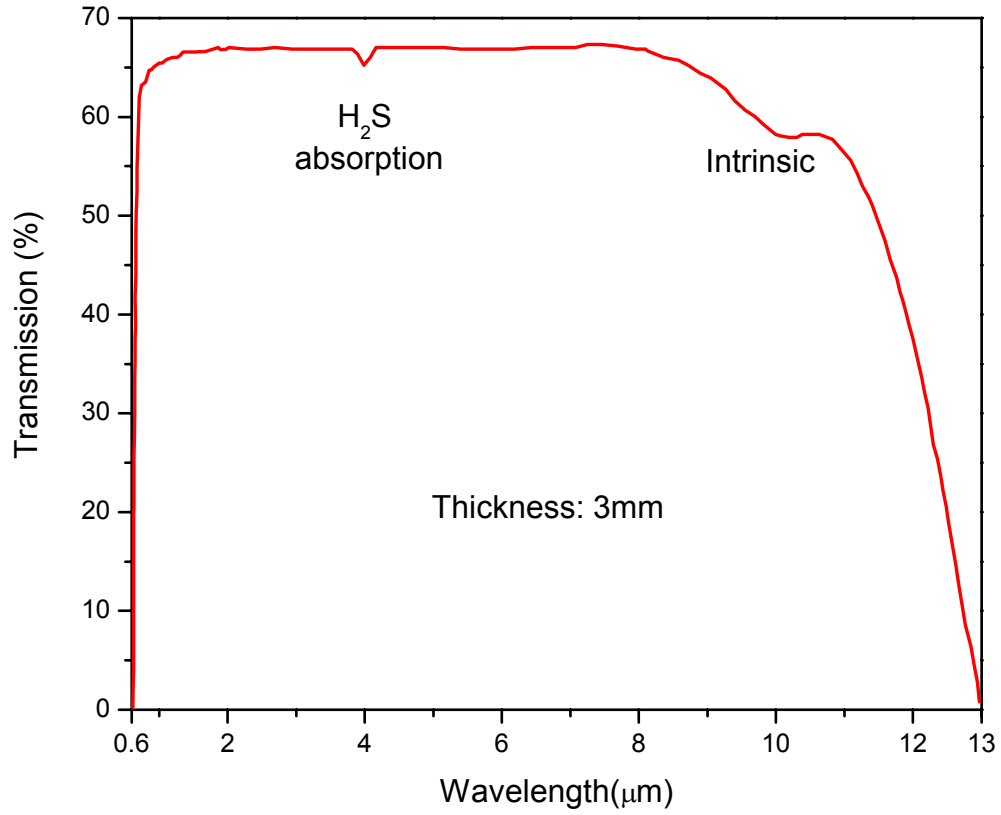

Figure 1-3 Transmission window of As_2S_3 glass[46]

Figure 1-4 is the plot of refractive index of As_2S_3 glass versus wavelength (taken from reference[49]). Refractive index decreases as the wavelength of incident light increases. Note that the refractive index at 1.55 μm where our optical experiment will operate is 2.43.

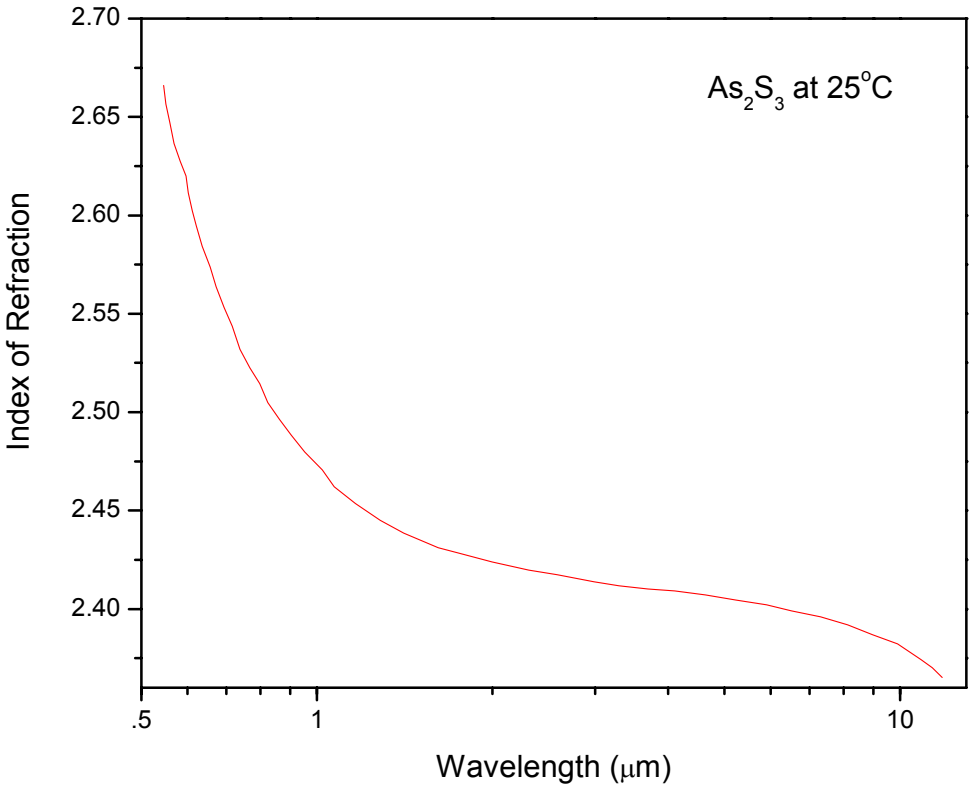

Figure 1-4 Refractive index versus wavelength of As_2S_3 glass [49]

In addition, more optical properties relating to the intrinsic window of As_2S_3 will be discussed at Section 1.8 below after a better understanding of the attenuation of optical fiber.

1.7. Optical fiber: single-mode and multimode behavior

Modes are stable patterns of waves which can travel through a waveguide. Their propagation depends upon the wavelength of the wave and the size, shape, and nature of the waveguide. The number of modes in a fiber can also be calculated by the waveguide parameter V[50]:

$$V = \frac{2\pi}{\lambda} a\left(n_1 - n_2\right)^{1/2} \qquad 1\text{-}5$$

where a is the core radius, λ is the wavelength, n_1 and n_2 is the refractive index of core and cladding respectively. For single-mode fiber, $0 < V < 2.4048$ and for multimode fiber, $V \geq 2.4048$.

Single-mode fiber sensors offer a higher sensitivity because they permit the user to construct guided wave interferometers directly from the fiber itself so as to measure small phase changes in light transmitted through the measuring region. This is achieved by comparing the phase of a light wave which has traversed a sensing path with the phase of another light wave originating from the same source, but arriving via a protected, reference path. The phase difference can be measured with a sensitivity of $\sim 10^{-6}$ of a wavelength, whereas the path length for the measuring interaction can be millions of wavelengths long. This leads to a possible measurement resolution for the optical path of one in 10^{12}. Simultaneously, the absence of free space optical paths between sources and detectors eliminates slow alignment drifts which could easily occur if bulk-optical interferometer had been used. In practice, single-mode fiber sensors need very stable, highly coherent sources with low phase noise in order to gain full advantage of their potential sensitivity. When such sources are used, absolute calibration of the phase difference is normally not possible and a range limit arises from the periodic nature of the interferometer output[26].

On the other hand, multimode optical fiber sensors have several advantages[51,52]. It is inexpensive to operate with substantial optical power over moderate distances. Utilizing the multiplicity of propagation modes, multi-sensing can be performed. Multimode sensors have higher tolerances with respect to end effects and interconnections because of the relatively larger dimensions.

However, one should also be aware of the drawbacks of using multimode optical fibers. They produce various intensity modulation outputs for transmission (including phase and polarization modulating elements), which are difficult to analyze. The variation of optical path length at different wavelengths in optical fiber systems have to be overcome.

Single-mode fiber is usually preferred by researchers for sensing applications. However, due to the unavailability of single mode chalcogenide fiber at the beginning of our project, multimode fibers were used in our study.

1.8. Loss mechanisms in optical fibers

Optical fibers suffer transmission losses just as any other transmission medium. Though it would not be as an important concern as for the communication applications where the fiber lengths are very long, in multiple kilometers, the attenuation or power loss of the FBGs should considered as the distributed FBGs will ultimately fabricated in the length of tens of kilometers for multi-spot scanning.

Mechanisms of attenuation[53] can be divided into two categories, the intrinsic and extrinsic fiber losses.

1.8.1. Intrinsic losses

Intrinsic losses include scattering and absorption losses which would persist even if other losses could be reduced to zero. Thus, they are the fundamental limiting losses in fibers.

Scattering

Rayleigh scattering arises as a result of random, microscopic variations in the index of refraction of the fiber core[53]. These irregularities, act as dipoles, and are excited by the incident light. Throughout this process, some incident power is being lost. The dipole radiates this power with the same frequency in any direction.

Absorption

There are two types of absorption, one located in the far-IR and the other located in UV region[53].

The former is dominated by the one-phonon lattice vibrational bands (the Reststrahl). Other features are also present and can be explained by processes in which a photon is absorbed by the lattice via interactions involving two or more phonons. Such effects are induced either by the anharmonicity of the fundamental phonon modes or by any non-linearity in the relationship between induced polarization and the stimulating electric field. For example, two-phonon lines can appear at the sum and difference frequencies of the phonons involved, with the sum frequency (corresponding to the creation of two phonons) appearing on the short wavelength side of the Reststrahl. The complete set of such 'sum resonance' tails off into the optic window from the top of the Reststrahl and makes up the multiphonon edge.

On the high-frequency side, attenuation of the optic window is dominated by band gap absorption which is primarily the result of one-electron excitations between the filled valence and empty conduction bands. In the simplest band scheme, it might be expected to 'cutoff' sharply at a wavelength corresponding to the energy gap between the top of the valence band and the bottom of the conduction band.

However, it is more complicated situation in a real material. First, the excited electron and the vacated 'hole' in the valence band are created at the same site and interact via an attractive electrostatic force. The consequence of this attraction is most pronounced near the band edge where bound electron-hole excitations can form and produce resonant absorptions below the conduction band. They are more pronounced for wide-band gap materials.

In addition to these electron-hole interactions, deviations of the lattice from exact periodicity would also be a factor of complications. Such deviations are present in the intrinsic limit, either via thermally excited lattice vibrations (in crystals) or by the essential nonperiodicity inherent in glasses at absolute zero.

In glasses, the lattice periodicity is naturally disrupted and is therefore not so markedly affected by temperature. The perturbation induced by the glass disorder is so predominant that near the valence and conduction band edges the 'band' description of electron actually cease to propagate as band electrons and become trapped in potential wells with a distribution of depths. The density of the localized states induced extends into the band gap from both the conduction and valence band ends to produce an Urbach tail that extends well into the optic window below the excitonic resonances. The precise mathematical form of the Urbach tail is still the subject of discussion in the literature[54, 55].

This weak Urbach tail arises from electronic transitions induced by defect states inside the gap. Defects in an amorphous context refer to a disruption of perfection in the topological pattern of bonding or coordination implied. By the concept of a continuous random network (CRN)[56], while proper annealing can control this weak tail to a degree by reducing the amount of defects, the tail is not necessarily of entirely extrinsic origin since its seems likely, in many cases, that the perfect CRN topology is not energetically the most stable glassy state, and the defects are therefore present as an essential component.

Intrinsic window

The intrinsic window, as shown in Figure 1-5[28], describes the theoretical loss minimum α_{min} of an optical material as a function of λ. It can be determined by the intrinsic attenuation processes that define the optical window[27].

$$\alpha_{\min} = \alpha_{Rayleigh} + \alpha_{multiphonon} + \alpha_{Urbach} \qquad 1\text{-}6$$

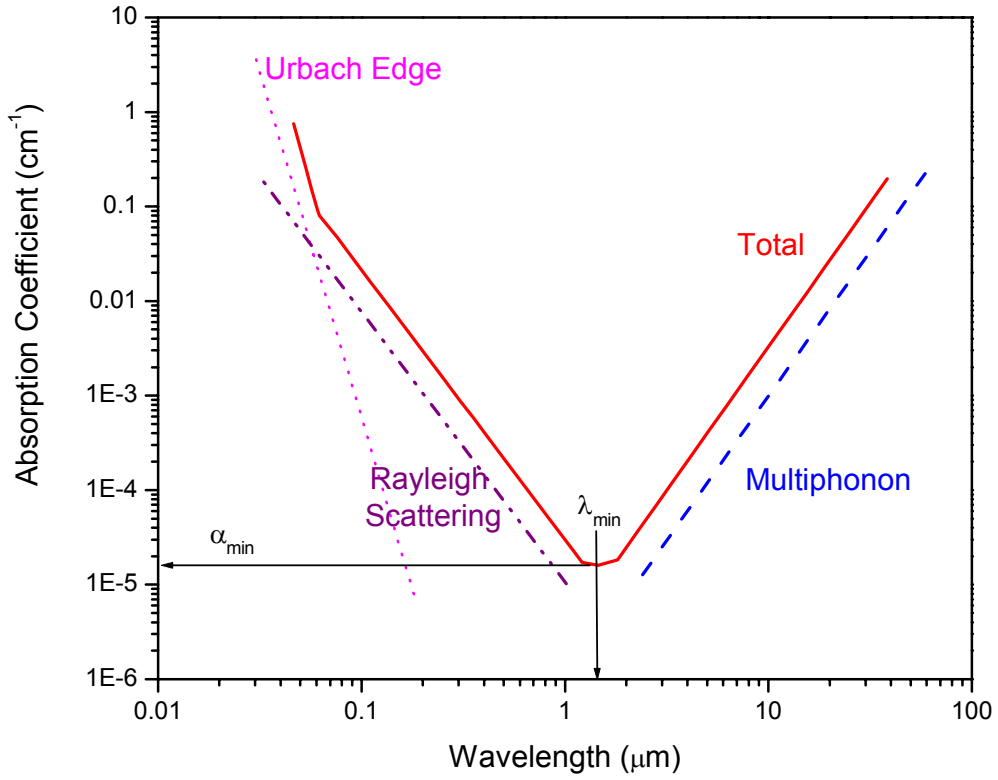

Figure 1-5 Optic window V plot[27]

Optical losses in sulfide glass fibers

The effect of the weak absorption tail on the transmission loss in As_2S_3 glass fiber was studied by Kanamori et al.[57] and his plot is shown in Figure 1-6.

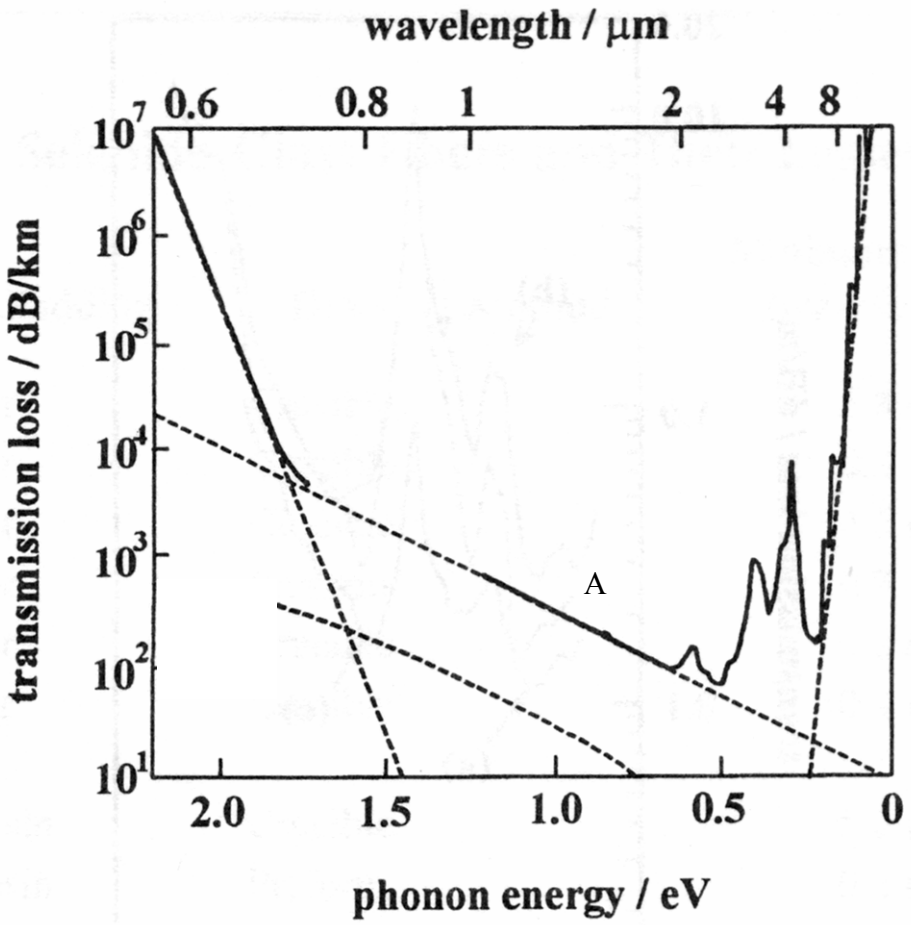

Figure 1-6 Photon energy versus transmission loss of As_2S_3 glass fiber[57]

The weak absorption tail is observed below the exponential part of the absorption edge (Urbach tail) and is due to transitions from localized states deep in the band gap to the extended states. Curve A is the estimated scattering loss by measuring Rayleigh's ratio R_{90} at 633 nm (He-Ne laser). The loss between 0.7 and 6 μm is assigned to the weak absorption tail. Consequently, the expected theoretical minimum loss of this fiber is estimated as 23 dB/km at 4.6 μm. It is suggested that the deep potentials states causing the weak absorption tail are associated with disorder, defects, and impurities. In our case, it may refer to the existence of As-As and S-S homopolar bonds in addition to the As-S bond which alone

determines the structure in a CRN model. The concentration of states[58] giving rise to the weak absorption tail is approximately 10^{16} to 10^{17} /cm^3. There is a possibility that the transmission loss characteristic of As-S glass can be considerably improved if the concentration of defects and impurities can be minimized.

The absorption bands due to contaminant such as OH and SH impurities at 2.9 and 4.1 μm respectively. The researchers suggested that the amount of SH could be minimized by the distillation of sulfur under an S_2Cl_2 stream, and a minimum loss below 0.2 dB/m was attained near 2.6 and 4.6 μm, which is 10 times larger than the theoretical minimum.

1.8.2. Extrinsic losses

Extrinsic/Induced losses are attributed to the imperfections and impurities within the fiber. Optical beams passed through geometric irregularities, bends or microbends form a propagation angle exceeding the critical angle and thus result in loss. Design and processing of fibers are aimed at reducing these losses as much as possible.

Point defects, dislocations, grain boundaries, and impurity atoms can all create electronically active states within the band gap that enable significant low energy absorption to occur in what would, in their absence, be a highly transparent wavelength regime. The major impurity absorption bands in As_2S_3 glasses are tabulated in Table 1-2:

Table 1-2 Impurity absorption bands in As_2S_3 glass[28]

Wavenumber (cm^{-1})	Wavelength (μm)	Assignment
925	10.81	AsO-H
1825	5.48	AsO-H
3440	2.91	SO-H
4370	2.29	SO-H
5210	1.92	SO-H
6950	1.44	SO-H
1580	6.33	H_2O
3610	2.77	H_2O
2480	4.03	S-H
2710	3.69	S-H
3215	3.11	S-H
3940	2.54	S-H
4880	2.05	S-H
2025	4.94	Carbon

Hydrogen is the most problematic of impurities of IR fibers as it reacts to form hydroxyl ion (OH^-) and H_2S.

1.9. FBG fabrication: interferometric technique

Different techniques of inscription of Bragg gratings in silica optical fibers have been reported, such as internal inscription[59], interferometric techniques[60], phase-mask techniques[61], point by point fabrication[62], etc.

Internal inscription was the first method reported to inscribe FBGs and was demonstrated by Hill et al. using Ge-doped SiO_2 fiber and Ar ion laser (514.5 nm)[59]. A standing wave intensity pattern was formed by the interaction between the transmitted beam and back-reflected beam within the fiber. At the point of constructive interference, index of refraction in the photosensitive fiber was modified and Bragg gratings were obtained.

Point by point fabrication is done by inducing refractive index change one step at a time using pulse laser along the fiber core which eventually forms the grating structure[63].

The phase mask technique is the easiest and most common technique to inscribe FBGs in photosensitive fibers. The transmitted plus and minus first orders formed behind the phase mask interfere and high contrast fringe pattern will result to induce refractive index change in

the core of the fiber. This is an appealing method because of its simplicity. For fabrication of SiO_2 fiber, the period of the phase mask should be in between about 1013 nm to 1090 nm for FBGs to be written at 1520 nm to 1580 nm while the period we need to write FBGs in As_2S_3 glass fiber should be 633 nm to 659 nm. As a result, we were not able to obtain a phase mask commercially at the earlier stage of our research due to the unsophisticated technology. By the third year of our research, phase mask companies were found the could supply the phase mask with lower period and therefore we also tried the phase mask technique.

Interferometry can be used to inscribe FBGs by first splitting the laser radiation into two beams of equal intensity that were coherent and then recombined to produce an interference pattern, normal to fiber axis. This technique is flexible because it requires only optical parts and FBGs wavelength is flexible based on the set-up of optical parts. However, it is susceptible to mechanical vibration. Submicron displacement in any optical parts will result in drafted interference fringe pattern, washing out the gratings. Excellent spatial and temporal coherence, laser stability and air currents are factors affecting the quality of the FBGs.

Therefore, we first tried the interferometric techniques at the beginning of the project because of the flexibility of the experiment set up. At the later time, we also tried phase mask technique to inscribe FBGs.

1.10. Bragg gratings inscription in As_2S_3 single mode fiber

Since Asobe et al.[64] had demonstrated the FBGs writing in single mode As_2S_3 fiber using the holographic method, we tried to use similar set-up to inscribe FBGs. Their result was shown in Figure 1-7 and Figure 1-8. The FBGs showed at 1539 nm with reflection 80% after 14 min radiation and the FWHM is 1 nm.

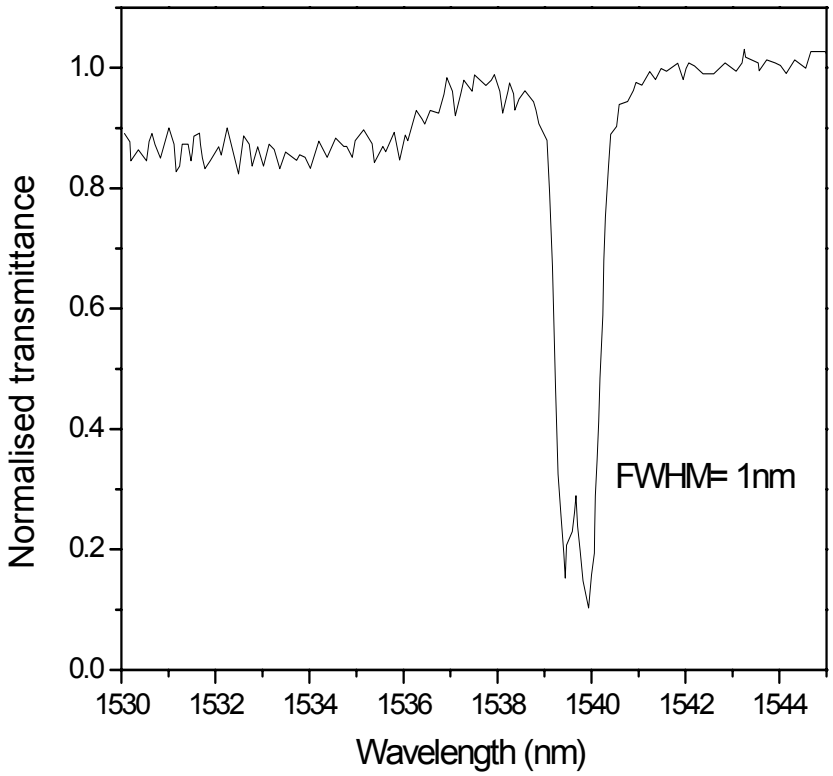

Figure 1-7 Transmission of the As_2S_3 fiber Bragg gratings in single mode fiber from Asobe et al.

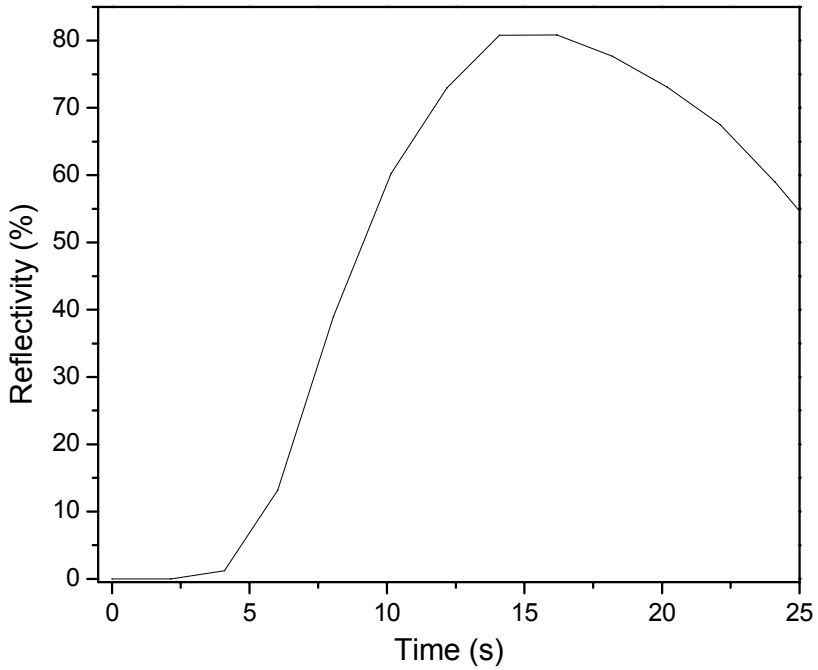

Figure 1-8 Reflectivity of As_2S_3 FBGs versus irradiation time from Asobe et al.

1.11. Bragg gratings inscription in SiO_2 multimode fiber

Mizunami et al.[75] has studied and reported the FBGs in multimode SiO_2 optical fiber. They used two different light sources to characterize the same FBGs written in a graded-index multimode fiber. In Figure 1-9, the transmission spectrum was obtained by LED with a single mode fiber pigtail as low order mode excitation source. Four reflection wavelengths appeared and the maximum reflectivity was 96.6% at 1559 nm.

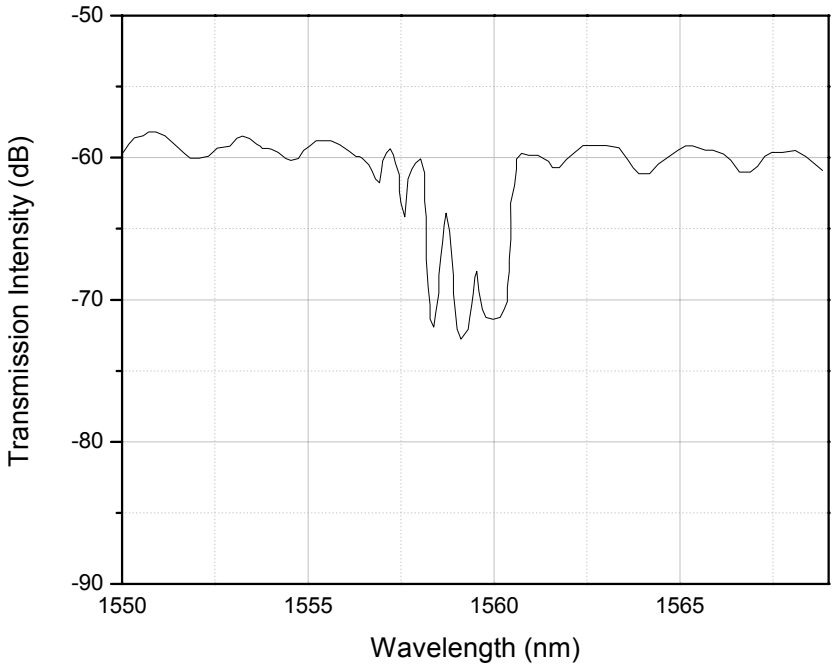

Figure 1-9 FBGs in multimode SiO_2 fiber for lower order mode excitation from Mizunami et al [73]

In Figure 1-10, a halogen lamp was used as the light source, which excited higher order mode. 19 dips appeared with maximum reflectivity 36% at 1551.8 nm.

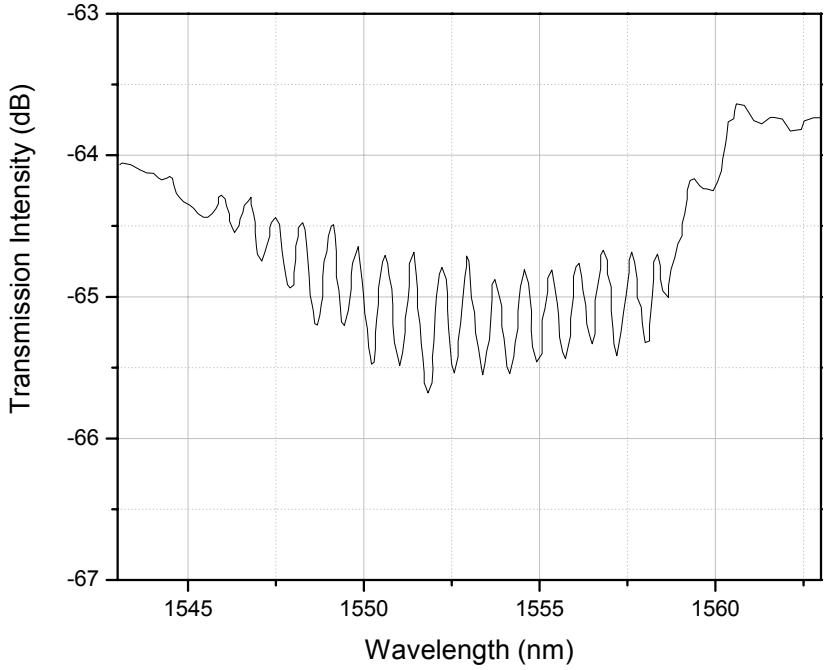

Figure 1-10 FBGs in multimode SiO_2 fiber for higher order mode excitation from Mizunami et al[73]

These multiple transmission dips in both cases do not arisen from coupling to the cladding modes, but the reflection of same mode and neighboring modes. Also, the wavelength separations between the neighboring dips are 0.7 nm and 0.8 nm respectively in Figure 1-9 and Figure 1-10, suggested that the mechanism of reflection by a Bragg grating in multimode fiber does not depend on mode excitation condition.

On the other hand, Sang et al.[65] has shown the growth dynamics of FBGs in step index multimode SiO_2 fiber using phase mask technique. Standard step-index multimode fibers with a core diameter of 50 mm and a numerical aperture of 0.22 were used in their experiment. Also, Narrowband KrF excimer laser operated at 248 nm was used, with energy density per pulse and repetition rate equal 150 mJ and 10 Hz respectively. Their experimental results are shown in Figure 1-11.

Four transmission dips appeared and the width of each dip increased and these dips overlapped each other as number of irradiation pulses increased. Also, Bragg wavelength shift towards longer wavelength as the refractive index changes during the FBGs writing process.

Moreover, if there is a tilt between the fiber and the phase mask, the cladding mode tended to couple to the radiation modes and resulted in poorly defined transmission dips. In Figure 1-12, the researchers showed the transmission spectra of 4.5^{o} tilted FBGs.

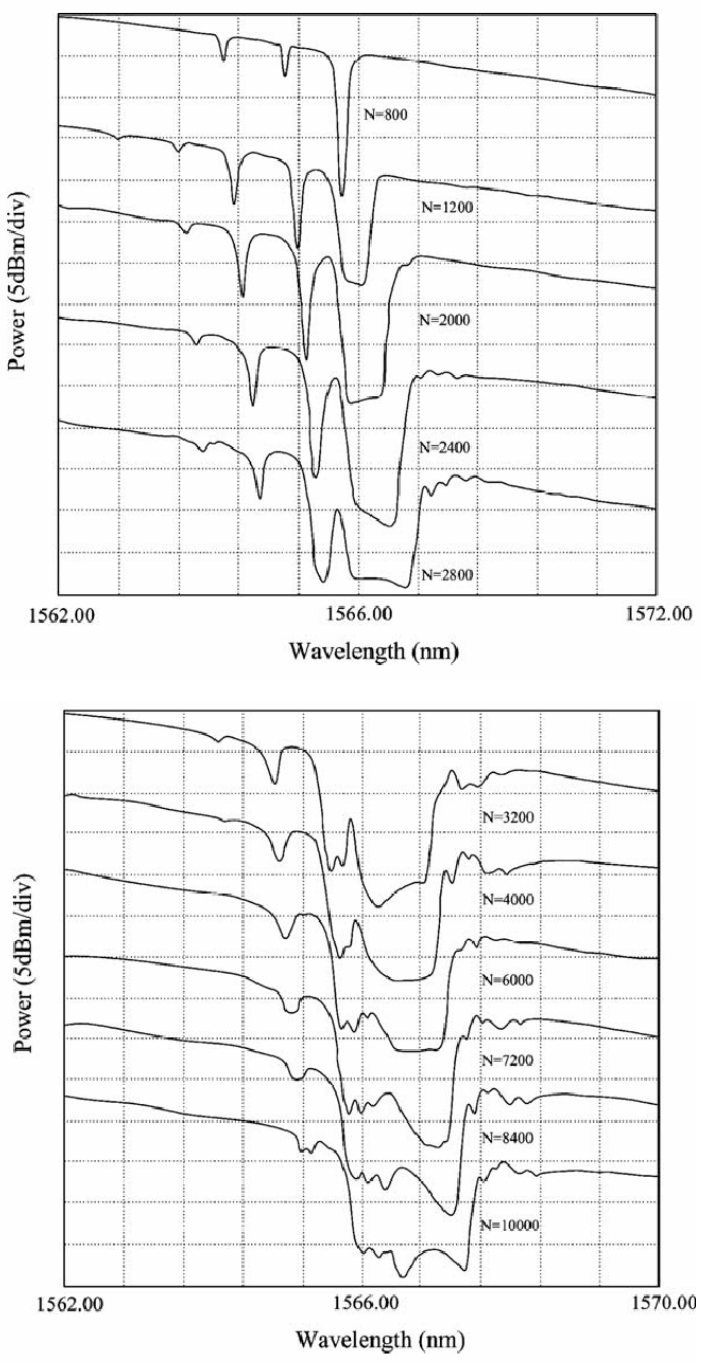

Figure 1-11 Growth dynamics of FBGs in multimode SiO_2 fiber using KrF laser (150 mJ, 10 Hz)[65]

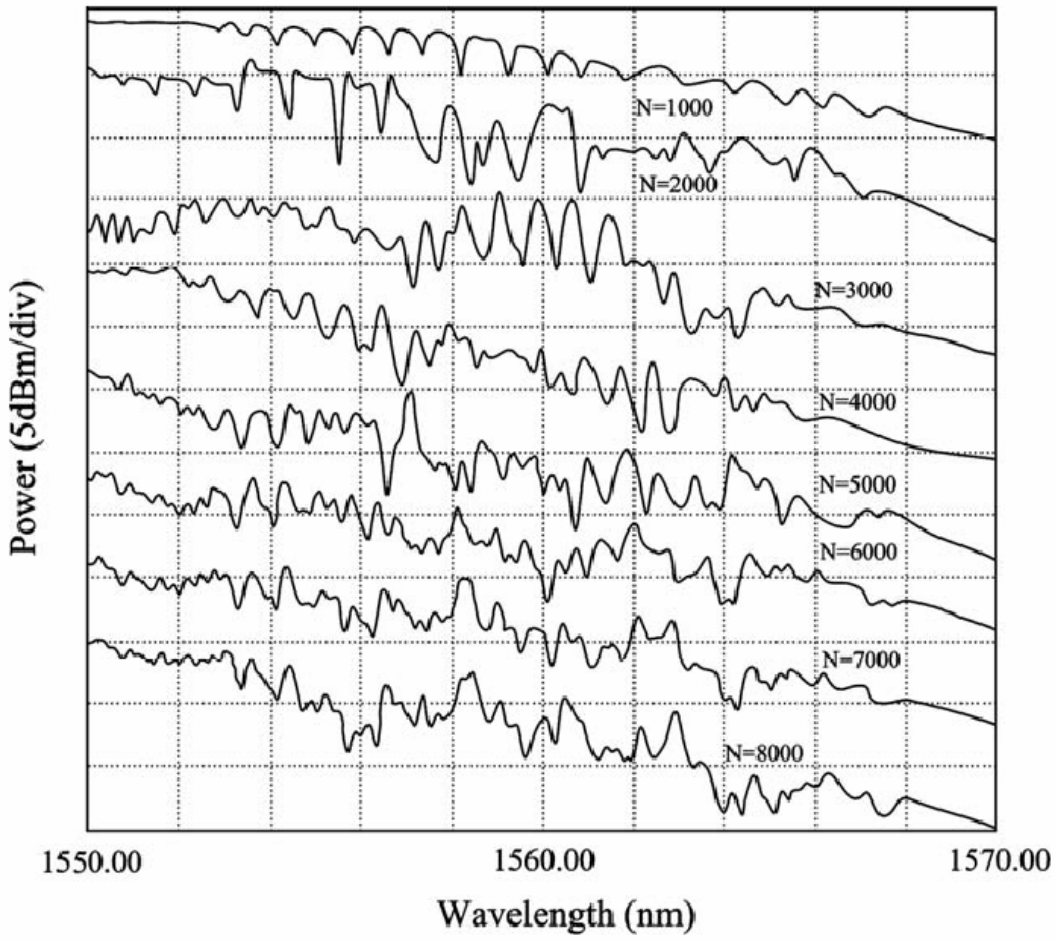

Figure 1-12 FBGs in multimode SiO_2 fiber[65], tilted angle = 4.5^o

2. Materials preparation

2.1. Preface

It was originally thought that the commercial single-mode As_2S_3 fiber would be used throughout the project. While multimode fiber (Number of modes > 10000) can be found from many sources, we could not find single-mode fiber. Glass preparation and fiber drawing became necessary in the project while we were also actively looking for an alternate supplier for single mode fiber.

There are some technical papers discussing the fabrication of As_2S_3 single mode fiber that we tried to replicate. We collaborated with Clemson University for a fiber drawing experiment. Due to the limitation of their facilities, only the core-clad technique could be employed and we tested the fiber drawing experiment once using core only preform.

In order to fabricate As_2S_3 single mode fiber, the purity of glass has to be assured for high transmission. Work was done on preparing high purity As_2S_3 glass and good quality performs. Purity of the glass has been improved by first purifying the raw material followed by distillation process.

While we were working to improve our perform, the fiber drawing tower at Clemson University underwent moving and upgrade, which delayed the fiber fabrication process.

Knowing that our goal is to write and test the FBGs, when we found that the A.R.T. Photonics GmbH group from Berlin, Germany could provide us some multimode mode As_2S_3 fibers, we decided not to continue the fiber drawing experiment and work on the commercial few mode As_2S_3 fibers.

In this section, the work on making the As_2S_3 glass, including the purification experiment and characterization of the glass are reported.

2.2. Preparation of As_2S_3

As reported by many researchers, commercial grade As_2S_3 (99.9%) cannot be used as perform materials since the impurity concentration in fiber is very high. We started with arsenic metal pieces (0.99999) and sulfur powder (0.999999). However, each raw element is slightly oxidized or hydrated when received. Therefore, it is essential to purify the elements before batching the glass.

2.3. Materials characterization

To ensure the right composition of glass, several characterization techniques have been employed, including Raman and IR spectroscopy for structural analysis and differential scanning calorimetry for thermal analysis.

2.3.1. Structural analysis - Raman spectroscopy

Raman spectroscopy was performed on glass powder samples using a Bruker RFS-200/S FT-Raman Spectrometer and a Nd:YAG Laser operating at 1064 nm as the excitation source. The powders were placed in aluminum holders and sealed with clear packaging tape. The spectra were collected using a 180^o backscatter experiment at powers of typically 50 to 100 mW with a resolution of 2 cm^{-1}.

Figure 2-1 shows the Raman spectra of As_2S_3 prepared and compared with the commercial grade As_2S_3.

As_2S_3 glass has a broad absorption peak at 340 cm^{-1} and arises from the $AsS_{3/2}$ pyramid structure. The weak band at 495 cm^{-1} is attributed to S-S bonds. Other weak bands in the range of 180 cm^{-1} to 220 cm^{-1} can be attributed to $AsS_{3/2}$ pyramids, S_8 and As rich As_4S_4 molecules[66].

As_2S_3 with 1% and 2% excess S have very similar spectra as the commercial grade As_2S_3. However, for 0% excess S, a peak of As-riched phase As_4S_4 appeared at 360 cm^{-1} in Figure 2-1. This indicated some sulfur has been lost during the reaction, possibly because of the high vapor pressure of the sulfur.

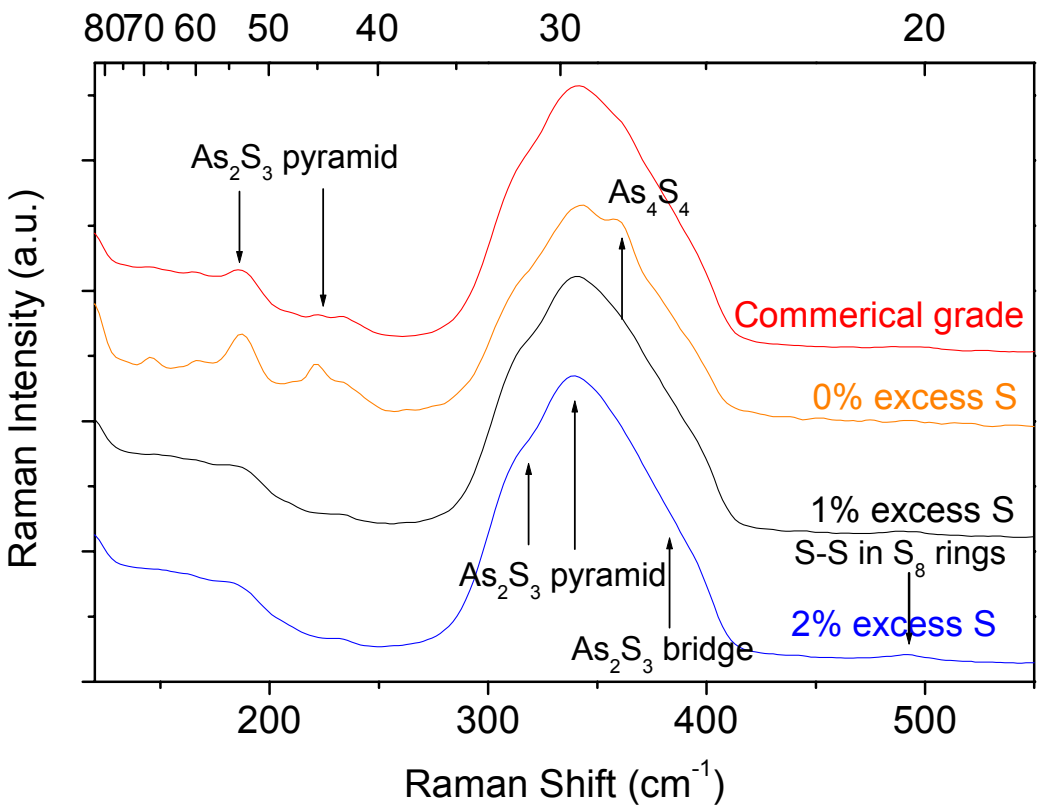

Figure 2-1 Raman spectra of As_2S_3 prepared in CsI pellet form

2.3.2. Structural analysis - infrared spectroscopy

Infrared spectroscopy was performed using a Bruker IFS 66v/S spectrometer. The spectra were measured in the mid-IR spectral range of 4000 to 400 cm^{-1} and in the far-IR range of 600 to 120 cm^{-1} with a resolution of 4 cm^{-1}. CsI pellets and glass plates ~ 1.5 mm thick were used for both the mid- and far-IR measurements. Pellets were made for transmission by mixing approximately 2-3% of sample by mass with dried CsI powder.

Figure 2-2 shows the far IR spectra of As_2S_3 prepared and can be used to compare with the result taken from the Raman spectroscopy.

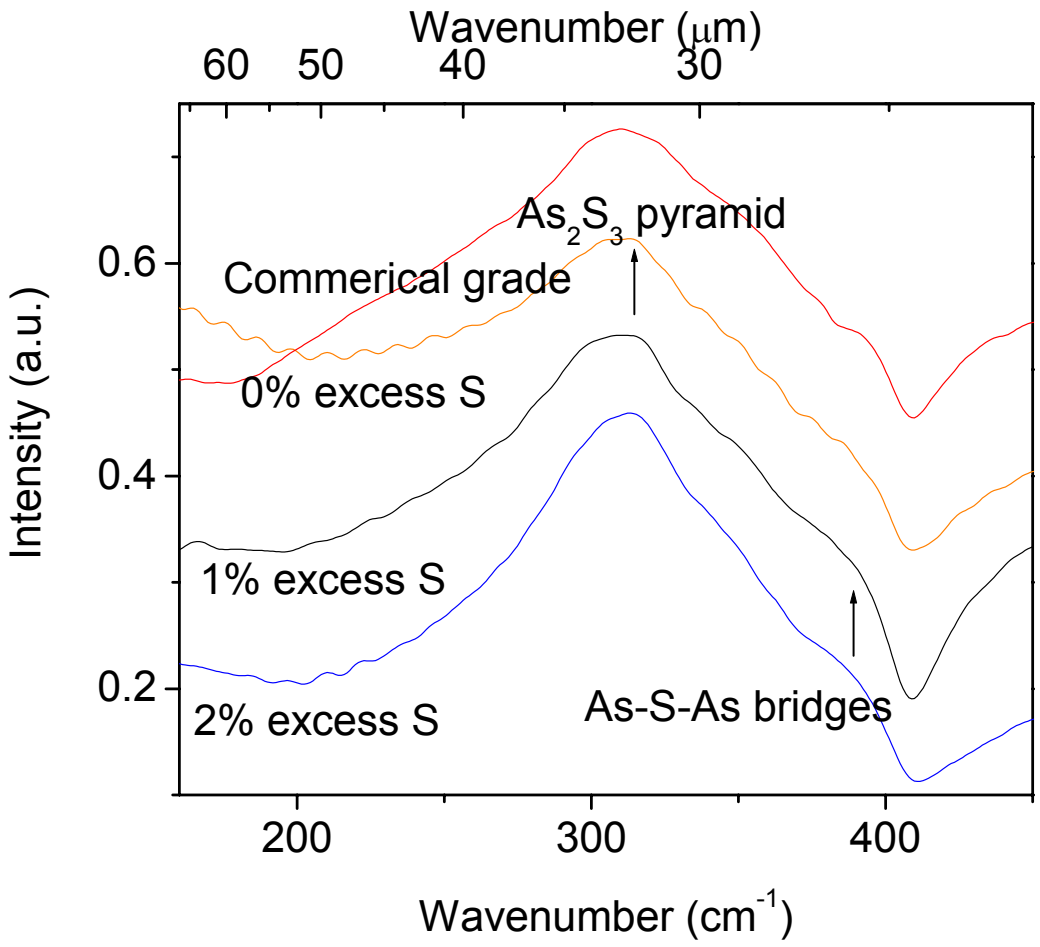

Figure 2-2 IR spectra of As_2S_3 prepared in CsI pellet form

In IR spectra, 4 types of As_2S_3 glass resemble each other, There is a broad absorption peak at 300 cm^{-1} and 313 cm^{-1} and are contributed by the $AsS_{3/2}$ pyramid structure. There is also a peak appeared at 390 cm^{-1} which is attributed from As-S-S bridge.

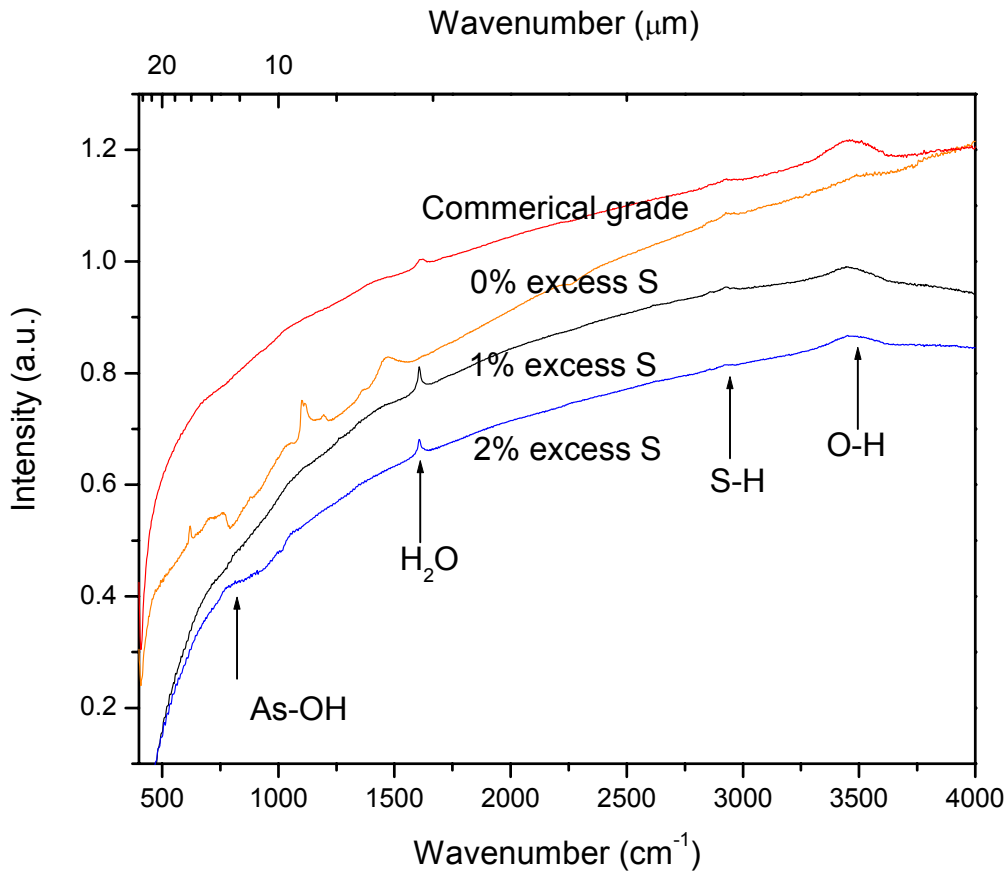

Figure 2-3 IR Spectra of As_2S_3 prepared in CsI pellet form

Since most of the impurities would absorb at mid infrared range, Figure 2-3 shows the presence of impurities inside the glass. Absorption bands attributed to impurities such as As-OH (813 cm^{-1}), O-H (1590 cm^{-1}, 3481 cm^{-1}) and H_2S (2925 cm^{-1}) are also observed.

Compared with the commercial grade As_2S_3, samples prepared from pure elements have higher content of impurities. This indicates that the purification of raw materials is essential.

2.3.3. Thermal analysis

Glass transition temperature measurements were performed using a Perkin-Elmer Pyris Diamond DSC. Approximately 15 mg. of glass powder was hermetically sealed in aluminum

samples pans. The samples were measured from 50 to 250°C at 10° C/min. The thermal characteristics were determined by measuring the onset of each thermal event.

Figure 2-4 shows the DSC scan of As_2S_3 glass. Since As_2S_3 is an excellent glass former, no crystallization peaks could be found above T_g while a very sharp glass transition can be observed.

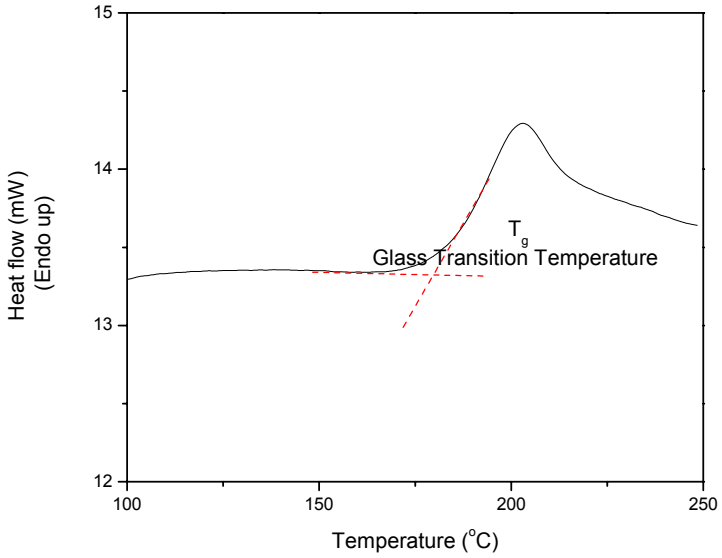

Figure 2-4 DSC scan of As_2S_3 glass

The glass transition temperatures of As_2S_3 with different amounts of sulfur content are tabulated in Table 2-1.

Table 2-1 Glass transition of As_2S_3

Sample	Glass Transition Temperature (°C) ± 1 °C
Commercial grade	193
As_2S_3 + 0% excess S	175
As_2S_3 + 1% excess S	194
As_2S_3 + 2% excess S	189
As_2S_3 + 5% excess S	194

Besides the 2% excess S content glass, it showed an increasing trend between the glass transition temperature and the amount of sulfur added during the preparation.

As a summary, Raman spectra showed that slight amount (1%) of excess S should be added to the batch materials to prevent As rich compound.

2.4. Purification

After we confirmed the batch composition for As_2S_3, we purified the raw materials in order to get better quality As_2S_3. Arsenic metal was sublimed while sulfur powder was reacted with S_2Cl_2.

2.4.1. Arsenic sublimation

Since arsenic oxides have a higher partial pressure than arsenic metal, removal of arsenic oxides can be done by heating the as-received arsenic at 300°C under a vacuum of a 10^{-5} torr[29]. The arsenic oxides sublime and then deposit in a cooler region of the system. The diagram of the experiment can be seen in Figure 2-5:

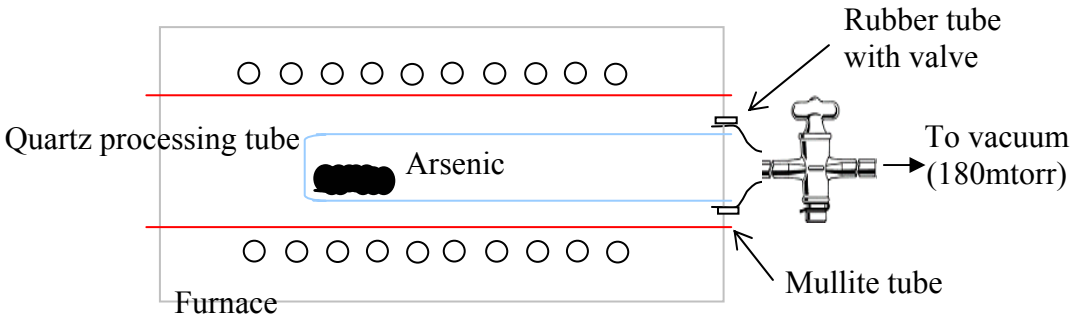

Figure 2-5 Experimental setup for purifying arsenic metal

2.4.2. Sulfur reaction

Sulfur was purified by passing S_2Cl_2 through liquid S under vacuum at 150°C for 12 hours as shown in Figure 2-6. During the purification, the following reaction was carried out.

$$2\ S_2Cl_2\ (l) + 4\ H_2O\ (s) \rightarrow 2\ SO_2\ (g) + 4\ HCl\ (g) + 2\ H_2S\ (g)$$[57]

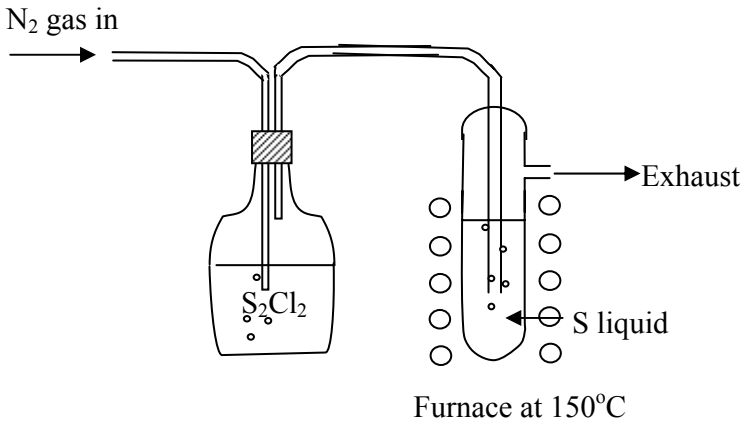

Figure 2-6 Experimental set up for purifying sulfur[57]

2.5. Batching and glass reaction

After measuring the appropriate amounts of As and S inside a high quality N_2 glove box, the two elements were mixed and sealed under vacuum in a quartz tube. Then quartz tube was heated up to 550°C at a heating rate of 1°C/min and held for 10 hours. After that, the sample was annealed at 205°C for 8 hours and then cooled down to the room temperature. After the melting process, small pieces of unreacted arsenic were seen inside the glass matrix. Also, many cracks were present such that only small pieces of As_2S_3 could be obtained, possibly because of the relatively large thermal gradient inside the small box furnace and also because of the large thermal expansion coefficient of the glass. The heating process was further improved by using a split tube furnace with thermal gradient less than 1°C to eliminate the factor of thermal gradient. In addition, a pre-annealing stage above glass transition at 220°C has been added to the melting process to relieve the stresses inside the glass caused by cooling.

To promote complete reaction and improve the homogeneity of the glass, the heating temperature was increased to 800°C and ampoule was manually rocked during the melting process. Since the ampoule was reacted either horizontally or at a slight incline, large portions of the glass reacted was not in the desirable rod shape. To prepare a better rod shaped perform, the ampoule was then heated inside a box furnace where the sample tube

was held vertically so that the glass would flow into a vertical rod shape. The final heating profile is shown in Figure 2-7.

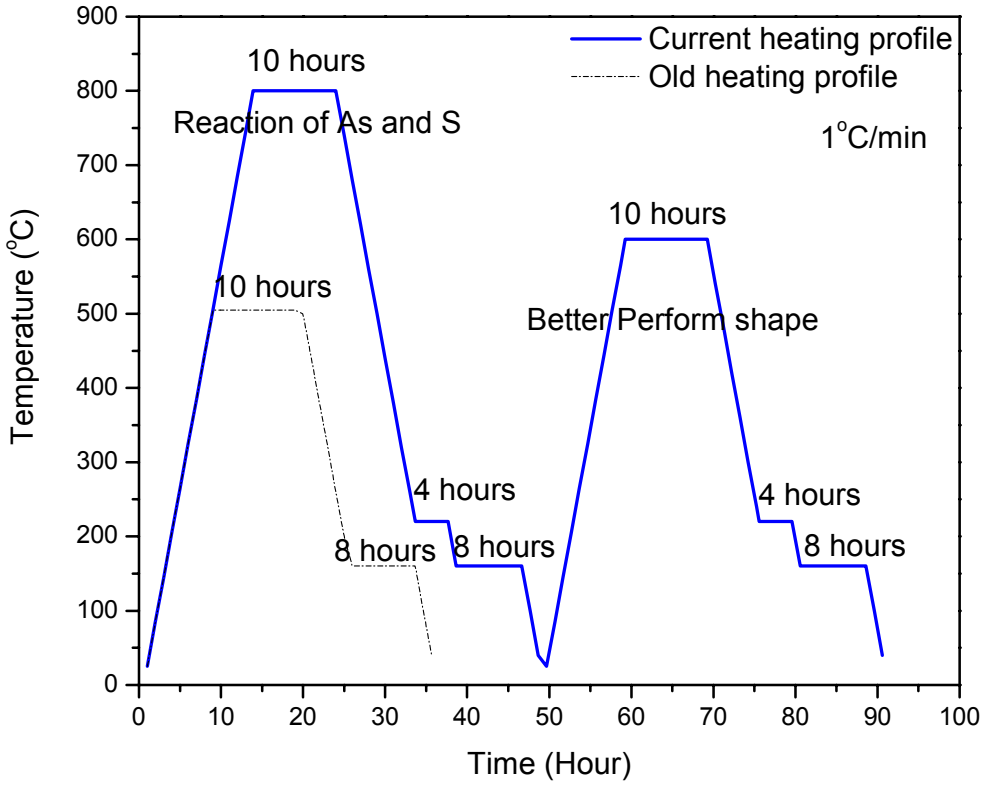

Figure 2-7 Heating profile of the glass

The rod shape sample was taken out from the quartz ampoule. Thin glass plates at ~ 1 mm thick were cut from the sample for characterization. The remaining rod was used as perform for fiber drawing.

2.6. Effect of purification

After the purification process, arsenic pieces change to a more silvery appearance, with white arsenic oxides condensed at the cooler part of the processing tube. With increasing reaction time, metallic arsenic will also sublimate and condense at the cooler part of the furnace.

Even though the appearance of arsenic powder changed, the IR spectrum of pure As does not show any significant difference. This may be due to the method of characterization. Since IR samples were prepared inside the glove box and after that they were taken out and characterized using the IR spectrometer, purified As metal may become hydrated again. In addition, the thickness of the samples cannot be assured to be the same, which give rises to the inaccurate impurities content measurement. To solve the problem, polished glass plates at ~ 1.5 mm thick were used to measure the impurity content. Comparison of IR spectra of As_2S_3 prepared from unpurified and purified elements was shown in Figure 2-8. The factor of thickness has been taken into account when plotting the graph so that the peak amplitude is directly related to the concentration of the present species and spectra were offset for better presentation.

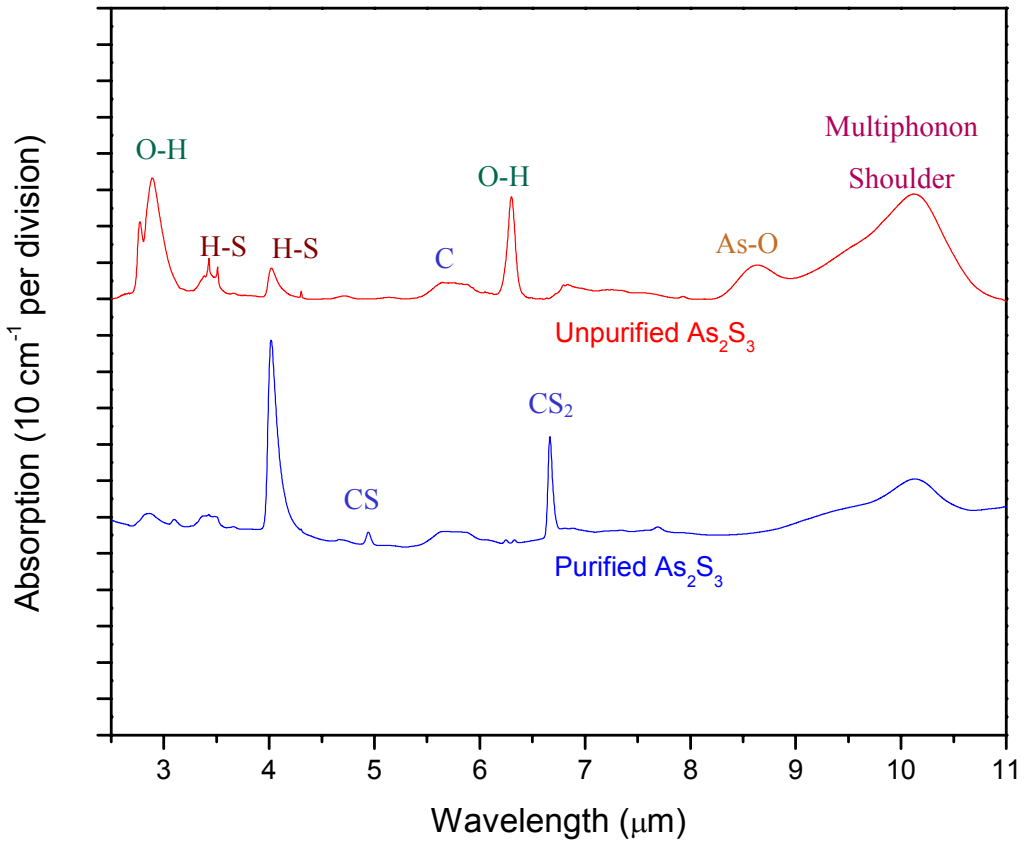

Figure 2-8 Comparison of IR spectra of As_2S_3 prepared from unpurified and purified elements

As we can see in Figure 2-8, the intensity of oxide and O-H peaks are significantly reduced for As_2S_3 prepared from purified As and S. However, the H-S peak has increased in intensity. This may be due to the ineffective removal of H_2S after the purification of sulfur. To solve the problem, it may help to evacuate the processing tube after the reaction of sulfur to get rid of the trapped H_2S gas.

Through the two purification experiments, carbon impurities can still be found possibly came from handing and also the environment. To eliminate carbon or other impurities, the batching materials have to be distilled in the presence of an oxygen getter. Details of the distillation experiment will be discussed in Section 2.8.

2.7. Fiber fabrication

2.7.1. Introduction

A attempt was made at Clemson Univeristy to draw fiber from 40 mm long, 10 mm diameter preforms were first prepared and multimode core-only fiber.

The performance of optical fibers, specifically, the transmission losses, bandwidth, and strength is strongly influence by the fiber drawing and coating processes. These processes must be treated as an integrated operation designed to impart desired properties to the resulting fiber. The essential components of the fiber draw process are consist of a feed glass rod, a heat source, a fiber-diameter monitor, a coating applicator, a curing apparatus, and a fiber puller and winding mechanism. A schematic of a fiber drawing tower is shown in Figure 2-9:

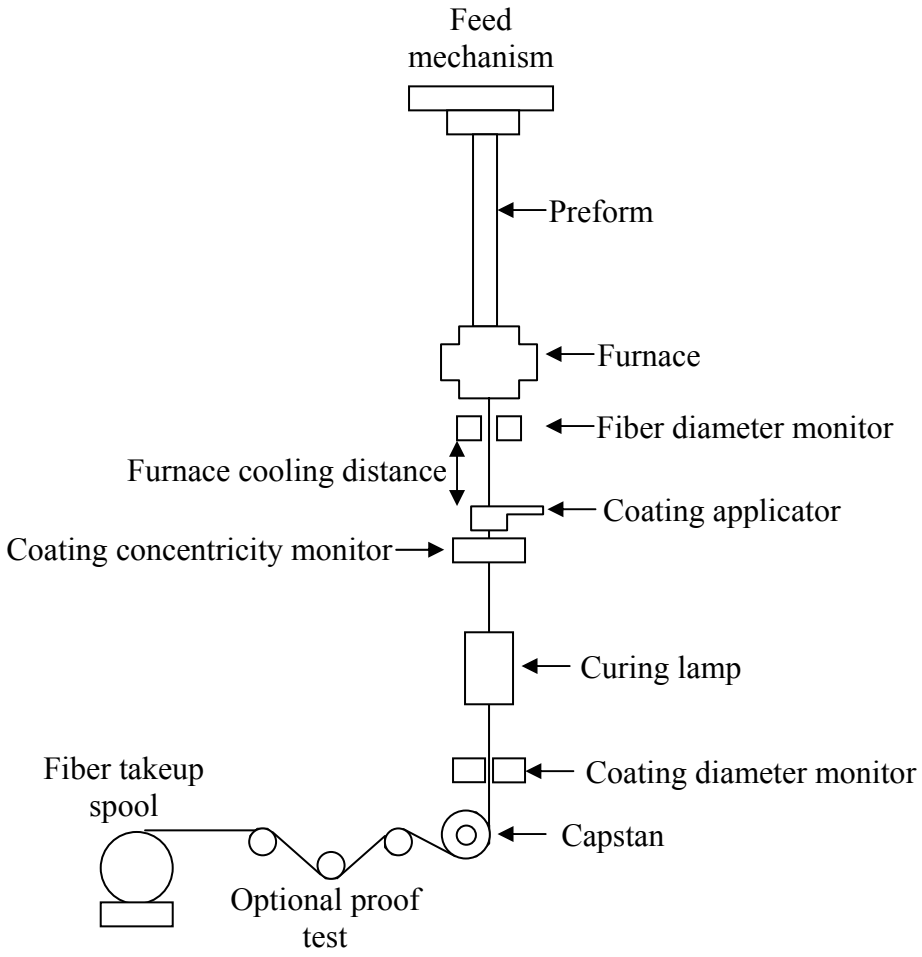

Figure 2-9 Schematic drawing of fiber drawing tower

Performs 10 mm in diameter and 40-50 mm in length were fed at speeds of 1.8- 2.1 cm/min in order to get fiber ~ 125 μm in diameter.

Fiber drawing begins by heating the tip of the perform to a molten state and allowing it to extend under the force of gravity downward while shrinking in diameter into a fine-diameter filament without the use of any die mechanism. A pulling and winding mechanism sustains a drawing force. The fiber diameter is monitored continuously as the fiber is drawn. Any variance of the fiber's diameter is detected by a control device that automatically readjusts the temperature and or the speed of pulling to compensate for the initial changes.

It has been found that the strength of the fiber is strongly affected by the quality of the silica glass tubing used for preparing the preforms. Any foreign inclusions or other defects

on the inside surface of the silica tubing used to prepare the preform, causes defects on the perform surface, which in turn can cause a reduction in strength. Cleanliness and temperature stability of the draw furnace also affect the fiber strength. Further, the drawing process is particularly vulnerable to atmospheric particle contamination during drawing because upward flow of air through the furnace by convection can cause particles to fuse to the surface to the molten glass thus greatly reducing the tensile strength of the fiber. It has also been established that greater strengths can be attained when relatively high drawing temperatures are used. When the fiber exits the furnace, it immediately enters the coating applicator. The fiber was coated with a UV-cured polymer DESOTECH 3471-3-14 to prevent contamination and mechanical damage[67]. The fiber was then wound onto a fiber take up spool at a winding stage.

2.7.2. As_2S_3 fiber drawing experiments

The As_2S_3 perform started to neck down at 400^oC and elongated under its own weight and formed a protruding section. However, the mechanical properties of the fiber were poor and the drawn fiber broke very easily. Only 1 out of the 4 performs brought to Clemson University were successfully drawn into fiber and this fiber was coated and reached the fiber take up spool. Very low yield of fiber was obtained due to the loss of the first drop of glass and continual breakage of the fiber. Bubbles and impurities can be seen within the fiber, which contribute to the reduction in the fiber strength. Also, these imperfections are considered to increase the transmission loss.

Since the fiber drawn at the first time was mechanically poor, we needed to further improve the quality of preforms.

2.7.3. Core-clad fiber perform

Because of the dispersion, the transmission loss of core-only optical fiber is higher than that of the core-clad fiber. Therefore, besides improving the quality of the perform, it is also essential to draw the fiber with a core-clad structure. It will be attempted to prepare the single-mode core-clad perform in the way suggested by Kobelke[68]. Here the cladding part can be prepared by drilling a hole with diameter of 1.5 mm at the center of the cladding glass

rod with an outside diameter of 10 mm by hypersonic drilling. Core glass with diameter 1.45 mm can be prepared by the double crucible fiber drawing method. After that, the core glass was inserted into the cladding glass rod and was used for the fiber drawing.

2.8. Distillation of arsenic and sulfide

To eliminate additional impurities beyond that of water and oxide, distillation was used[69]. Dehydrated quartz process tubes are used for the distillation. The batched pure elements are sealed under vacuum with the addition of a small amount of Mg as an oxygen getter. Mg has a lower free energy of formation of oxides than those of the chalcogen elements. After that, the ampoule is heated to ~ 600^{o}C whereupon the pure elements sublime and condensate at the unheated part of the sealed tube where they could be collected (Figure 2-10).

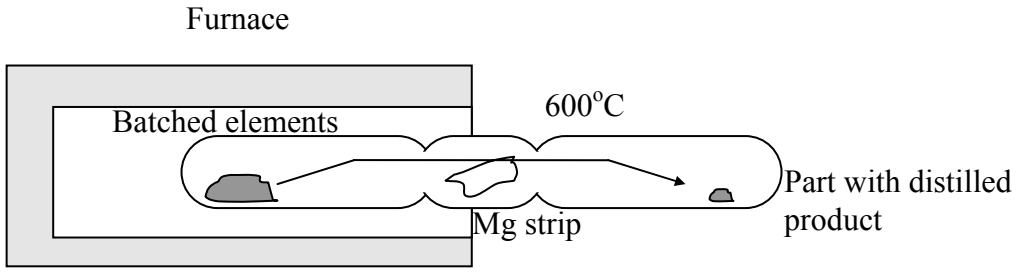

Figure 2-10 Distillation process of pure As_2S_3

After distillation process was done, residue was left at the original side. The part of the quartz tube with distilled product was sealed off and underwent melting process, as described in Figure 2-7.

2.9. Effect of distillation

Comparison of IR spectra of As_2S_3 prepared from unpurified, purified (sublimated As + purified S) and distilled raw materials was shown in Figure 2-11.

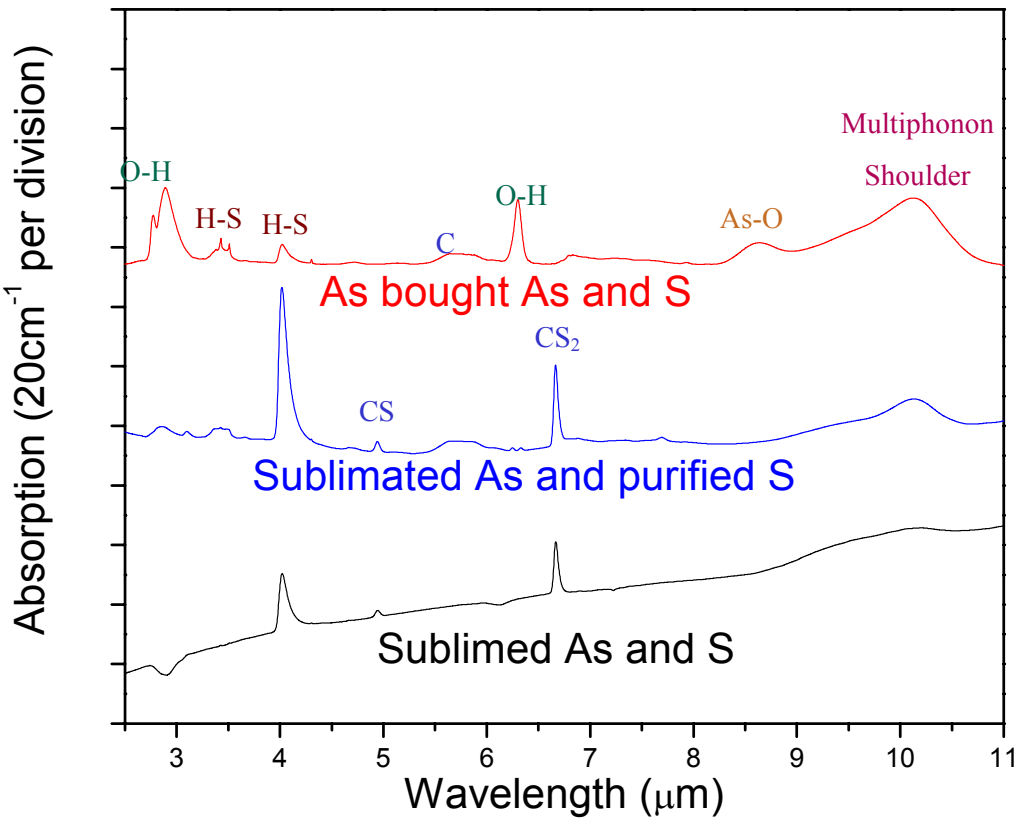

Figure 2-11 Effect of sublimation on purity of As_2S_3

After further purification using the distillation method, the amount of C impurities (5.78 μm, 6.66 μm) inside the sample was reduced but there remains some H_2S at 4 μm. We should be able to further improve the quality of glass but we discontinued the perform fabrication works as we had found a new supplier of As_2S_3 few mode fiber.

3. Optical experiment set-up

3.1. Preface

As discussed in Section 1.9, interferometric or phase mask techniques were suggested as methods to write the FBGs at the beginning of the project and we started with interferometer method, for which the details will be discussed in Section 4.

In the later stage of our research, it is thought that the phase mask technology became more sophisticated and we attempted to use this easier technique. Section 5 will cover the details of experiment and results obtained using phase mask technique.

In this Section, we will describe our instrument for experiment and the characteristic of As_2S_3 optical fiber we used.

3.2. Interferometric (Holographic) method

Few years ago, Asobe et al. successfully fabricated FBGs in chalcogenide glass fiber using the transverse holographic method[12], which is the interference of two laser beams. Since it was first proposed to use interferometric techniques in writing FBGs in this project, we tried to follow their basic set-up. A 35 mW He-Ne laser was employed to inscribe Bragg gratings at 633 nm which is near the band gap of As_2S_3. An OSA (Agilent HP86412B) is used to analyze the inscribed FBG with the reflectivity measured at 1.55 μm.

The optical set-up presented in Figure 3-1 is divided in three parts, which are:

1. Interferometer, which produces the interference
2. Coupling system, which couples the light into the optical fiber
3. Analyzer, which detects and measures the FBGs

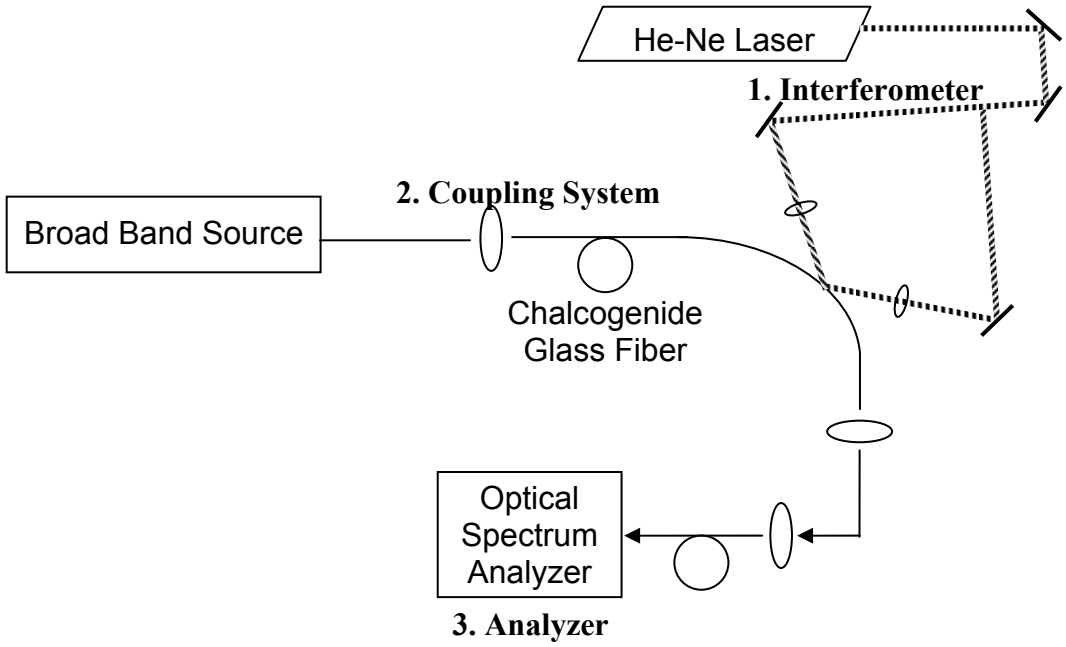

Figure 3-1 Optical set-up of the interferometric method

3.2.1. Interferometer

First suggested by Meltz et al[72], inscription of the FBGs in silica fiber using UV laser light can be done by the set-up as shown in Figure 3-2. A beam splitter is used to divide a single input laser beam into two beams of the same power. The beams then interfere at the fiber core after being reflected by mirrors.

To assemble a similar set-up, a glass cube with an anti-reflection coating is used as the beam splitter. This cube is made of two prisms joined together providing a 50:50 split ratio. The two arms of the interferometer of the same length are collimated into the fiber using first two mirrors mounted on a stable high precision rotation stage (5 arc min resolution) and two hemi-cylindrical lenses. The interference zone is about 1 cm in length and 100 μm in width considering an original beam of 1.2 mm in diameter. The total losses are expected to be less than 1% at each interface.

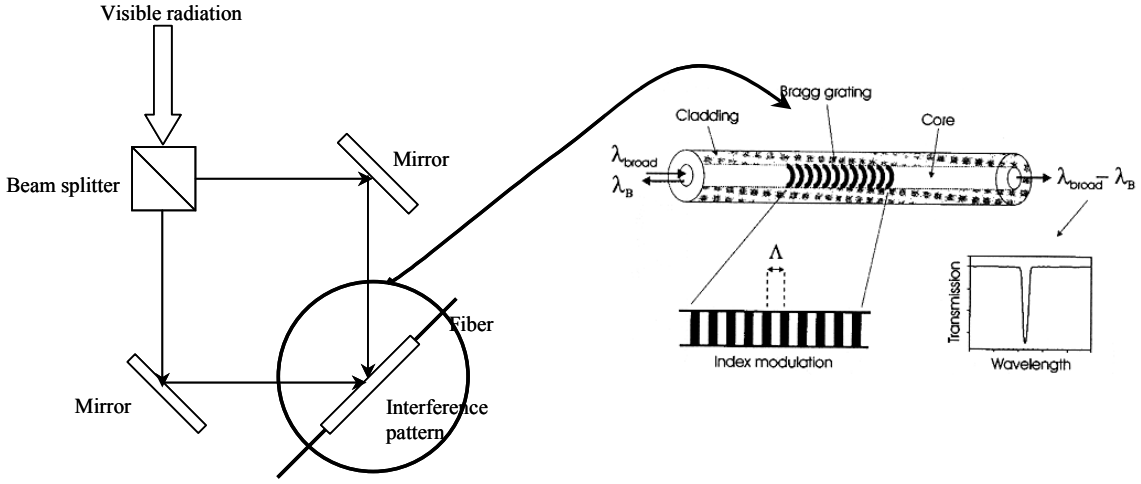

Figure 3-2 Components of interferometer[70]

Since As_2S_3 glass fiber is being used, a He-Ne laser of 7 mW output was used at the beginning. Due to the lack of power, a new laser of 35 mW output was purchased and used for the FBGs writing experiment.

3.2.2. Coupling system

Multimode optical fibers are typically of hundreds of microns in diameter but single-mode fibers have core diameter of only a few microns. Because of the requirement of accuracy, highly precise XYZ flexure stages with sensitivity down to 0.2 μm were used in the fiber coupling systems to insert a laser probe into the fiber and detect and measure the inscription of the FBGs. A microscope was used to ensure the perfect centering of the all set-up when moving such small parts during alignment.

The interferometer described above has several beams paths in open air. Since the interference fringes formed at the fiber can drift if the paths of the two beams change during the inscription time, it is important that these are shielded from turbulence. For this reason, the interferometer is built on a sturdy base, with stable optical mounts and enclosed entirely within Plexiglas housing. This housing gives an extra protection and avoids eventual dangerous reflection when conducting experiment.

3.2.3. Analyzer

To detect the inscribed FBGs, a broadband light source and an optical spectrum analyzer were purchased. We used Agilent OSA 86142B for fast, precise measurements in the 600 nm to 1700 nm range and Agilent Broadband light source 83437A which is centered at 1550 nm and has a 100 nm bandwidth. Because of the relatively short length of As_2S_3 fiber, SMF-28™ SiO_2 fibers were used to connect the As_2S_3 fiber to the light source and OSA.

3.3. Phase mask technique

In FBGs writing experiment using phase mask technique, we used same laser source, coupling system and analyzer. The only difference between phase mask technique and interferometric method would be a single mask is used to replace most of the optics used in the interferometric method. When using +1/-1 order phase mask, the incident laser beam needed to be normal to the phase mask and the fiber. For 0/-1 order phase mask, the phase mask is tilted at an angle that satisfy the Bragg's law and the fiber should be placed parallel

to the phase mask. In our case, Bragg's angle equals 76.6°. Figure 3-3 shows the illustrated diagram for phase mask experiment set-up.

Meanwhile, the two phase mask should have different pitch period.

For +1/-1 order phase mask, $\Lambda_{PM} = 2\Lambda_{fringe}$

For 0/-1 order phase mask, $\Lambda_{PM}=\Lambda_{fringe}$

where Λ_{fringe} is the period of Bragg gratings and Λ_{PM} is the period of the phase mask.

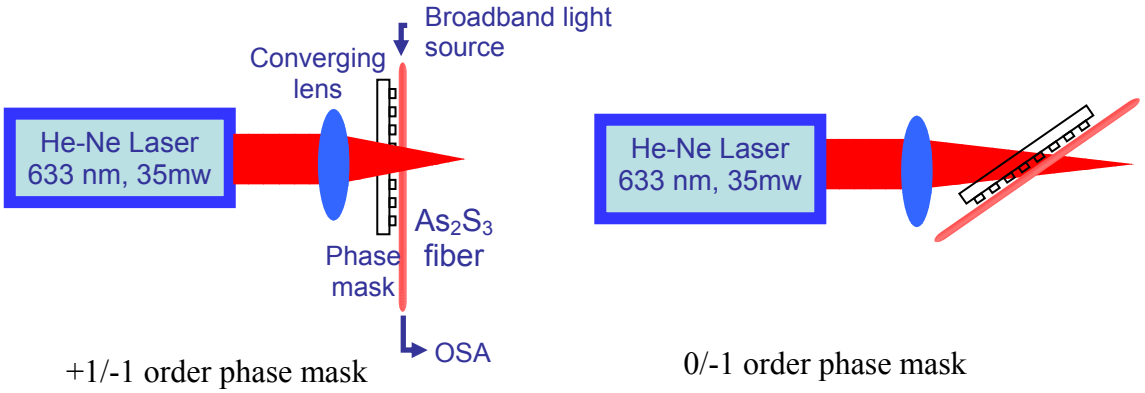

Figure 3-3 Illustrated diagram for phase mask experiment set-up

3.4. Transmission spectra of single mode SiO_2 and As_2S_3 fiber

The commercial few mode (Number of mode =79) As_2S_3 fibers were used for the FBG writing experiment. The specifications of these fibers are reported in Table 3-1:

Table 3-1 Specifications of single-mode chalcogenide fibers

Core/Cladding materials	As_2S_3 / As-S
Working wavelength	1 to 6 μm
Core diameter	20 μm
Cladding diameter	250 μm
Numerical aperture	0.3
Core refractive index	2.4

Before performing the FBGs writing experiment, the transmission spectra of Si_2O and As_2S_3 fiber were taken and compared.

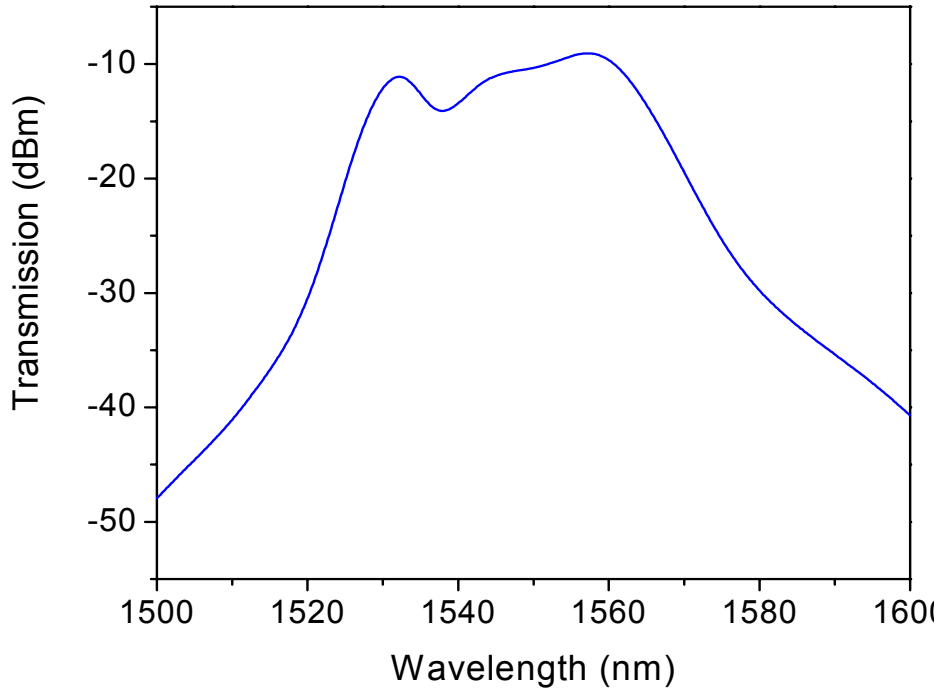

Figure 3-4 Transmission spectrum of SiO_2 fiber, SMF-28™

Figure 3-4 showed the transmission spectra of a single mode SMF-28 SiO_2 fiber. Because of the much more sophisticated development of SiO_2 fiber, SMF-28 showed a much higher transmittance than As_2S_3 fiber. The maximum attenuation SiO_2 fiber is less than 0.40 dB/km. The transmitted profile resembled the characteristic output spectrum of the light source as printed in the manufacturer' s manual as shown in Figure 3-5.

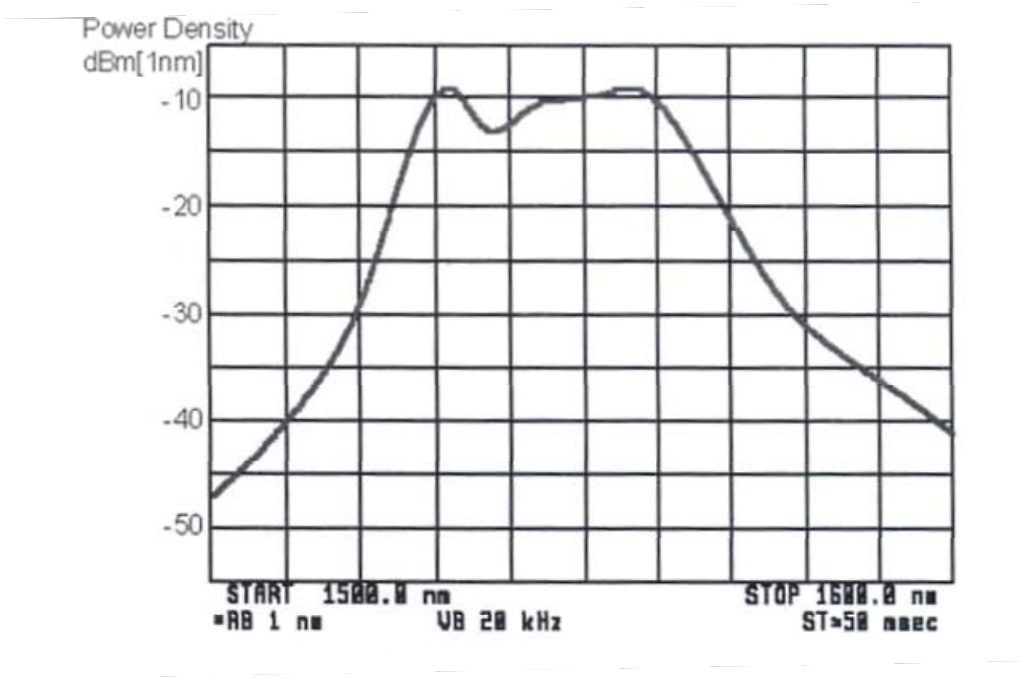

Figure 3-5 Characteristic output spectrum (1500 nm to 1600 nm) of the light source

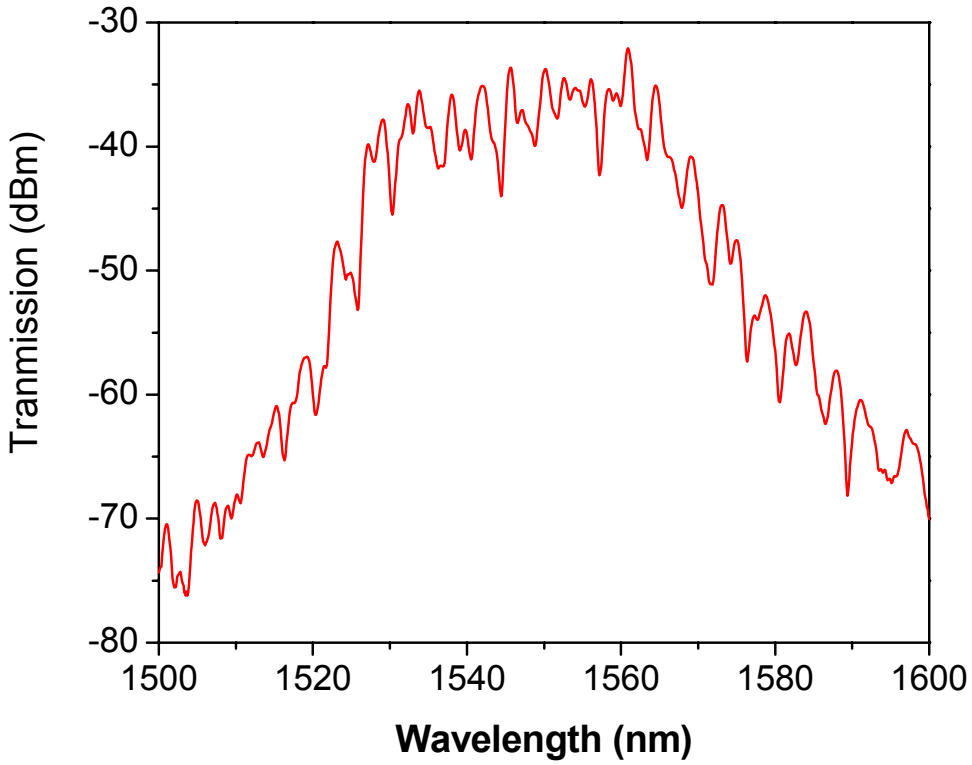

Figure 3-6 Transmission spectra of one of the As_2S_3 fibers from A.R.T Photonics

For As_2S_3 fiber, the transmission loss is ~1300 db/km at 1500 nm. As a result, the maximum intensity in the transmission spectrum (as shown in Figure 3-6) reduced to -32.4 dBm. The application range of As_2S_3 fiber is usually between 1.5 μm to 12 μm while the light source and optical spectrum analyzer we had should be applied at wavelength around 1.5 μm, explained why we have a low transmission.

In fact, the maximum intensity of different As_2S_3 fibers from the same supplier varied from -28 dBm to -38 dBm. This may be explained by the quality of the polish ends of each fiber.

Also, there were numerous spikes present in the data. When the shape of the fiber changed slightly, the pattern of the transmitted spectrum also changed. It is possibly due to the presence of multi modes rather single mode. The occurrence of mode beating suggested that the fiber has the multimode properties in our operation range. To determine mathematically how many modes, *N*, can existed, we should consider the V parameter of the fiber.

$$V = \frac{\pi d}{\lambda}\sqrt{n_1^{\,2} - n_2^{\,2}} \qquad 3\text{-}1$$

where d is the diameter of the fiber core, which is 20 μm,

λ is the transmitted wavelength which equals 1.55 μm,

and numerical aperture of the fiber is given to be 0.3 by the manufacturer of the fiber.

$$N.A. = \sqrt{n_1^{\,2} - n_2^{\,2}} \qquad 3\text{-}2$$

Therefore, V equals 12.16.

$$N = \frac{V^2}{2} \qquad 3\text{-}3$$

The number of modes presented inside the fiber is calculated to be 73. With this number of modes, it explained the phenomenon of mode beating in the transmission spectrum as it is commonly seen in multimode fiber.

For FBGs writing experiment using single mode fiber, one sharp peak would be expected. For multimode fiber, the result should be different due to the different mode coupled to the FBGs written.

3.5. FBGs in SiO_2 single mode fiber

A commercial FBGs SiO_2 filter from JDS Uniphase was characterized for our initial test and reference. The experimental results shown in Figure 3-7 are identical of the description document of the filter in which states the FBGs located at 1537.2 nm and 1563.7 nm.

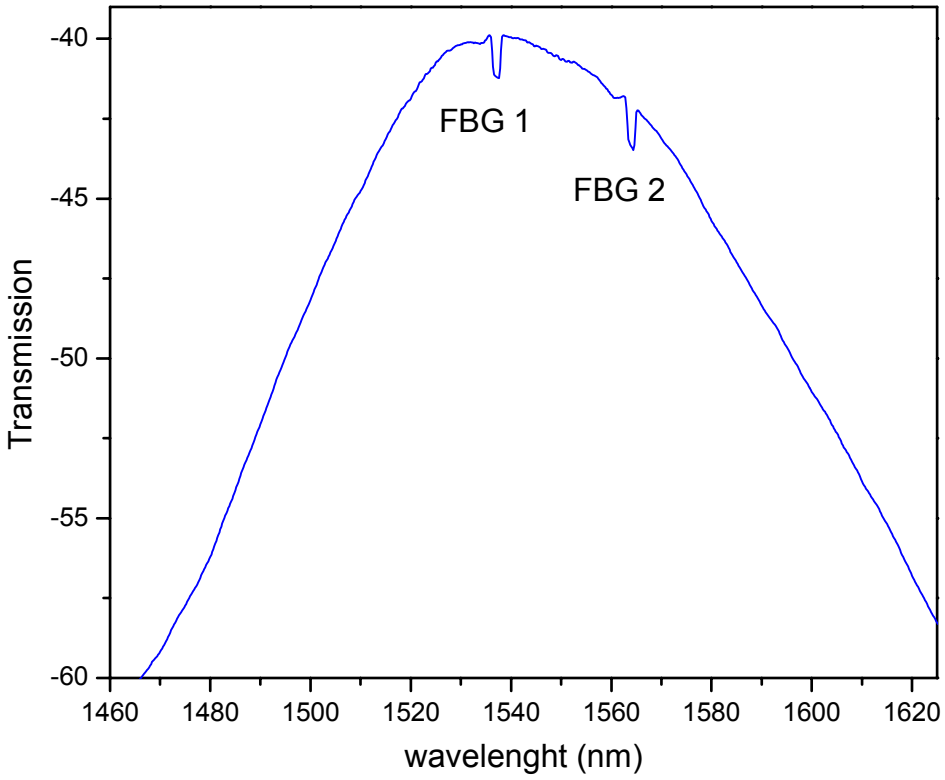

Figure 3-7 SiO_2 fiber Bragg gratings filter

4. Interferometric method

4.1. Preface

As described in Section 1.9, there are different techniques for inscription of Bragg gratings in silica optical fibers, such as internal inscription[71], interferometric techniques[72], phase-mask techniques[73], point by point fabrication[74], etc.

Among all these fabrication methods, we first tried interferometric method because of its flexible set-up. Only slight adjustment in optics can change the wavelength of FBGs. However, it requires high stability and alignment to write the FBGs. In this section, the problems we encountered at the beginning of our research will be discussed. After solving all the problems, we were able to write FBGs in As_2S_3 fiber.

4.2. Introduction of interferometric method

In this technique shown in Figure 4-1, an interferometer splits the incoming laser light into two beams and two placed mirrors then recombine them in order to form an interference pattern at the point of recombination.

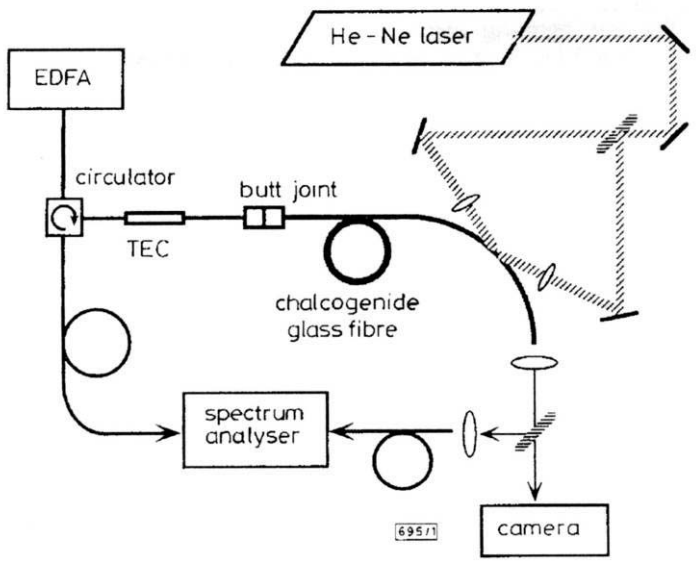

Figure 4-1 Experimental setup for As_2S_3-based fiber grating fabrication [64]

The period of the grating[10] is given by:

$$\Lambda = \frac{\lambda_w}{2\sin\varphi} \qquad 4\text{-}1$$

where λ_w is the wavelength of incident beam and φ is the half-angle between the intersecting split beams. Hence, a Bragg grating resonance wavelength can be represented in terms of the wavelength of writing irradiation and half-angle[10]:

$$\Lambda_B = \frac{n\lambda_w}{\sin\varphi} \qquad 4\text{-}2$$

The most important advantage offered by the amplitude-splitting interferometric fabrication technique is the ability to inscribe Bragg gratings at any wavelength by simply

changing φ. It allows the fabrication of wavelength narrowed or broadened gratings, offering high flexibility. By using curved reflecting surfaces in the beam delivery path, different grating geometries can be accomplished.

There are some disadvantages; however, chief among them is that it is sensitive to mechanical vibration. Submicron displacements in the position of mirrors, beam splitter, or mounts in the interferometer can cause the fringe pattern to drift, washing out the grating. Due to long separate optical path lengths involved in the interferometers, air currents, which affect the refractive index locally, may also cause a problem in the formation of a stable fringe pattern. Finally, the laser source must have good spatial and temporal coherence and excellent output power stability in order to obtain quality gratings.

4.2.1. Laser power requirement of FBGs writing

Asobe et al.[64] reported fiber Bragg gratings written in single mode (6 μm/120 μm) fiber. We can consider it as a reference of how much laser power density is needed to trigger the reaction.

In his experiment, Asobe used 50 mW HeNe laser to form a 40 μm x 10 mm size spot. Also, the fiber cladding is 60 μm in diameter. Given that the absorption coefficient of the fiber is 30 cm^{-1}. Thus, the power density should be 104.4 mW/mm when the beam reached the fiber core. In order to obtain enough power for FBGs writing, the same power density should be achieved.

In our experimental set-up, we used a 35 mW HeNe laser and fiber with cladding in thickness 115 μm. Additionally, half of the light is being reflected by the phase mask. The beam size required should be 0.593 mm x 0.127 mm. To obtain the desired beam size, a planar convex lens with focal length 200 mm was used and the phase mask was placed 17.9 mm away from the lens.

4.2.2. Difficulties encountered during the experiment

In our experiment, there are certain limitations which made it more difficult to obtain the FBGs in As_2S_3 fiber rather than SiO_2 fiber using the interferometric method. These reasons are listed as followed:

Refractive index and irradiation angle

Refractive index of silica fiber is known to be around 1.45 while As_2S_3 has a much higher value, 2.4.

Bragg grating resulted from interferometric method will have wavelength:

$$\lambda_B = \frac{n\lambda_{HeNe}}{\sin\left(\frac{\theta}{2}\right)} \qquad 4\text{-}3$$

Consider wavelength of HeNe laser, λ_{HeNe}, is 633 nm which is a fixed value and refractive index, *n*, is also fixed at 2.4. Thus, $\sin\left(\frac{\theta}{2}\right)$ is inversely correlated to λ_B. Limited by the light source which provides illumination range, λ_B needs to be in the range of 1520 to 1580nm for reasonable transmission intensity. Together with the fact that $\sin\left(\frac{\theta}{2}\right) \le 1$, θ has to be 152^o to 160^o. For SiO_2 fiber with refractive index at 1.5, FBG irradiated at 248nm UV laser and the angle will be in the range of 27.2 ^{o} to 28.3 ^{o}. The angle needed to write the FBGs for As_2S_3 glass fiber is much higher and it is difficult to set up.

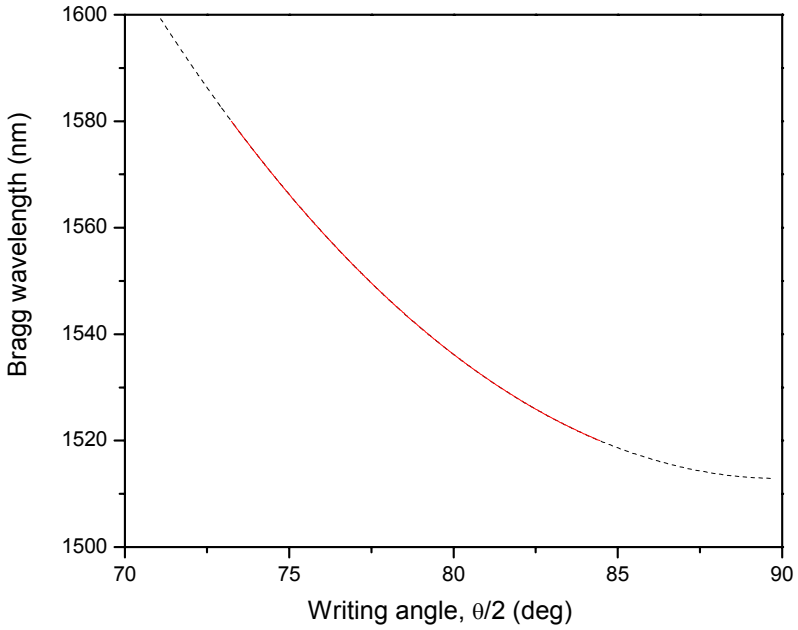

Figure 4-2 Calculation of Bragg wavelength resulted from changing the writing angle

Coherence length of the laser

Besides the irradiation angle, the coherence of the two beams during intereference is also very critical. For HeNe laser, the coherence length is 21.4 cm, i.e., the total optical path for the laser beam within the interferometer has be to less than the coherence length in order to achieve interference. Combining the wide irradiation angle, putting the optics with actual physical dimension within a short coherence length of the laser is practical difficult.

Vibration

It took a significant time period in setting up and modifying the inteferometric set-up to achieve the desire angle irradiation within the coherence length. However, we had not succeeded in writing FBGs. We had reconsidered the set-up and it is thought that vibration may be the cause of the poor results obtained even though the experiments were carried out on a rigid optical table. After the vibration issue was solved by turning off all the operating instruments at the surrounding, FBGs were obtained.

To prove that vibration impacted our experiment, a tri-axial PCB Piezotronics shear accelerometer model #356A15 was used. A PCB Piezotronics ICP Sensor Signal Conditioner, Model 485A22 sent the signal to the B&K Pulse Data Acquisition Unit type: 3560C.

An accelerometer is a device that measures the vibration, or acceleration of motion of a structure. The force caused by vibration or a change in motion (acceleration) causes the mass to "squeeze" the piezoelectric material which produces an electrical charge that is proportional to the force exerted upon it. Since the charge is proportional to the force, and the mass is a constant, then the charge is also proportional to the acceleration.

The accelerometer was placed in the experiment set-up with all equipment turned onto determine whether vibration is a concern during the experiment. To provide stability, epoxy was used to mount the base of accelerometer to the optical table and the accelerometer was then screwed on the base.

Figure 4-3 illustrated the position of the accelerometer mounted on the optical table by epoxy. The X-axis runs parallel to the laser beam and the Y-axis runs perpendicular to the beam direction. The Z-axis runs perpendicular to the optical table.

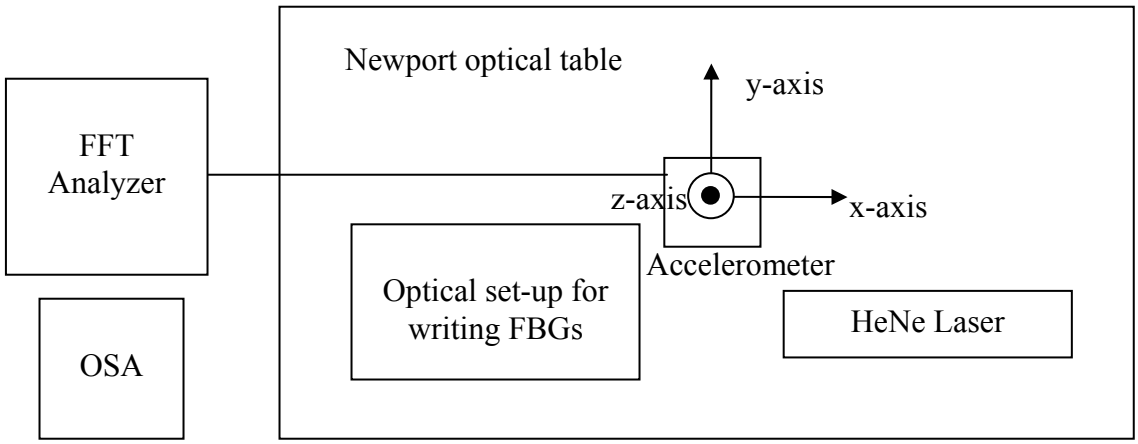

Figure 4-3 Set-up of the accelerometer on the Newport optical table

Figure 4-4 shows the Fast Fourier Transform (FFT) acceleration versus frequency measured in the three axes of the Newport optical table. The accelerometer measured acceleration in x, y and z-direction respectively. Spikes with asterisk at 255, 511, 771 Hz arise from electronic noise which generated by the amplifying circuit.

The results indicated the presence of vibration noises in significant amplitudes and different frequency in the lab. Spikes appeared at different frequency were caused by various vibration sources in the surrounding which the optical table is unable to damp these vibration. Besides the magnitude of these peaks, lower frequency means vibration with higher energy, which should be the most concern.

For any set-up using interferometric technique, precision and stability are critical factors to get succeed. Unfortunately, the optical table we had been using was unable to provide the stability we needed and this is thought to be the reason for us not being able to write good FBGs previously.

After the vibration problem was identified, we have turned off all other equipments in the laboratory and retested the vibration status of the optical table. Figure 4-5 shows the Fast Fourier Transform (FFT) acceleration versus frequency measured after turning off the equipments.

We found that the vibrations in x-axis and y axis have been significantly reduced. Meanwhile, there still existed 2 spikes at 24.9 Hz and 117.5 Hz, which may arise from the building vibration and other sources.

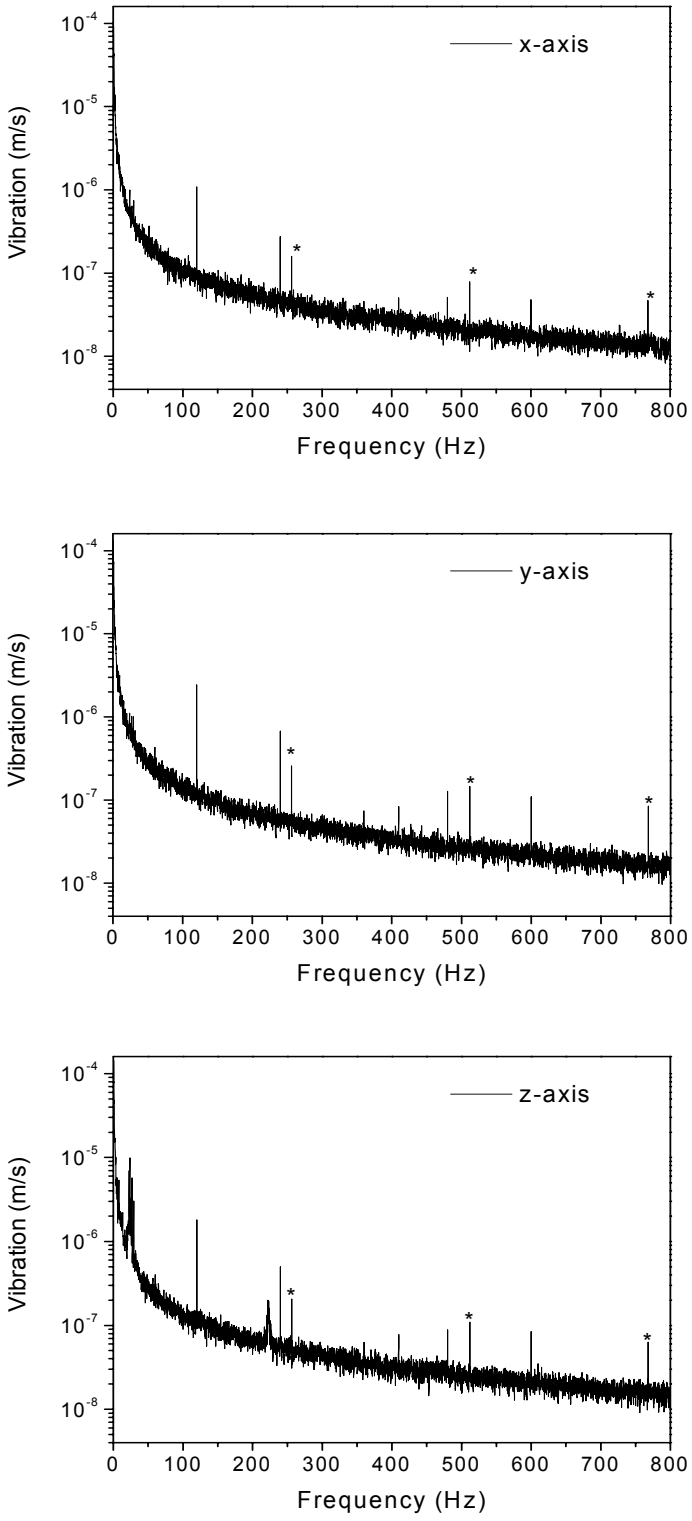

Figure 4-4 FFT acceleration versus frequency measured under normal testing condition

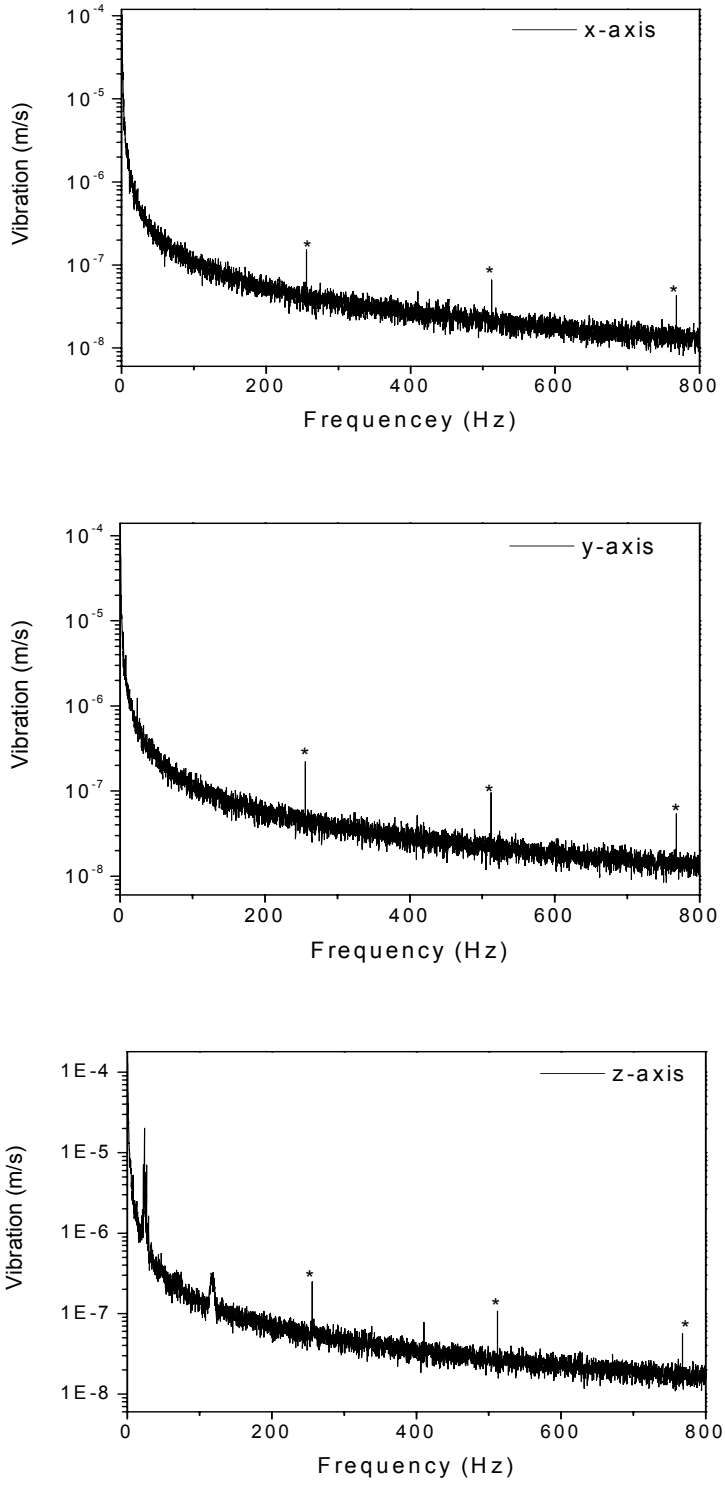

Figure 4-5 FFT acceleration versus frequency measured after equipments around have been turned off

4.3. Results of FBGs writing

After the vibration problem was eased, we were able to obtain FBGs using the interferometric method at $\theta = 152^{o}$. The transmission spectra taken at before and after the experiment are shown in Figure 4-6 and Figure 4-7 respectively.

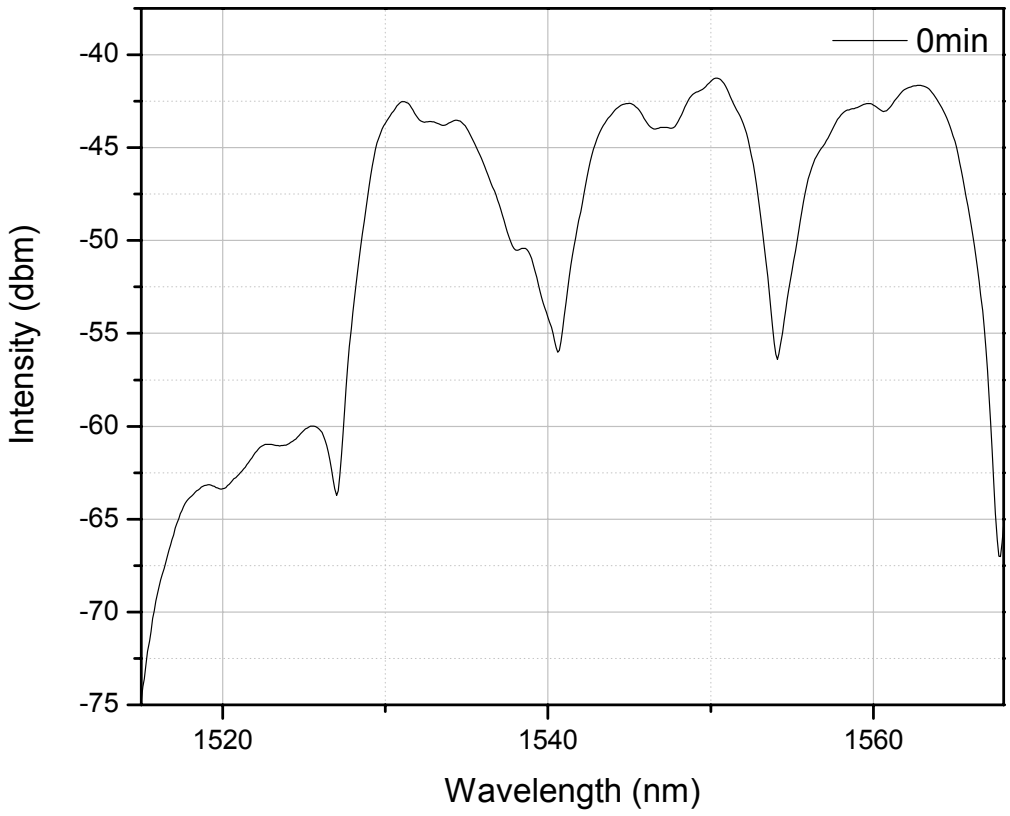

Figure 4-6 Transmission spectrum of As_2S_3 fiber before FBGs writing experiment using interferometric method (0 min. of exposure)

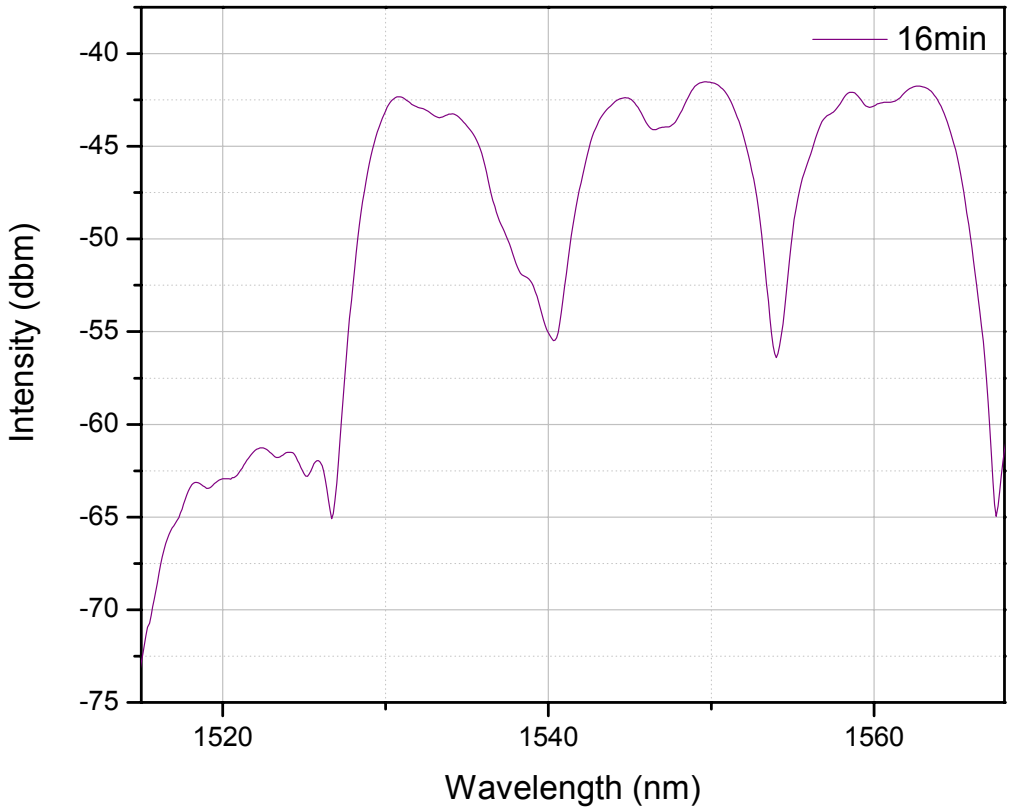

Figure 4-7 Transmission spectrum of As_2S_3 fiber after FBGs writing experiment using interferometric method (16 min. of exposure)

It is difficult to observe the growth of FBGs using comparing the transmission spectra because of the presence of mode beating. Therefore, the transmission intensity at different time of laser exposure was normalized to show the FBGs written in Figure 4-8. The growth process is plotted in Figure 4-9.

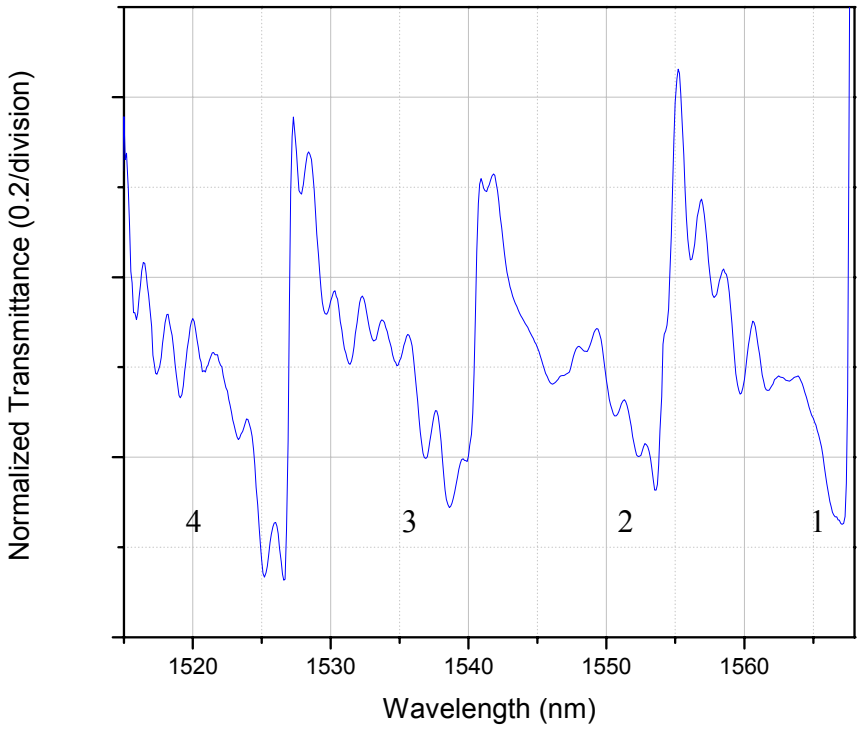

Figure 4-8 FBGs in few mode As_2S_3 fiber using interometric method

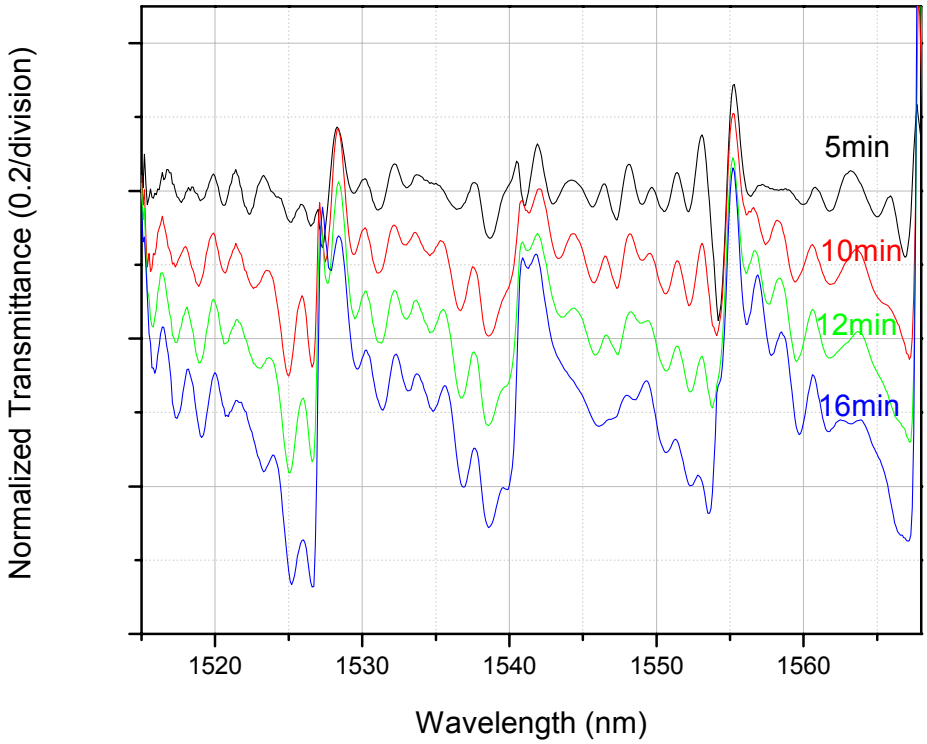

Figure 4-9 Growth of FBGs in few mode As_2S_3 fiber using interometric method

We obtained a series of transmission dips rather than one single transmission dip, which agreed with other researchers' work on multimode FBGs[65, 75]. In our case, four transmission dips appear at wavelengths 1526.6 nm, 1538.6 nm, 1553.7 nm and 1566.3 nm. Since we have a writing angle = 152°, Mode 1 should be at 1566.3 nm (with a slight misalignment of 0.4°, calculated writing angle = 151.67 ° corresponded to 1566.3 nm).

Distance between each set of transmission dips is measured to be around 13.2 nm. Suggested by Mizunami et al[75], this periodicity indicates the reflection from the N mode to the N+1 mode and that from the N+1 mode to N mode.

Bragg reflection condition or the phase matching condition, of an index modulation with the period L is given by

$$\beta_1 - \beta_2 = \frac{2\pi}{\Lambda} \qquad 4\text{-}4$$

where β_1 and β_2 are the propagation constants of forward and backward propagating modes, respectively. $\beta_1 = -\beta_2 = \beta$ if the same mode reflects.

For step-index multimode fiber, the relation between the normalized propagation constant b for the Nth principal mode for normalized frequency V is givien by[76]:

$$V = \sqrt{\frac{1}{1-b}}\left(\frac{N}{2}\pi + \frac{\pi}{4} + \tan^{-1}\sqrt{\frac{b}{1-b}}\right) \qquad 4\text{-}5$$

and

$$V = \frac{2\pi a \cdot NA}{\lambda} \qquad 4\text{-}6$$

In this case, a is the core radius, NA is the numerial aperture and λ is the wavelength. Since V can be calculated by substituting different λ, b can be found putting N = 0, 1, 2……

Then, we can calculate the propagation constant by the following equation:

$$\beta = \frac{2\pi}{\lambda} n_1 \left\{ \left[1 - (1-\Delta)^2 \right] b + (1-\Delta)^2 \right\} \qquad 4\text{-}7$$

where Δ is the maximum relative index difference.

Figure 4-10 shows the plot of propagation constant versus wavelength in N equals 0 to 10. We tried to match the transmission dips to the mode diagram to see if any of the peaks came from the coupling of the same mode.

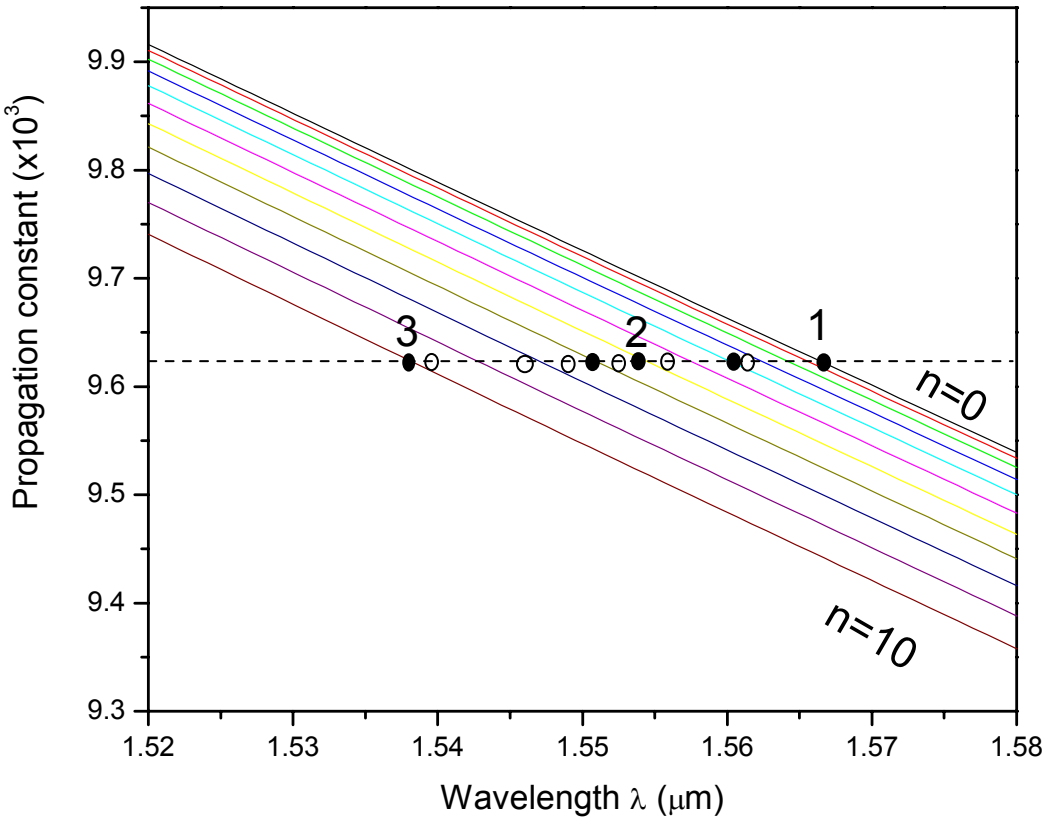

Figure 4-10 Mode diagram of FBGs

The black dot shown in Figure 4-10 indicated a match of transmission dip wavelength to the reflection of the same mode. We found that some of the dips match to the line very well, especially the major dips at 1538 nm, 1554 nm and 1567 nm. Additionally, dips at 1551 nm and 1558 nm appeared also due to the same mode reflection.

On the other hand, the white dots lied between different modes should be arisen from the coupling of the neighboring modes.

The maximum reflectivity is found to be 46.6% at 1526.6 nm. The relationship between reflectivity and laser irradiation time is plotted in Figure 4-11. It showed that the reflectivity increase with time. However, it seemed the time for exposure is not long enough to show the saturation.

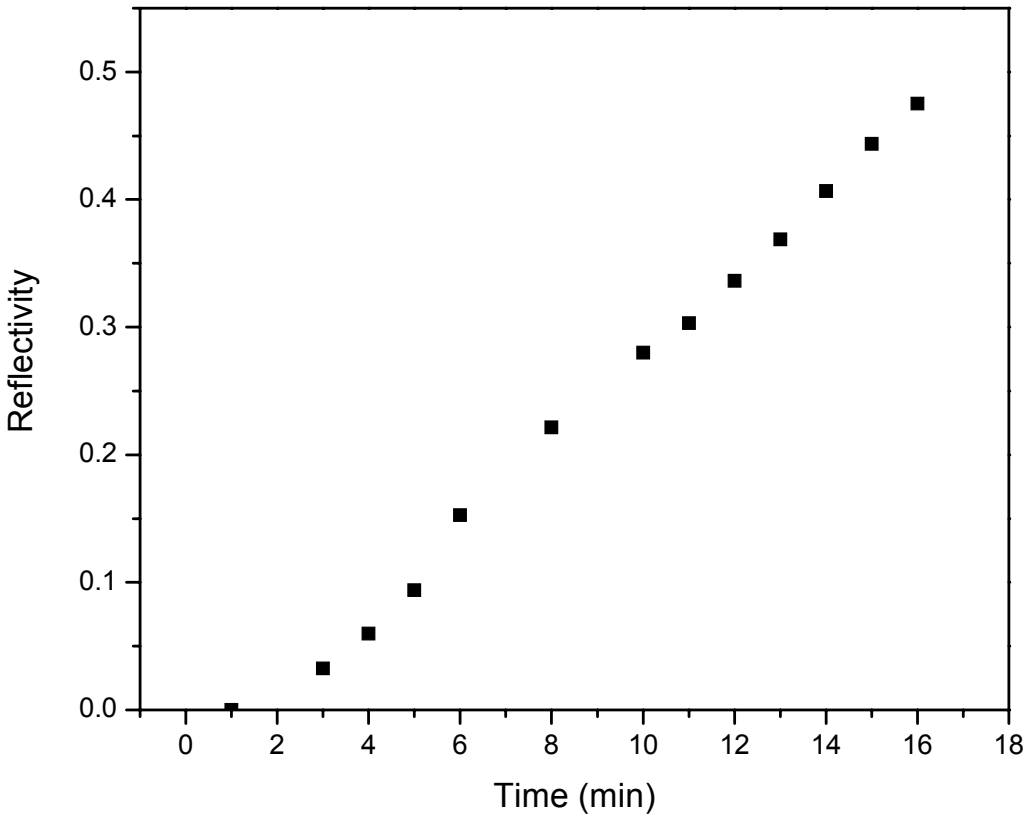

Figure 4-11 Reflectivity of FBGs in As_2S_3 fiber

As irradiation time increased, the wavelength of transmission dips shift to the longer wavelength because of the refractive index change of the materials. From this shift, we can estimate the effective refractive index change using the gratings equation

$$2n_{eff}\Lambda_{FBG} = \lambda_B \qquad 4\text{-}8$$

by assuming initial n equals 2.4, we estimated Λ_{FBG} to be 326.44 nm.

Using the below data, we can estimate the effective index change.

Table 4-1 Calculation of effective index of refraction

Initial wavelength (nm)	1524.74	1526.37	1550.67
Final wavelength (nm)	1525.19	1526.58	1550.86
$\Delta\lambda$(nm)	0.45	0.21	0.19
Δn_{eff}	0.000690	0.000322	0.000291

Table 4-1 is the value we used in the calculation. The average effective index change is estimated to be 0.000434.

5. Phase mask method

5.1. Preface

We attempted to use the holographic method which involves many components that slight misalignment and is difficult to achieve quality FBGs. Therefore, effort had also been made to reexamine the feasibility of applying phase mask technique. At a later stage of our research, we attempted to fabricate phase mask using E-beam lithography under collaboration with Ohio State University. This work ended before we were able to produce phase mask with excellent grating profile which is essential for desired diffraction pattern because we finally found suppliers that makes suitable phase masks using the holographic method. Among the two phase masks purchased from different suppliers, only the tailor made phase mask could work for our FBGs writing experiment.

During the years we have worked on the project, the phase mask fabrication technology became more sophisticated and we started reconsidering this simpler FBGs fabrication technique, in which a transmission phase-grating, also known as the phase mask, is used as the component of the interferometer.

Application of a phase mask is a very common technique when using SiO_2 fiber for the fiber gratings inscription because of the simplicity of the FBG writing setup. However, due to our experimental condition, in which HeNe laser and As_2S_3 fiber were used, the period of the phase mask has to be in the range of ~ 640 nm. As a reference, ~1070 nm phase masks are commonly used for SiO_2 FBGs inscription. We first collaborated with Ohio State University to fabricate our own phase masks and later purchased phase masks from commercial suppliers.

As we mentioned before, we needed to turn off all other machines inside the lab in order to be able to perform FBGs writing experiment to assure the stability of the optical set-up. This is a feasible way to work but it also caused inconvenience while other researches was carried out in the same location. Therefore, we started our phase mask experiment at a new area, using another optical table. Vibration measurement was performed again to assure the vibration level.

5.2. Vibration measurement

We changed our optical table and our location for experiment. The new optical table we used is Kinetic Systems Model No: 505-200-22-3. Again, the vibration test has been done to assure we have a good stable optical table. Figure 5-1 shows the Fast Fourier Transform (FFT) acceleration versus frequency measured in the three axes of the Kinetic Systems optical table. The accelerometer measured acceleration in x, y and z-direction respectively. Spikes with asterisk at 255, 511, 771 Hz arise from electronic noise which generated by the amplifying circuit.

In Figure 5-1, we can see a spike at 28.3 Hz in x-axis and low amplitude vibration at around 42-59 Hz. In z-axis, we found a very low amplitude spike at 59.4 Hz. Overall, the vibration level is lower than that in the original lab space.

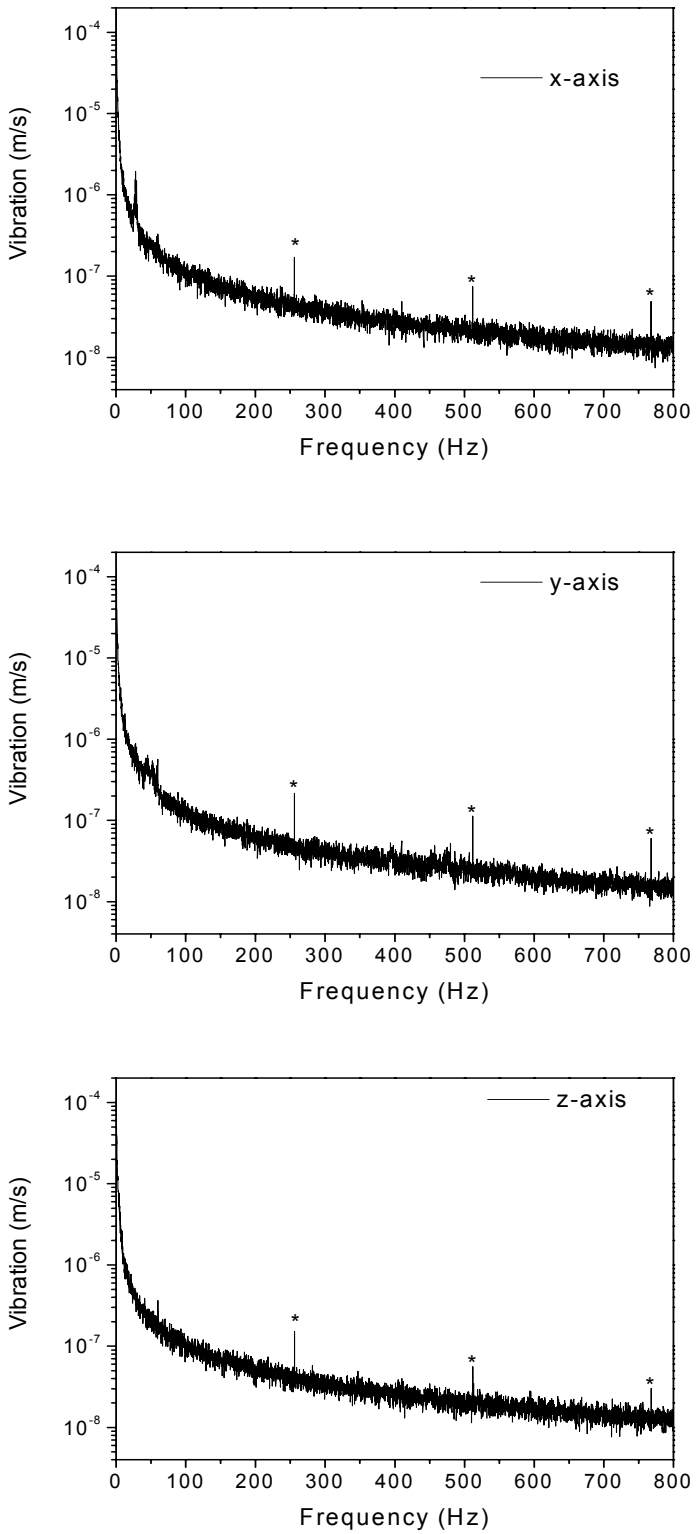

Figure 5-1 Vibration measurement of second optical table in new experiment location

5.3. +1/-1 order phase mask

Phase masks can be used because of the diffraction of an incident light beam into several orders, $m = 0, \pm1, \pm2\ldots$ Figure 5-2 shows the diffraction of an incident beam from a phase mask with λ_{pm} period. The relationship between the period of the phase mask and the period of the FBGs can be realized by considering the diffraction and interference theory.

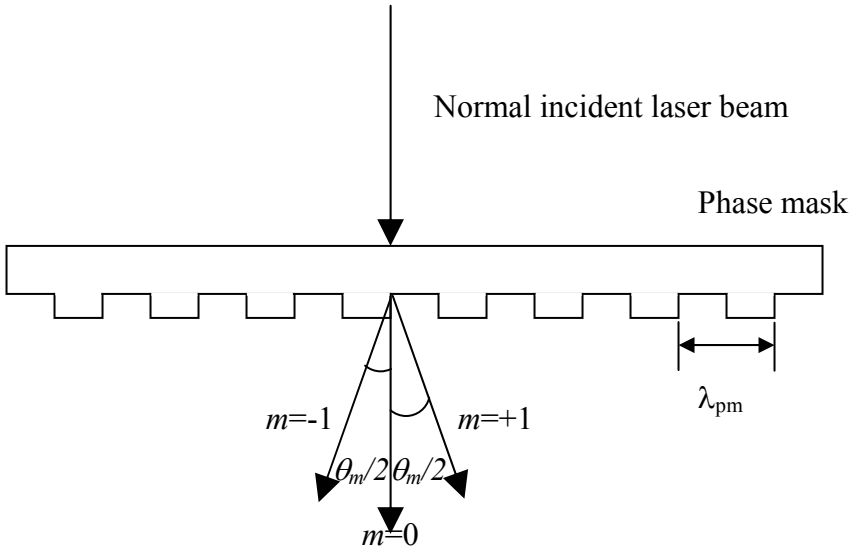

Figure 5-2 A illustrated diagram of an incident beam diffracted from a phase mask

The incident and diffracted order satisfy the general diffraction equation[77].

$$\lambda_{pm} \sin\left(\frac{\theta_m}{2}\right) = m\lambda_{HeNe} \qquad 5\text{-}1$$

where λ_{pm} is the period of the phase mask grating,

λ_{HeNe} is the wavelength of HeNe laser,

$\theta_m/2$ is the direction where mth maxima can be found.

+1/-1 st order phase mask is used to produce interference for FBGs fabrication. The angle of first-order diffracted beam is

$$\theta_1 = 2\sin^{-1}\left(\frac{\lambda_{HeNe}}{\lambda_{pm}}\right) \qquad 5\text{-}2$$

Now, let's consider there are two planar waves[78], whose amplitudes are described by the equations:

$$\vec{E}_1\left(\vec{r}_1,t\right)=\vec{E}_{01}\cos\left(\vec{k}_1\cdot\vec{r}-\omega t\right) \tag{5-3}$$

$$\vec{E}_2\left(\vec{r}_1,t\right)=\vec{E}_{02}\cos\left(\vec{k}_2\cdot\vec{r}-\omega t\right) \tag{5-4}$$

where k_1 and k_2 are the propagation vectors of the two waves.

On the other hand, the relative irradiance within the same medium is

$$I=\left\langle \vec{E}^{\,2}\right\rangle_T=\left\langle \vec{E}\cdot\vec{E}\right\rangle_T \tag{5-5}$$

which is also known as the time average of the magnitude of the electric-field intensity squared.

In the case of total maximum irradiance, two waves are in-phase and δ is an integer multiple of 2π.

$$I_{\max}=I_1+I_2+2\sqrt{I_1I_2} \tag{5-6}$$

$$I_1=\frac{E_{01}^2}{2}\ \text{and}\ I_2=\frac{E_{02}^2}{2}$$

$$I_{12}=2\left\langle \vec{E}_1\cdot\vec{E}_2\right\rangle_T$$

$$I_{12}=2\,\vec{E}_{01}\cos\left(\vec{k}_1\cdot\vec{r}-\omega t\right)\cdot\vec{E}_{02}\cos\left(\vec{k}_2\cdot\vec{r}-\omega t\right)$$

$$=\vec{E}_{01}\cdot\vec{E}_{02}\cos\left[\left(\vec{k}_1\cdot\vec{r}-\omega t\right)-\left(\vec{k}_2\cdot\vec{r}-\omega t\right)\right]$$

$$=\vec{E}_{01}\cdot\vec{E}_{02}\cos\left[\left(\vec{k}_1-\vec{k}_2\right)\cdot\vec{r}\right]$$

To achieve maximum,

$$\cos\left[\left(\vec{k}_1-\vec{k}_2\right)\cdot\vec{r}\right]=2m\pi \qquad \text{where } m \text{ is an integer} \tag{5-7}$$

For +1/-1st order phase mask, $k_1 = (-k_x, k_y)$ and $k_2 = (k_x, k_y)$. Then, the condition for maximum intensity reduces to

$$2k_x\vec{r}=2m\pi \tag{5-8}$$

and the fringes are seen to be a set of vertical lines passing through the x-axis at $m\pi/k_x$. The spacing between the fringes of the FBG, λ_g is therefore

$$\lambda_g=\frac{\pi}{k_x}=\frac{\pi}{k\sin\left(\frac{\theta_1}{2}\right)}=\frac{\pi}{\left(\frac{2\pi}{\lambda_{HeNe}}\right)\sin\left(\frac{\theta_1}{2}\right)}$$

$$=\frac{\lambda_{HeNe}}{2\sin\left(\frac{\theta_1}{2}\right)} \tag{5-9}$$

Now substitute Equation 5-2 into this equation, and the result is:

$$\lambda_g=\frac{\lambda_{pm}}{2} \tag{5-10}$$

For our experiment, λ_g has to be between 312.5 to 333 nm since the limited transmission wavelength of the light source is from 1500 nm to 1600 nm. λ_{pm} should be in the range of 625 to 666 nm. Besides, for +1/-1st order grating, no diffraction will occur when the illumination wavelength is higher than the grating period. Therefore, 633 nm to 666nm phase mask grating is needed.

In order to obtain enough power density, beam size must be 0.593 mm X 0.127 mm. To obtain the desired beam size, a planar convex lens with focal length 200 mm was used and the phase mask was placed 17.9 mm away from the lens.

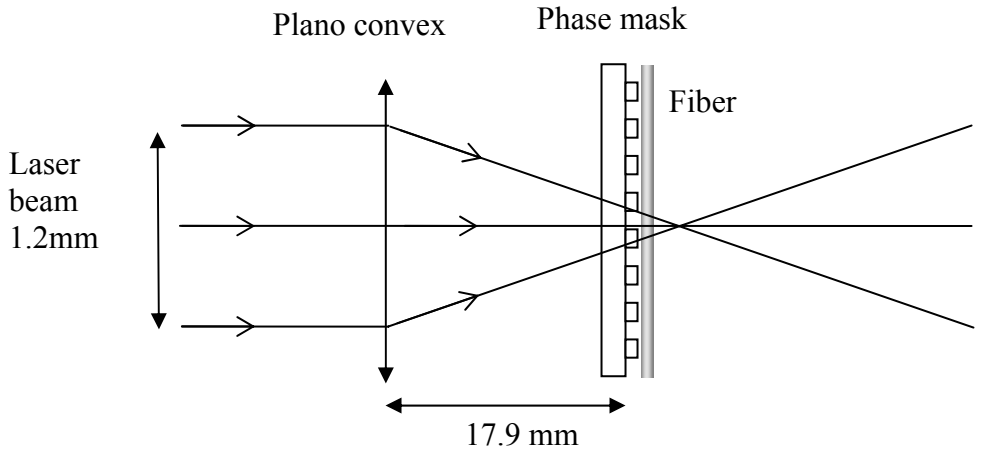

Figure 5-3 Experimental set-up for +1/-1 order phase mask

5.4. 0/-1 order phase mask

In +1/-1 order phase mask, many order beams may be present and degrade the quality of FBGs written. For 0/-1 phase mask to work, only 0th order and -1st order beam will present. This is an advantage of completely eliminating unwanted orders, leaving a clear interference pattern.

For 0/-1 phase mask to work, both the phase mask period and illumination wavelength have to satisfy the Bragg's condition and the angle we needed would be 77.6°.

$$\lambda_{HeNe} = 2\lambda_{pm} \sin\theta \qquad 5\text{-}11$$

In this case, Equation 5-8 becomes $k_x \vec{r} = 2m\pi$.

$$\therefore \lambda_g = \lambda_{pm} \qquad 5\text{-}12$$

and phase mask period equals grating period.

Besides the requirement of phase mask period, two other requirements must be fulfilled:

1. Diffraction must occur, i.e. a first order must exist. i.e., $0 \le \sin\theta_1 \le 1$

$$\therefore 0 \le \lambda_{HeNe} \le 2\lambda_{pm}$$

2. The second order must not exist.

According to the grating equation[78]:

$$d\left(\sin\theta_1 + \sin\theta_2\right) = m\lambda_{HeNe} \qquad 5\text{-}13$$

By substituting $\sin\theta_1 = \dfrac{\lambda_{HeNe}}{2\lambda_{pm}}$ and $m = 2$ for 2nd order,

$$\sin\theta_2 = \frac{\lambda_{HeNe}}{2\lambda_{pm}}$$

If 2nd order is not permitted, $\dfrac{2}{3}\lambda_{pm} < \lambda_{HeNe}$

Therefore, $\dfrac{2}{3}\lambda_{pm} < \lambda_{HeNe} \le 2\lambda_{pm}$.

λ_{HeNe} = 633 nm and λ_{pm} has to be in the range of 316.5 nm to 949.5 nm.

Since we need to inscribe FBGs at range of 1500 nm to 1600 nm, λ_{pm} will be in the range of 312.5 nm to 333 nm.

Combining the two requirements, we can use 0/-1 order phase mask with period 316.5 nm to 333 nm.

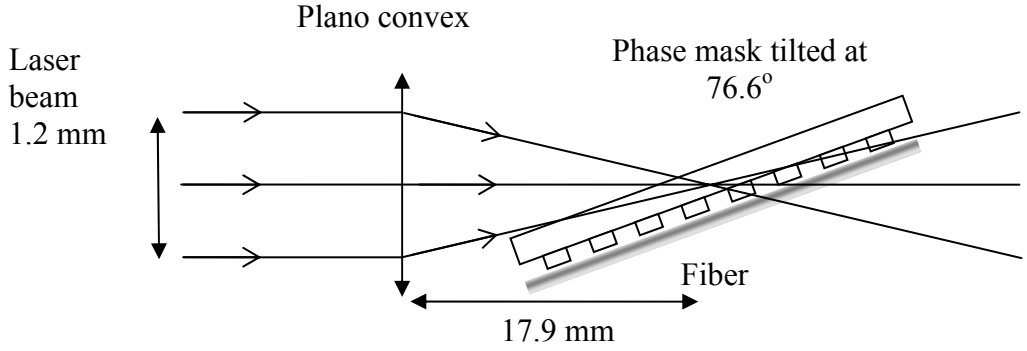

Figure 5-4 Experimental set-up for 0/-1 order phase mask

5.5. Distance requirement between the phase mask and the fiber

To obtain good FBGs, the distance between the phase mask and the optical fiber is very critical. Too great a distance will result in blurred interference fringes and low reflectivity Bragg gratings[79]. To determine out this distance, the minimum requirement of the spatial coherence of the HeNe laser, *d*, should be known:

$$h = \frac{d}{2\tan\left(\frac{\theta}{2}\right)} \qquad 5\text{-}14$$

where *d* is the minimum spatial coherence length of the HeNe laser, *h* is distance between fiber core and phase mask.

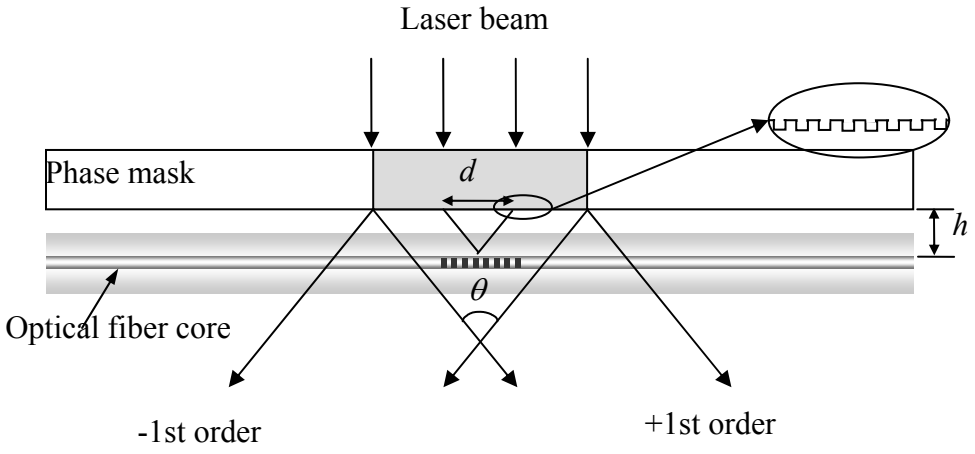

Figure 5-5 Effective distance between phase mask and optical fiber to achieve desired interference

In our experiment, HeNe (633 nm) laser and phase mask with period 642 nm were used. From

$$\theta_1 = 2\sin^{-1}\left(\frac{\lambda_{HeNe}}{\lambda_{pm}}\right) \qquad 5\text{-}15$$

θ is calculated to be 160.79°.

$$h = 0.0846d \quad (5\text{-}16)$$

For our HeNe laser, the coherence length is 1.2 mm. Thus, the minimum distance between phase mask and the optical fiber core has to be less than 101.5 μm.

5.6. Phase mask fabrication at Ohio State University

5.6.1. E-beam lithography

While attempting to use the phase mask technique at the earlier stage, we tried to fabricate the phase mask with electron beam lithography[80]. We collaborated with the Ohio State University Nanoscale Patterning Laboratory. The Leica EBPG-5000 they used is a state-of-the-art electron beam lithography system for patterning samples. The system can achieve feature size which is less than 10 nm.

We first tried single layer photoresist on soda lime glass slides but lift off was unsuccessful. Later, by changing to bilayer photoresist and quartz substrate, a 640nm period phase mask was obtained. It was done by first depositing ~500 nm MMA (8.5) MMA EL11 which is a copolymer of PMMA with 8.5% methacrylic acid, 11% total solids content in solvent ethyl lactate and then ~90 nm 950K PMMA A2. 500 Å Al layer was then deposited on top of the resist, for both charge elimination and was then exposed and developed. Lift off was done after the developing. Two phase masks with different metal deposition were prepared.

1. Phase mask A (500 Å of Au and 300 Å of Ti)
2. Phase mask B (600 Å of Al)

Several electron beam dose rates were tested for both phase masks to obtain the desired 1: 1 line gap ratio. To analyze the phase masks fabricated, FEI Sirion SEM 12 kV with FEG source, was performed by staff at OSU for SEM analysis and MFM-Scanning Probe Atomic/Magnetic Force Microscopy in contact mode was performed here at ISU for AFM analysis. The best results of each type of phase masks were reported in Section 5.6.2 and Section 5.6.3.

5.6.2. Phase mask with 500 Å of Au and 300 Å of Ti

BSE image of the Au/Ti coated phase mask is shown in Figure 5-6.

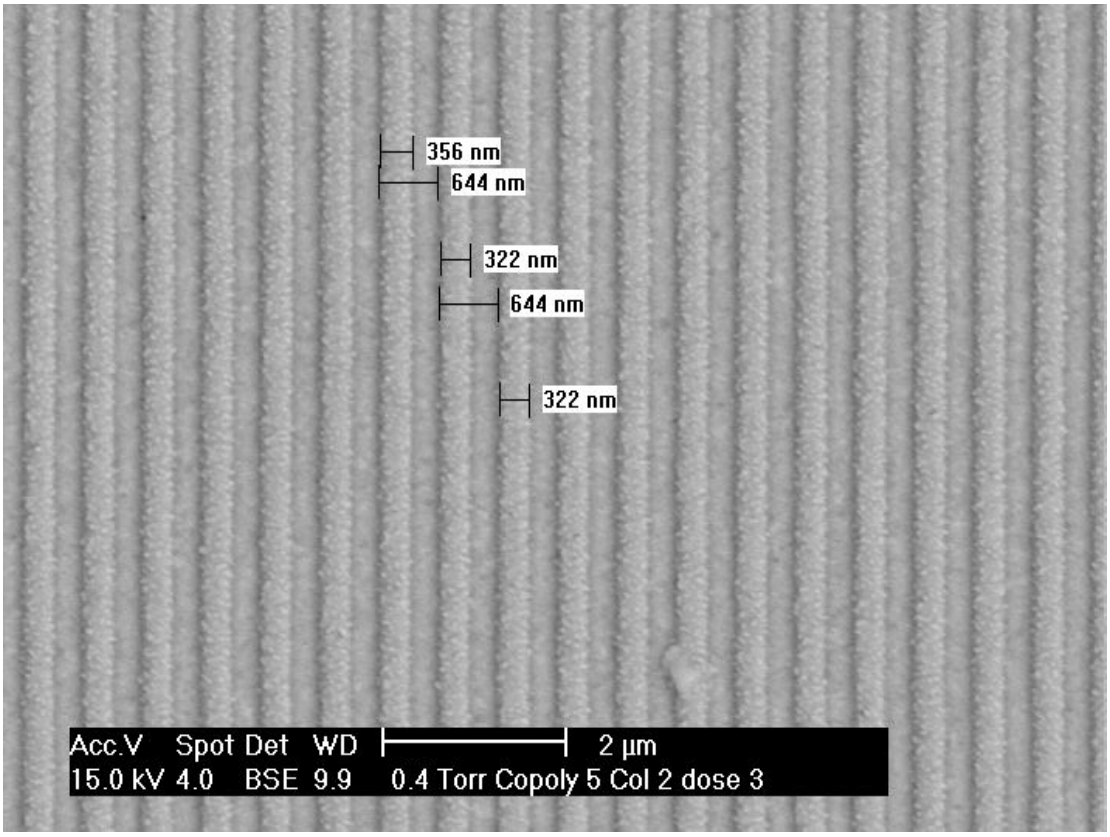

Figure 5-6 BSE image of the Au/Ti phase mask (Provided by OSU)

It showed a fairly good periodity 644 nm. However, with the instrumental error of 12 nm for line measurement in the SEM under consideration, it showed a slight difference between the line gap ratio, which ideally should be 1:1. Also, it was uncertain if the metal has been removed thoroughly during the lift off process as we did not see the significant contrast between the metal and quartz substrate. Therefore, AFM analysis has been performed to further characterize the phase mask and the result is showed in Figure 5-7.

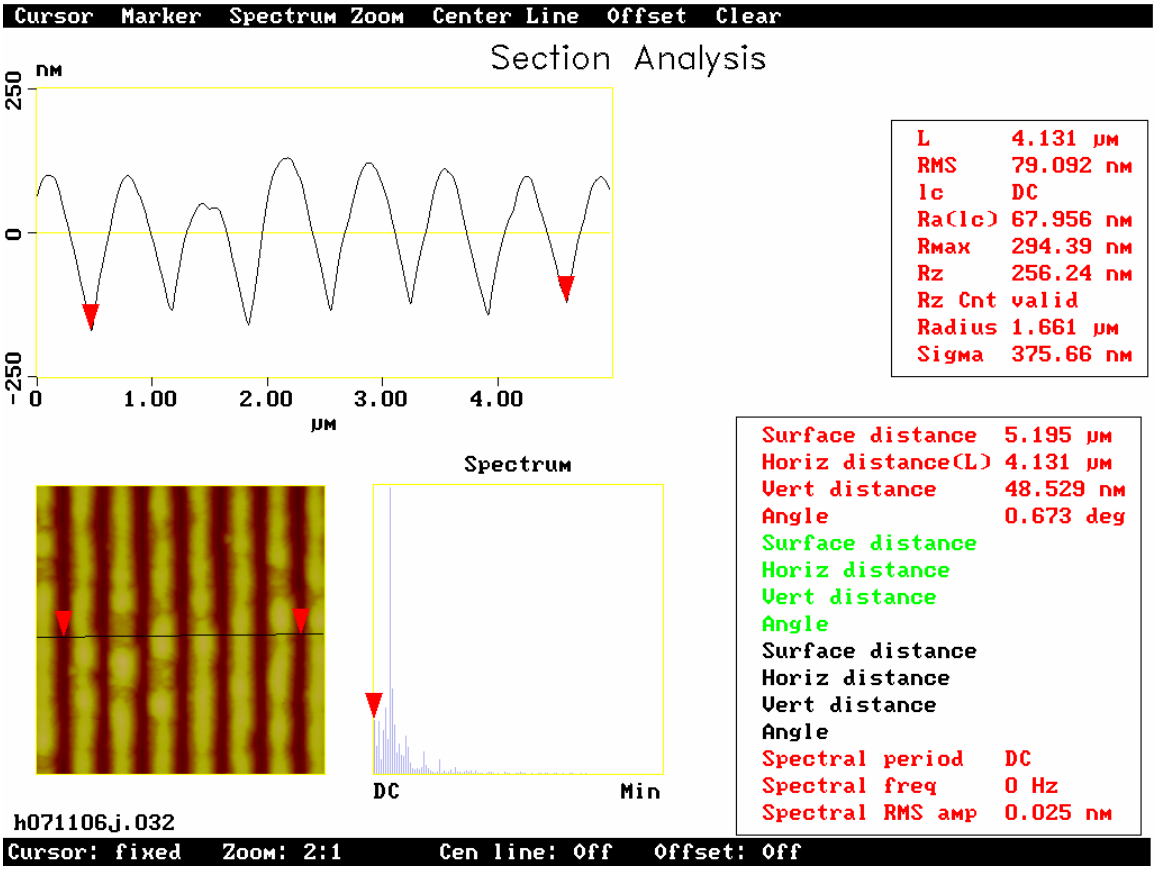

Figure 5-7 AFM analysis of the Au/Ti phase mask

AFM result in Figure 5-7 showed that the edges of the metal layer were round off. It is believed that this will lead to the degrade diffraction pattern. The pitch depth is found to be 260 nm. Since the metal layers should be in thickness 130 nm. Thus, it is believed that the metal layers were successfully lifted off. However, part of the photoresist was not removed thoroughly.

By projecting the 1st order beam to a screen, we found that the diffraction pattern is not desired. Also, we found that the phase mask did not transmit enough light so that the +1 and -1 order beam were so weak that they are occupied less than 3% total intensity of the laser beam.

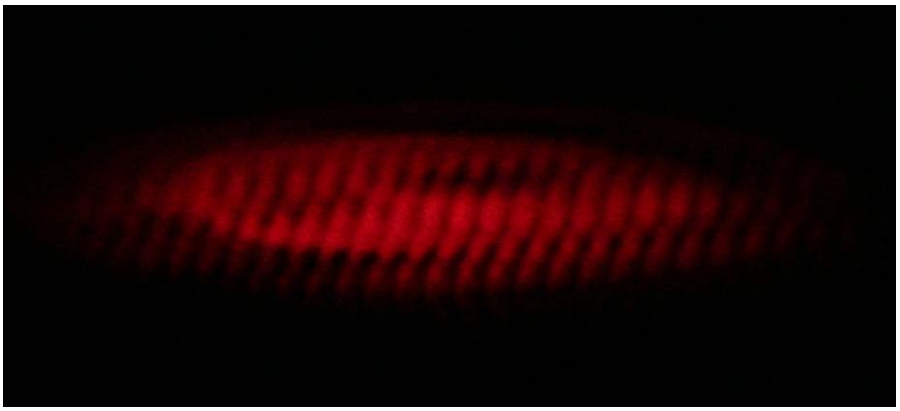

Figure 5-8 First order beam diffracted by Au/Ti phase mask

5.6.3. Phase mask with 600 Å of Al

Because of the more significant charging effect on the Al phase mask, the BSE image was taken under low vacuum. The pitch period was measured to be 648 nm by SEM (Figure 5-9), which seemed satisfying our need However, the line was measured to be 344nm while the gap was 324 nm.

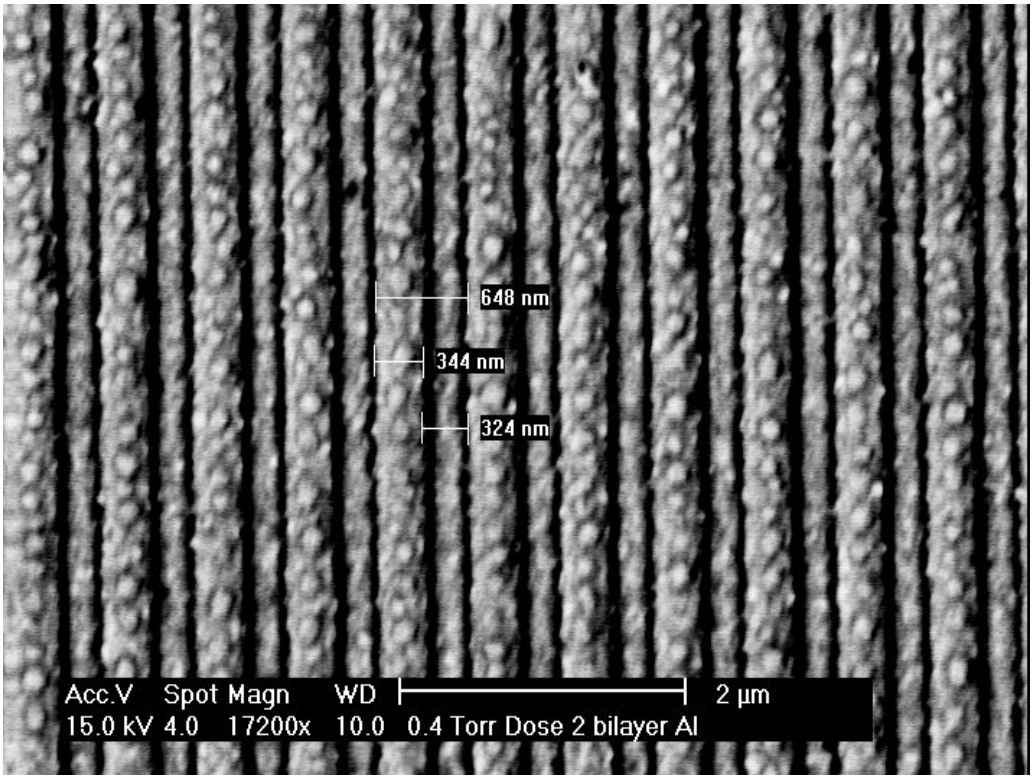

Figure 5-9 BSE image of the Al phase mask (Provided by OSU)

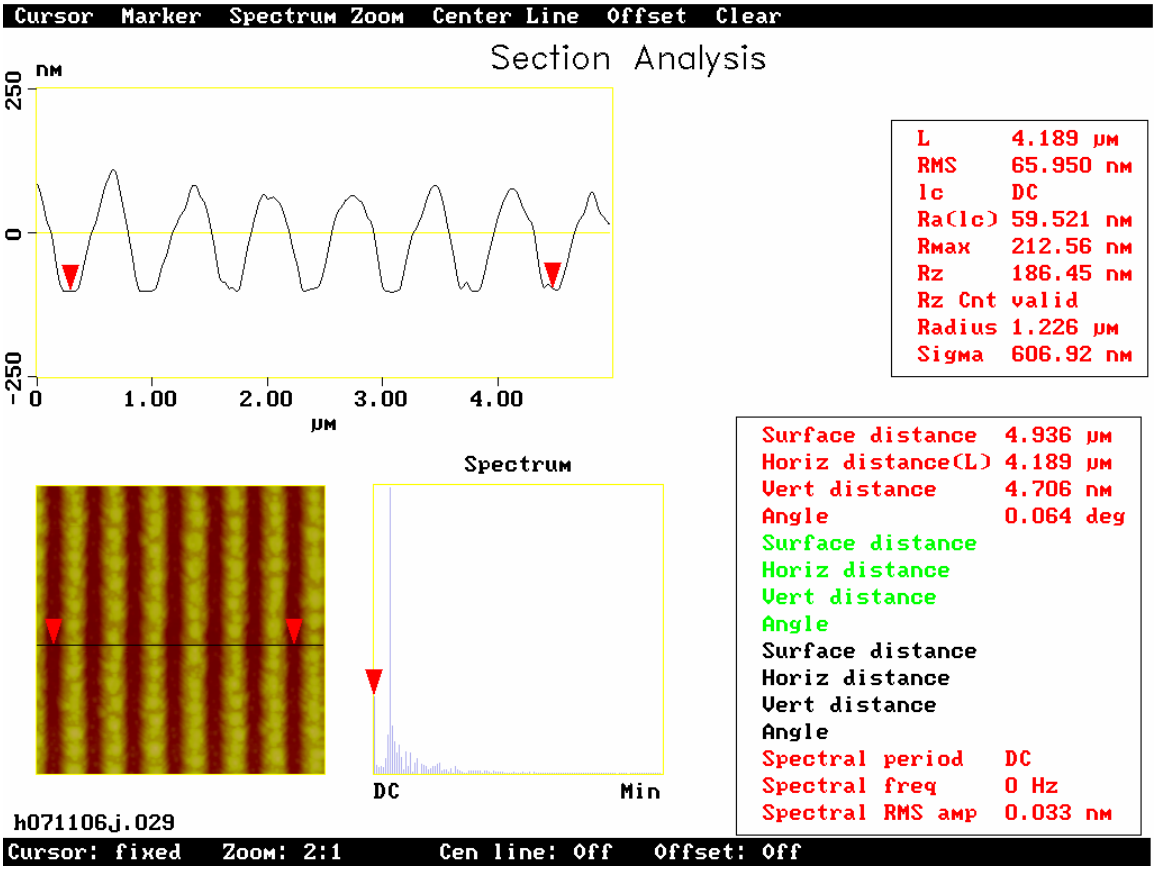

Figure 5-10 AFM image of the Al phase mask

For Al coated phase mask, the pitch depth was found to be 180 nm by AFM measurement, also indicated that the metal layer was successful lifted off

For the period measurement, the results were tabulated in Table 5-1.

Table 5-1 Period measurement of two phase masks using SEM and AFM

	Phase mask Au/Ti	Phase mask Al
SEM	644 nm	648 nm
AFM	688.5 nm	698.5 nm
AFM after calibration	634.5 nm	646.5 nm

Secondary electron image of the two phase masks shows that the image is in the range of 623 -666 nm as we needed. However, phase mask A was calculated to be off the range slightly from the AFM measurement.

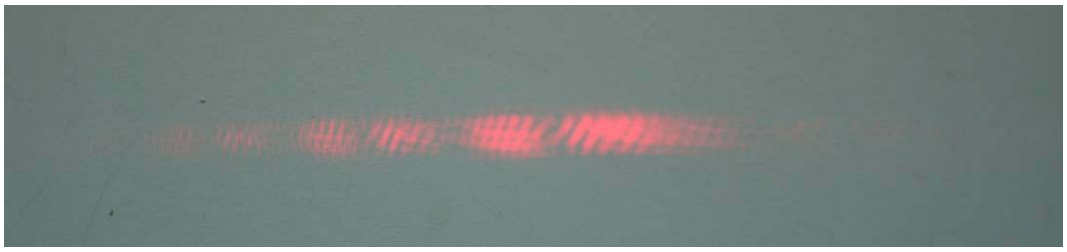

Figure 5-11 First order beam diffracted by Al phase mask

By projecting the 1st order beam to a screen, we found that the diffraction pattern produced by the Al phase mask is distorted. Though we could see the first order beam spot, the +1 and -1 order beam were so weak that the power meter with sensitivity of 0.1 mW cannot detect any signal. It is believed that the photoresist and metal layers have absorbed the light and thus limited amount of light was being transmitted and diffracted.

5.6.4. Results of FBGs writing experiment

The metal deposit layer was susceptible to absorption and therefore limited amount of light can transmit through the phase masks.

Besides, since 0th order suppression was not under consideration during the fabrication of the phase mask, there existed normal diffraction when light passed through the phase mask. For the two phase masks fabricated, there were no significant results obtained during the FBGs writing experiment.

5.7. +1/-1 order phase mask purchase

When we were still working on improving the phase mask fabrication process to suppress the 0th order beam, we were also looking for a supplier which produced the phase mask for us so that we can working on the FBGs writing experiment. We obtained a +1/-1 order phase mask from StockerYale, Canada. The pitchs were etched in the silica glass substrate by holography This phase mask has 642 nm ± 0.02 nm to 2.2% and 35.0% ±1st order efficiency for 248 nm (UV) light.

5.7.1. SEM and AFM analysis on the phase mask

JEOL JSM-606LV SEM (Tungsten) and AFM analysis were performed to characterize the phase mask.

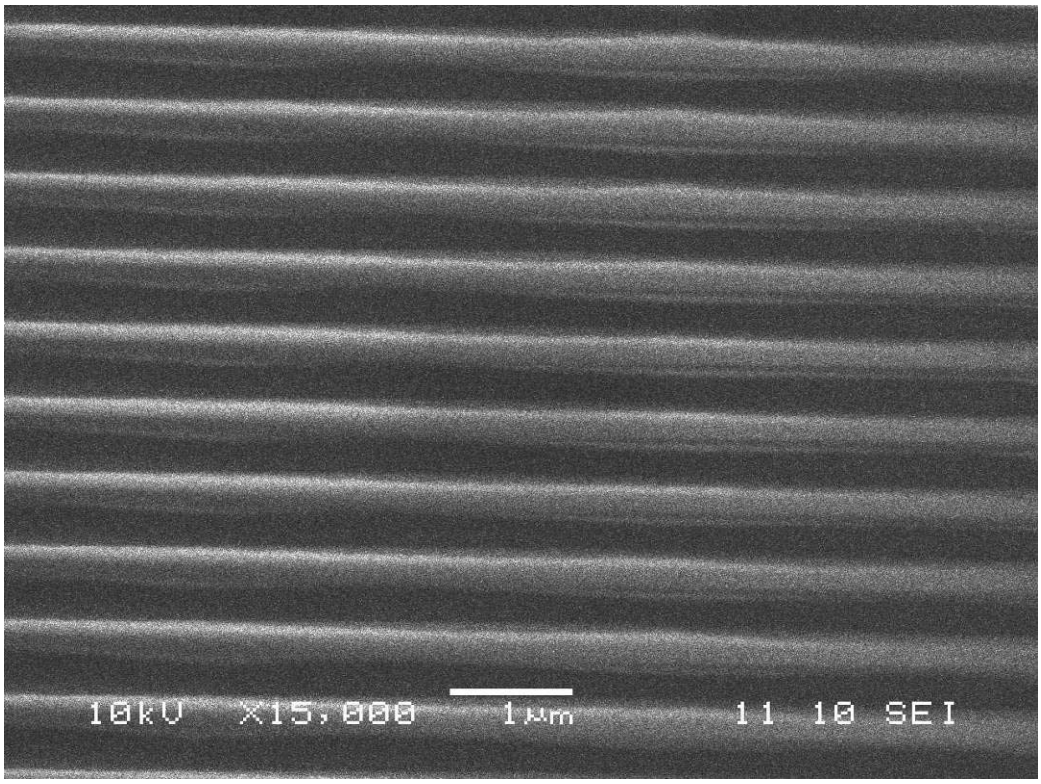

Figure 5-12 SEM image of the phase mask purchase from StockerYale, with period 642 nm

From SEM image shown in Figure 5-12, the pitches are uniformly distributed, with line gap ratio closed to 1:1.

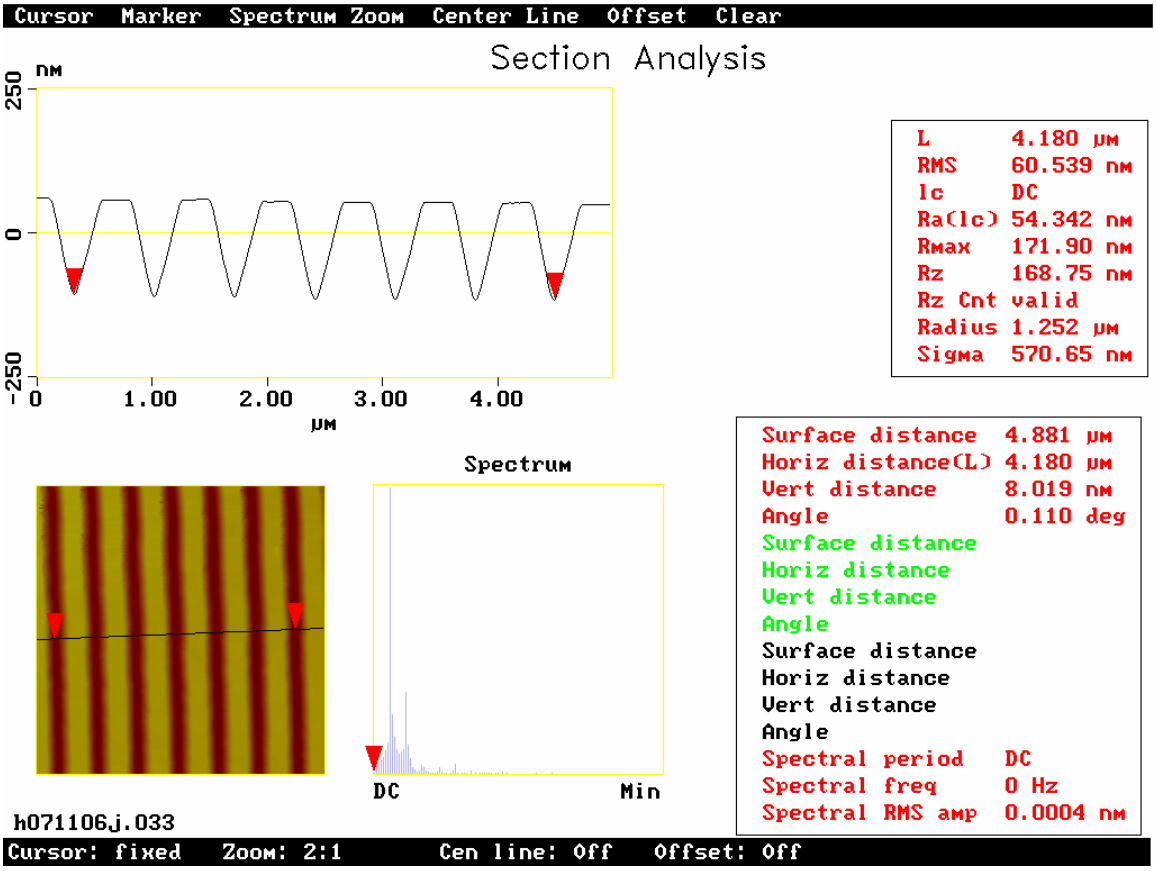

Figure 5-13 AFM result of the phase mask purchase from StockerYale

For AFM result shown in Figure 5-13, it was found that the pitch period is 642 nm, which matched the specification of the phase mask very well. Also, the pitch profile is very regular with good periodicity, which is critical for producing good diffraction pattern.

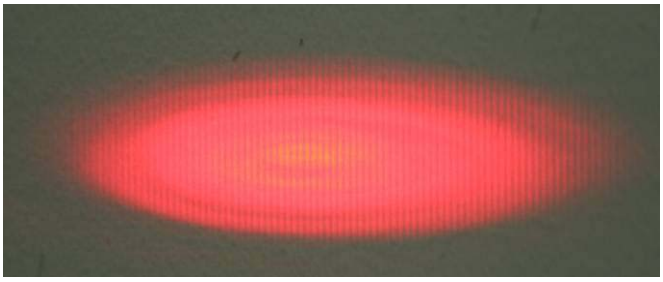

Figure 5-14 First order beam diffracted from StockerYale, +1/-1 phase mask

Unlike the phase mask produced by e-beam lithography, the first order beam has very uniform fringes. This was expected to promote good intereference for FBGs.

5.7.2.Results of FBGs writing

Even though the zero order should be suppressed by this +1/-1 order phase mask, we can still see a very bright zero order beam and relatively weak +1 and -1 order beams after the light passing through the phase mask. Moreover, we were not able to write any significant FBGs after several attempts. It is suspected that there may not have been enough laser power was provided for the chemical reaction. A power meter (S120, Thorlabs Inc.) was used to measure the beam power for 0th and +1/-1st order beams and the results were tabulated in Table 5-2.

Table 5-2 Power measurement the diffracted beams using +1/-1 order phase mask

Order	Power (mW)	Intensity (%)
0	28.3±0.5	81±2%
+1	3.3±0.5	9.5±2%
-1	3.3±0.5	9.5±2%

It is found that 81% of light came out as 0th order beam. FBGs should be written using the +1/-1 order beams for +1/-1 order phase mask. It is thought to be totally 19% of light intensity would not be enough for FBGs writing using 35mW HeNe laser.

The reason that the zero order beam has not been successful suppressed is thought to be due to the close value of the HeNe light (633 nm) and the pitch period (642 nm).

In fact, it is possible to find FBGs in the region of ~3000 nm before of the presence of interference for 0th order beam and the +1/-1 order beams, we do not have instrument applicable in the 3000 nm range to perform the experiment.

5.8. 0/-1 order phase mask purchase

Since we did not succeed in writing FBGs using +1/-1 order phase mask and realized that this may not be the best experimental approach, we changed to 0/-1 order phase mask purchase. Note that the period of the phase mask is 316 nm to 333 nm and it is very difficult to achieve. Only one company within our search could make phase mask with such a small period.

A 0/-1 order phase mask with period 324 nm was obtained from Ibsen Photonics, Denmark. Interferometry (holography) was employed to pattern the gratings. This phase should be able to produce Bragg gratings at 1555.2 nm, without considering the demagnification effect of the focusing lens. With the presence of the focusing lens, the Bragg gratings period will decrease slightly.

Since the AFM analysis will damage the phase mask, it was not performed to characterize this specific phase mask. Instead, we were able to obtain a SEM image of the cross section of a phase mask with similar period (330 nm) from the company to see the pitch profile, which is shown in Figure 5-15. It showed a regular pitch profile and is comparable to another holographic phase mask previously mentioned.

Figure 5-16 shows the projected 1st order beam and clear fringes can be seen.

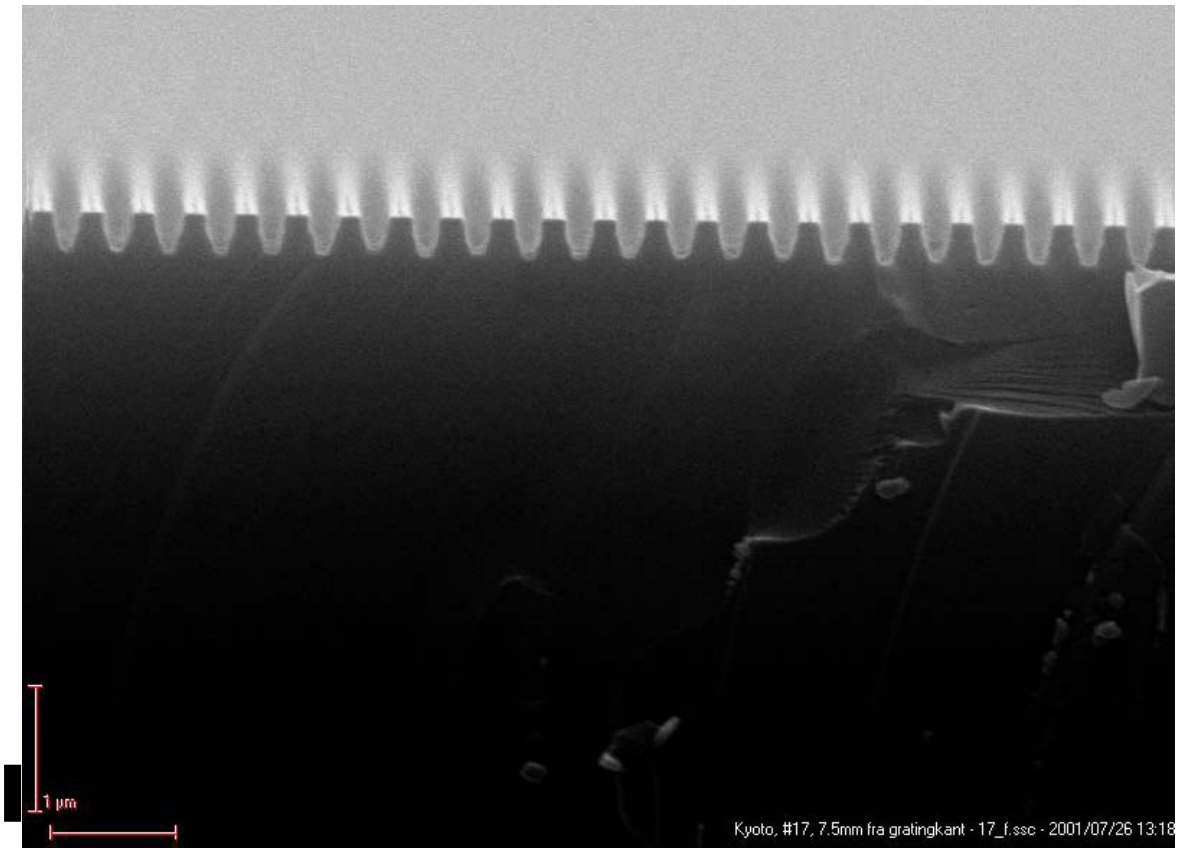

Figure 5-15 SEM image of cross-section of phase mask with period 330 nm produced by Ibsen Photonics (Provided by Ibsen Photonics)

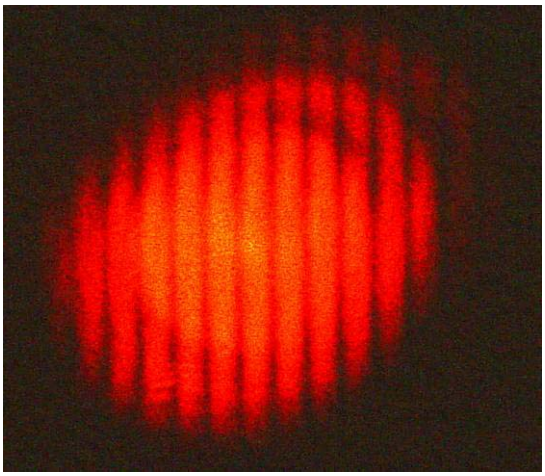

Figure 5-16 First order beam diffracted by Ibsen, 0/-1 order phase mask

To make sure there is enough energy density for FBGs writing, the power of the 0th order and 1st order beam were measured and the results are tabulated in Table 5-3.

Table 5-3 Power measurement the diffracted beams using 0/-1 order phase mask

Order	Power (mW)	Intensity (%)
0	17.8±0.5	56.7%±3%
-1	13±0.5	43.3% ±3%

5.8.1. Results of FBGs writing

The transmission spectra of the As_2S_3 fiber before and after the FBGs writing experiment were shown in Figure 5-17 and Figure 5-18 respectively.

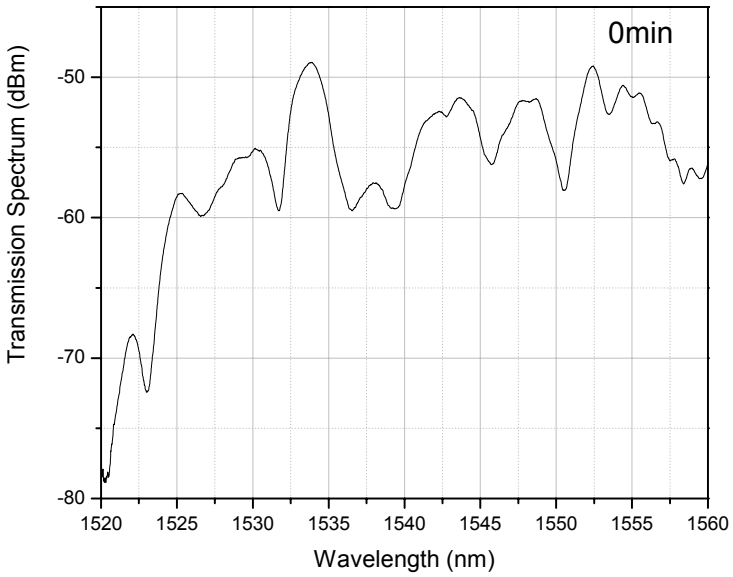

Figure 5-17 Transmission spectrum of As_2S_3 fiber before the FBG writing experiment

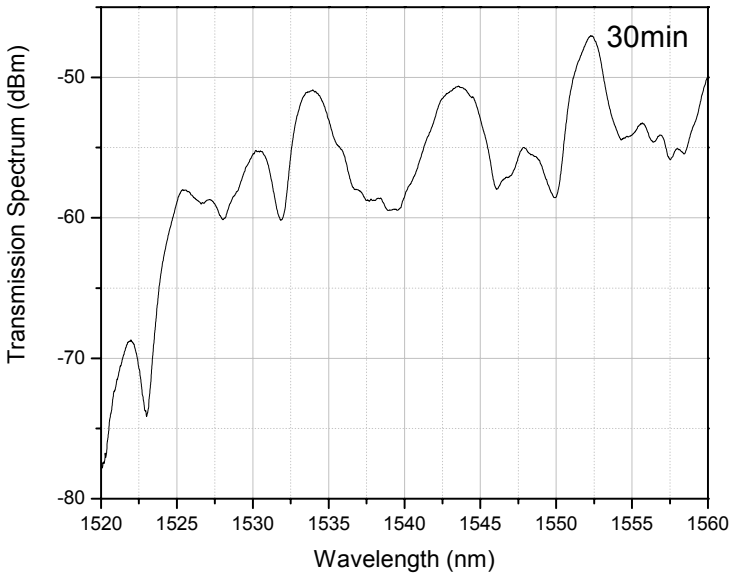

Figure 5-18 Transmission spectrum of As_2S_3 fiber after the FBG writing experiment

The growth of FBGs versus time is plotted in Figure 5-19.

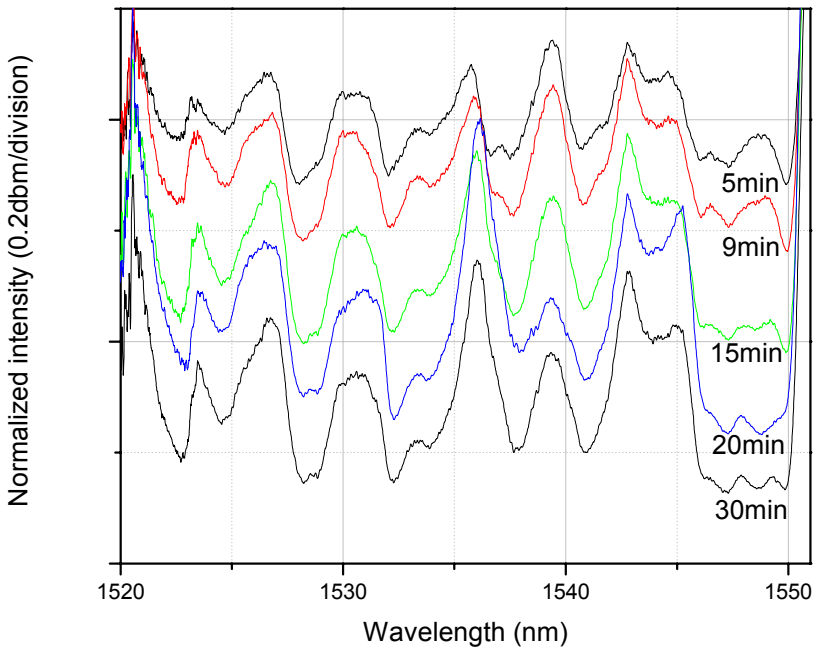

Figure 5-19 Growth of FBGs in As_2S_3 multimode fiber

From the result obtained from phase mask technique, we can also see multiple dips in the normalized transmission spectrum. However, unlike the data obtained from interferometric method, it did not show a very sharp period difference. It is believed that the interference pattern formed from interferometric method have better contrast than that formed by a phase mask. Besides, the presence of slight misalignment of the set-up, as shown by other researchers[65] will cause the cladding coupling which complicated the spectrum. Also, the interference pattern obtained by a phase mask is strongly affected by the quality of the phase mask and the phase mask distance between the optical fiber core (101.5 μm).

Since our phase mask period is 324 nm, it is believed that the dip at 1544.4 nm would be due to the N = 0 mode. Since the dips are much broader than that obtained from interferometric method, the Bragg wavelength is more difficult to measure.

The maximum reflectivity is 61.9% obtained at 1548.8 nm. The gratings started to grow after 3 min. of laser exposure and the reflectivity increased gradually as irradiation time increased. It started to saturate at around 30 min. and the reflectivity versus time is plotted in Figure 5-20.

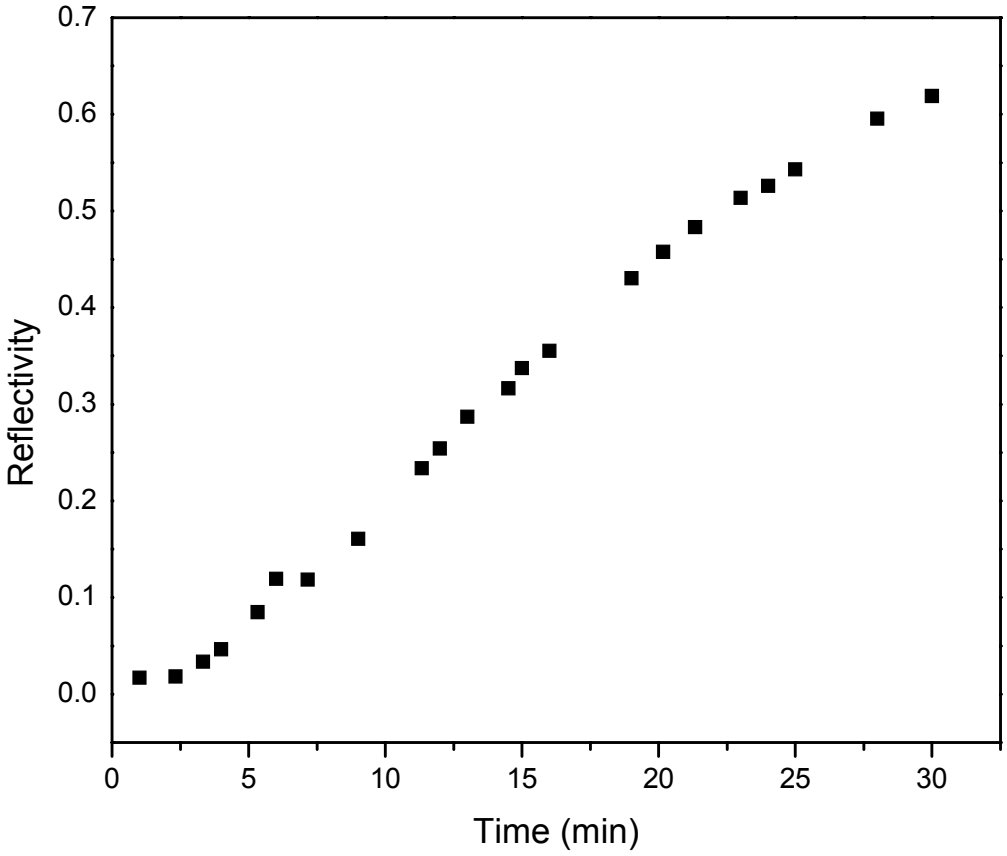

Figure 5-20 Reflectivity versus time of laser exposure during the FBGs writing experiment

Also, the effective index was estimated using the same method described in Section 4.3 and the data is tabulated in Table 5-4.

Table 5-4 Calculation of effective index of refraction

Initial wavelength (nm)	1527.98	1532.04	1537.42
Final wavelength (nm)	1528.28	1532.28	1537.84
$\Delta\lambda$ (nm)	0.30	0.25	0.42
Δn_{eff}	0.000458	0.000378	0.000644

Thus, the averaged effective index change is estimated to be 0.000493.

5.8.2. Temperature dependence of FBGs

We attempted to examine the temperature dependence of FBGs in multimode As_2S_3 fiber using a very simple design: 2 heating rods with temperature controller were used for heating experiment while a thermocouple was used to measure the FBGs shift over in a short range temperature change.

The shift of FBGs in silica fiber due to temperature change[21] was given by:

$$\Delta\lambda_B = \lambda_B(\alpha_\Lambda + \alpha_n)\Delta T \qquad 5\text{-}17$$

where $\alpha_\Lambda = \frac{1}{\Lambda}\left(\frac{\partial\Lambda}{\partial T}\right)$ is the thermal expansion coefficient for the fiber and

$\alpha_n = \frac{1}{n_{eff}}\left(\frac{\partial n_{eff}}{\partial T}\right)$ is the thermooptic coefficient .

In the case, it is assumed the wavelength shift is due to the change of the FBGs period and also the change of refractive index of fiber.

For As_2S_3 glass, α_Λ which is approximately 21.4 x 10^{-6} K^{-1} and α_n is approximately equal[46,81] to -8.6x10^{-6} K^{-1}. Therefore, $\frac{\Delta\lambda_B}{\lambda_B} = 1.28\times10^{-5}$ for 1 K change for As_2S_3 single mode fiber. For λ = 1561 nm, $\frac{d\lambda_B}{dT}$ would be 0.02 nm K^{-1}.

Figure 5-21 shows the date obtained from two temperature dependence experiment trials. We found that our experimental $\frac{d\lambda_B}{dT}$ value to be about 0.4 nm K^{-1} (Figure 5-21) and the value does not fit into the equation used above which consider only the thermooptic coefficient and thermal expansion coefficient.

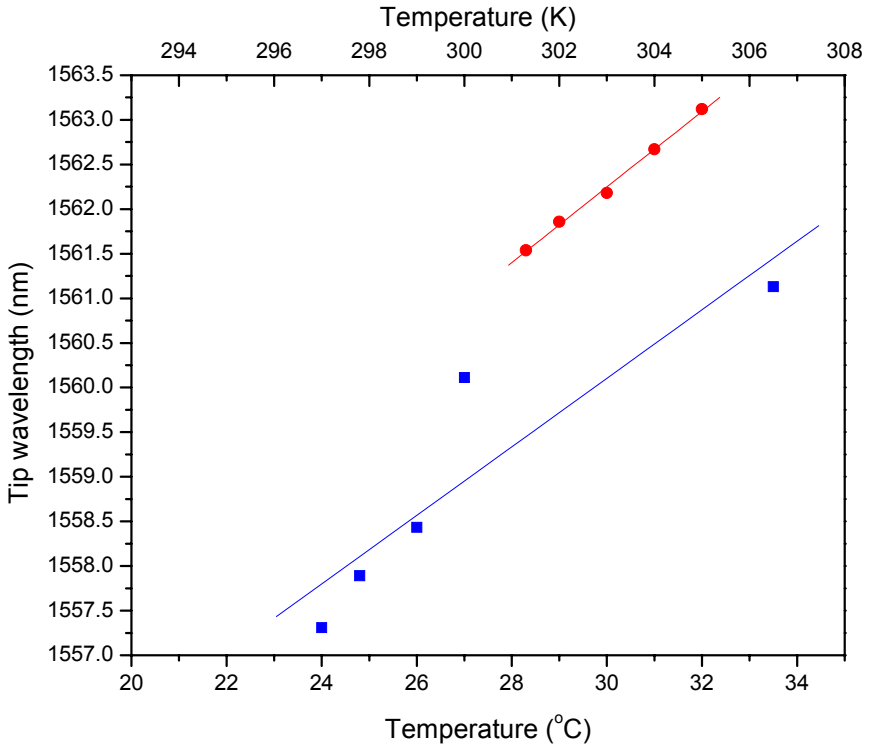

Figure 5-21 Temperature dependence of FBGs

It is believed that it may be more than other thermal expansion and thermo-optical change taking place during the heating process. Other factors should have effect on the temperature dependence of FBGs in As_2S_3 multimode fiber: photosensitivty exhibited in the As_2S_3 glass is known to be metastable and can be annealed by thermal energy[42, 82]; diffusion would change the light guiding condition and the temperature dependence of dispersion in the multimode fiber.

6. Future work

Since it is very difficult to drill a concentric hole with small diameter and long depth in the As_2S_3 glass perform, rotational casting used in fluoride glass optical fibers[83] may be tried to obtain the core/clad perform.

To examine the sensing capabilities of the FBGs in As_2S_3 multimode fiber, more research should be done in the future to examine the effect of the temperature dependence of photosensitivity on the FBGs. Also, bending of the fiber which causes FBGs shift should be avoided. A more sophisticated temperature control system may help to increase the temperature range for this temperature dependence study. To limit the variables, single mode As_2S_3 fiber, if available, would still be a better choice for studying the temperature sensing capability.

7. Conclusions

We used both interferometric method and phase mask technique to write FBGs in multimode As_2S_3 fiber.

Using interferrometric method, we obtained FBGs of maximum reflectivity 46.6% at 1526.6 nm, using the writing angle of 152^o (corrected to 151.67^o). Multiple dips appeared due to same mode reflection and neighboring mode coupling. The average effective index change is estimated to be 0.000482.

Using phase mask technique, we obtained FBGs of maximum reflectivity 61.9% at 1548.8 nm. We also observed multiple dips but the profile of these dips are slightly different and the periodicity is not obvious. This may be due to the slight misalignment in the optical set-up. The effective index change is estimated to be 0.000491.

Both reflectivity and effective index change of FBGs written are comparable using the two methods. The reflectivity of FBGs obtained by two different methods is relatively low compared to the SiO_2 FBGs. It is believed that misalignment of the optical set-up and slight vibration would contribute to the low reflectivity. The large diameter and photosensitivity of the fiber cladding and low laser power may also be the causes. It is known that As_2S_3 would be photosensitive to 1.5 μm irradiation[84] and therefore the light source may also have effect on the FBGs writing process.

Because of the low mechanical strength of the fiber, mechanical testing was not done to the FBGs as it would break easily with low stress or slight bending.

About temperature sensing, wavelength shift is estimated to be about 0.4 nm K^{-1} based on our simple experiment. However, the value does not fit into equations used to explain temperature dependence of SiO_2 fiber. It is therefore believed that some other factors, such as temperature effect on photosensitivity, dispersion in the fiber, may play an important role to the wavelength shift of FBGs.

8. Acknowledgements

I would like to thank Dr. Steve W. Martin for his guidance and support throughout my graduate study. I am very grateful to his continuous encouragement even at the time when we had little progress on the research.

I would also like to thank the researcher who had participate in this project: Dr. Brito Ferreira and Kyle Berg; and all of the researchers who have worked with me in the Glass and Optical Materials group: Dr. Chad Martindale, Dr. Jason Saienger, Dr. Annamalai Karthikeyan, Dr. Steve Poling, Dr. Sik Kim Young, Wen Long Yao, In Seok Seo, Bryce Campbell, Carly Nelson and the undergraduate assistants for their help and the great time throughout these years. I would like to give my appreciation to Dr. Pal Molian, Dr. Kristen Constant, Dr. Xiaoli Tan, Dr. Joseph Shinar, Dr. Bruce Thompson, Dr. Robert Weber, Dr. Adin Mann, Dr. Lacticia Petit, Dr. Chester Lo, Dr. John Ballato, Amy Bross, Jun Xu and many others for their advices and help on the research.

I would like to give thanks to my family and friends that have supported me throught my PhD study.

This work is supported by NASA-Advanced Non Destructive Evaluation for Future Aerospace Systems Grant # NA6102098.

9. References

1 G. A. Ball, W. W. Morey, J. W. Dawson, IS&T's 49th Annual Conference, 1996, 465-466.

2 S. Yiou, G. Lucas-Leclin, F. Balembois, P. Georges, Applied Optics, 2002, 41(30), 6356-9.

3 Z. Wei, L. Qin, Q. Wang, H. Li, W. Zheng, Y. Zhang, Optics Communications, 2000, 177(1-6), 201-205.

4 A. Ezbiri, S. E. Kanellopoulos, V. A. Handerek, Optics Communications, 1998, 150(1-6), 43-48.

5 P. Ferdinand, S. Magne, V. Dewynter-Marty, S. Rougeault, L. Maurin, MRS Bulletin, 2002, 27(5), 400-40.

6 S. Tsao, J. Wu, IEEE Journal of Selected Topics in Quantum Electronics, 1996, 2(4), 894-897.

7 A. O'Keefe, J.J. Scherer, U.S Patent, US6694067.

8 N. Takahashi, K. Tetsumura, S. Takahashi, Japanese Journal of Applied Physics, 1999, 38(5B), 3223-3236.

9 L. Zhang, Fiber Optic Sensors, Marcel Dekker, Inc., New York, 2002.

10 R. Kashyap, Fiber Bragg Gratings, Optics & Photonics, San Diego, CA: Academic Press, 1999.

11 B. Lee, Y. Jeong, Interrogation techniques for fiber Grating sensors and the theory of fiber gratings, Fiber Optic Sensors, Marcel Dekker, Inc., 2002.

12 S. Takeda, Composites Part A: applied science and manufacturing, 2002, 33, 971-980.

13 K. T. V. Grattan, B. T. Meggiitt, Optical Fiber Sensor Technology Advanced Applications-Bragg Gratings and Distributed Sensors, Kluwer Academic Publishers, Boston, 2000, 1-78.

14 P. M. Nellen, U. Sennehauser, R. Bronnimann, Optical Engineering, 1996, 35(9), 2570-2577.

15 J. Jung, N. Hui, J. H. Lee, N. Park, B. Lee, Applied Optics, 1999, 38(13), 2749-2751.

16 S. A. Wade, D. I. Forsyth, K. T. V. Grattan, Q. Guofu, Review of Scientific instruments, 2001, 72 (8), 3186-3190.

17 C. I. Merzbacher, A. D. Kersey, E. J. Friebele, Smart Materials and Structures, 1996, 5(2), 196-208.

18 W. Ecke, I. Latka, R. Willsch, A. Reutlinger,R. Graue, Measurement Science and Technology, 12(7), 2001, 974-980.

19 A. V. Kolobov, K. Tanaka, Handbook of Advanced Electronic and Photonic Materials and Devices, Acedemic Press, 2001, 47-90.

20 K. O. Hill, Y. Fujii, D. C. Johnson, and B. S. Kawasaki, Applied Physics Letters, 1978, 32, 647-649.

21 A. Othonos, K. Kalli, Fiber Bragg Gratings, Artech House, 1999.

22 D. P. Hand, P. St. J. Russell, Optics Letters, 15, 1990, 102-104.

23 C. Flori, R. A. B. Devine, Physical Review B, 72, 1998, 1287-1289.

24 A. K. Varshneya, Fundamentals of Inorganic Glasses, Academic Press, Inc, 1994.

25 D. J. Treacy, U. Strom, P. B. Klein, P. C. Taylor, T. P. Martin, Journal of Non-Crystalline Solid, 35&36, 1980, 1035-1039

26 A. Saitoh, T. Gotoh, K. Tanaka, Journal of Non-Crystalline Solids, 299-302, 2002, 983-987.

27 A. Siliminia, K. L. Foulgoc, A. Villeneuve, T. Galstian, K. Richardson, Fiber and Integrated Optics, 20, 2001, 151-158.

28 J. Heo, M. Rodrigues, S. J. Saggese, George H. Sigel Jr. Applied Optics, 30(27), 1991, 3944-3951.

29 J. S. Sanghera, I.D. Aggarwal, Journal of Non-Crystalline Solids, 256&257, 1999, 6-16.

30 J. A. Moon, D. T. Schaafsma, Fiber and Integrated Optics, 19, 2000, 201-210.

31 M. S. Maklad, R. K. Mohr, R. E. Howard, P. B. Macedo, C. T. Moynihan, Solid State Communications, 15, 1972, 855-858.

32 P. Hari, S. Guzel, T. Su, P. C. Taylor, P. L. Kuhns, W. G. Moulton, N. S. Sullivan, Journal of Non-Crystalline Solid, 326&327, 2003, 199-204.

33 N. A. Goryunaova, B.T. Kolomiets, Zh. Tekhn. Fiz. 25, 1955, 984.

34 N. A. Goryunova, B.T. Kolomiec, Izv. Akad Nauk, Ser Fiz 20 1956, 1496.

35 N. A. Popov, Pis'ma v Zhurnal Eksperimental'noi I Teorethicheskoi, 31(8), 1980, 437-440.

36 S. A. Dembovsky, E. A. Chechetkina, Materials Research Bulletin, 16(5), 1981, 505-511.

37 M. Kastner, Physical Review Letters, 28, 1972, 355-357.

38 M. Kastner, D. Adler, H. Fritzsche, Physical Review Letter, 37, 1978, 1504-1507.

39 Chang R. Materials Research Bulletin, 2 1967, 145-153.

40 E. Mytilineou, P. C. Taylor, E. A. Davis, Solid State Communications, 35(6), 1980, 497-499.

41 H. Hamanaka, K. Tanaka, S. Iizima, Solid State Communications, 23(1), 1977, 63-65.

42 K. Tanaka, Physical Review B, 57, 1998, 5163-5167.

43 K. Tanaka, Journal of Non-crystalline solids, 35-36, 1980, 1023-1034.

44 O. I. Shpotyuk, Physica Status Solidi B, 183, 1994, 365-374.

45 A. V. Kolobov, B. T. Kolomiets, O. V. Konstantinov, V. M. Lyubin, Journal of Non-crystalline solids, 45, 1982, 335-341.

46 http://www.amorphousmaterials.com

47 http://www.matweb.com/search/SpecificMaterial.asp?bassnum=EINOR0042

48 T. Cardinal, K. A. Richardson, H. Shim, A. Schulte, R. Beatty, K. Le Foulgoc, C. Meneghini, J. F. Viens, A. Villeneuve, Journal of Non-crystalline solids, 256&257, 1999, 353-360.

49 W. S. Rodney, I. H. Malitson, T.A. King, Journal of the Optical Society of America, 48(9), Sep 1958, 633-636.

50 A. Ghatak, Introduction to fiber optics. Cambridge University Press,1998, 193.

51 K. T. V. Grattan, B. T. Meggiitt, Optical Fiber Sensor Technology Advanced Applications-Bragg Gratings and Distributed Sensors, Kluwer Academic Publishers, Boston, 2000, 1-78.

52 K. T. V. Grattan, B. T. Meggitt, Optical Fiber Sensor Technology: Fundamentals, Luwer Academic Publishers, Boston, 2000, 85-115.

53 J. S. Sanghera, I. D. Aggarwal, Infrared Fiber Optics, CRC Press, 1998, 15-19, 143-181.

54 P. C. Schultz, Journal of American Ceramic Society, 57, 1974, 309.

55 D. B. Keck, R. D. Maurer, P.C. Schultz, Applied Physics Letter, 22, 1973, 307.

56 J. F. Hyde, 1942, US Patent US2272342.

57 T. Kanamori, Journal of Lightwave Technology, 2 (5), Oct 1984, 607-612.

58 D. L. Wood, J. Tauc, Physics Review, 5, 1972, 3144.

59 K. O. Hill, Y. Fujii, D. C. Johnson, B. S. Kawasaki, Applied Physics Letters, 32, 1978, 647-649.

60 G. Meltz,.; W. W. Morey, W. H. Glenn, Optics Letters 14 (15), 1989, 823-825.

61 K. O. Hill, B. Malo, F. Bilodeau, D. C. Johnson, J. Albert, Applied Physics Letters, 62, 1993, 1035-1037.

62 B. Malo, K. O. Hill, F. Bilodeau, D. C. Johnson, J. Albert, Electronics Letters, 29, 1993, 1668-1669.

63 C. G. Askins, M. A. Putnam, Journal of Lightwave Technology, 15 (8), 1997, 1363-1370.

64 M. Asobe, T. Ohara, I. Yokohama, T. Kaino, Electronics Letters, 32 (17), 1996, 1611-1613.

65 X. Sang, P. L. Chu, C. Yu, R. Lai, Optical Communications, 260, 2006, 131-135.

66 M. S. Iovu, S. D. Shutov, A. M. Andriesh, E. I. Kamitsos, C. P. E. Varsamis, D. Furniss, A. B. Seddon, M. Popescu, Journal of Non-Crystalline Solids, 326&327, 2003, 306-310.

67 Yeh C, Handbook of Fiber Optics, 1990, 28-30.

68 J. Kobelke, J. Kirchhof, M. Schuster, A. Schwuchow, SPIE Conference on Infrared Glass Optical Fibers and Their Applications, 3416, 1998, 55-65.

69 V. Q. Nguyen, J. S. Sanghera, B. Cole, P. Pureza, F. H. Kung, I. D. Aggarwal, Journal of the American Ceramic Society, 85(8), 2002,2056-2058.

70 A. Othonos, Review of Scientific Instrument, 68(12), 1997, 4309-4341.

71 K. O. Hill, Y. Fujii, D. C. Johnson, B. S. Kawasaki, Applied Physics Letters, 32, 1978, 647-649.

72 G. Meltz, W. W. Morey, W. H. Glenn, Optics Letters 14 (15), 1989, 823-825.

73 K. O. Hill, B. Malo, F. Bilodeau, D. C. Johnson, J. Albert, Applied Physics Letters, 62, 1993, 1035-1037.

74 B. Malo, K. O. Hill, F. Bilodeau, D.C. Johnson, J. Albert, Electronics Letters, 29, 1993, 1668-1669.

75 T. Mizunami, T. V. Djambova, T. Niiho, S. Gupta, Journal of Lightwave Technology, 18(2), 2000, 230-235.

76 Suematsu Y. et al., Hikari Faiba Tsuusin Nyuumon, 3rd edtition Tokyo, Japan: Ohmusha 1989, 184-194.

77 Hecht E., Opitcs, Addison Wesley, 2001, 462.

78 D. Halliday, R. Resnick, K. S. Krane, Physics, John Wiley, 1992, 952-954.

79 A. Othonos, X. Lee, IEEE Photonics Technology Letters, 7, 1995, 1183-1185.

80 M. Okai, S. Tsuji, N. Chinone, T. Harada, Apply Physics Letters, 55, 1989, 415-416.

81 I. V. Fekeshgazi, K. V. Mai, N. I. Matelesko, V. M. Mitsa, E. I. Borkach, Semiconductors, 39(8), 2005, 951–954.

82 J. P. De Neufville, S. C. Moss and S. R. Ovshinsky, Journal of Non-crystalline Solids, 13, 1973, 191-223.

83 S. Sakaguchi, S. Takahashi, Journal of Lightwave Technology, LT5, 1987, 1219-1228.

84 N. Ho, J. M. Laniel, R. Vallee, A. Villeneuve, Optics Letters, 28(12), 2003, 965-967.